Towards an H I Census of the Local Universe

T.D. Joseph

Department of Astronomy
University of Cape Town
South Africa

A dissertation submitted in partial fulfillment of the requirements for the degree of M.Sc.
in
the Department of Astronomy, as part of the
National Astrophysics and Space Science Programme
UNIVERSITY OF CAPE TOWN

November 2008

Abstract

In this dissertation the results of the pilot survey for the Nançay Interstellar Baryon Legacy Extragalactic Survey (NIBLES) are presented. The goal of NIBLES is to quantify the H I content of galaxies in the Local Universe, i.e. galaxies with recessional velocities in the range $900\,\mathrm{km\,s^{-1}} \leq v \leq 12\,000\,\mathrm{km\,s^{-1}}$. The sample consists of both H I data obtained using the Nançay radio telescope and optical photometric and spectroscopic data from the Sloan Digital Sky Survey (SDSS) sixth data release for 1385 galaxies; 600 galaxies were reliably detected. The H I data were compared to data from the Northern HIPASS catalogue (NHICAT). The NIBLES recessional velocities and velocity widths at the 50% flux level were found to be in good agreement with NHICAT.

Upon examination of the H I mass-to-light ratios (M_{HI}/L) of the galaxies, values of $M_{HI}/L > 100\,\mathrm{M_\odot/L_\odot}$ were found, with a maximum of $M_{HI}/L \sim 10^4\,\mathrm{M_\odot/L_\odot}$. The cause of these high M_{HI}/L values was investigated and was found to be the result of underestimated photometric data for galaxies with Petrosian radii, $R_P < 8''$ and inclination, $i < 50°$. When the corrected photometry data are used, no galaxies fainter than $M_g \sim -13^{\mathrm{m}}$ and $M_i \sim -12^{\mathrm{m}}$ are found. Using the corrected photometry data, the maximum value of $M_{HI}/L_g = 10\,\mathrm{M_\odot/L_\odot}$ and $M_{HI}/L_i = 19\,\mathrm{M_\odot/L_\odot}$.

Acknowledgements

I would like to thank my supervisors Profs. Renée Kraan-Korteweg, Erwin de Blok and Wim van Driel for their support, guidance and advice. I appreciate all the time and effort that went into helping me with my work.

To the students in the department, especially Nikki and Ed, thank you for all the encouragement and especially the laughter. Sarah and Antoine, your support and feedback has been invaluable. Thank you very much for always making time for me. An extra special thank you to Paul for sharing his knowledge of Python and Source Extractor with me. You were never to busy to help or to listen and for that I am deeply grateful.

To my parents and sisters, thank you for all your unwavering support and love throughout my life.

I would also like to thank Jesse for his encouragement and comfort in difficult times. Your love buoyed me when I was feeling down. I appreciate all that you have done for me.

Funding for this dissertation was provided by the South African SKA Project. I would like to express my sincerest gratitude to the SA SKA team for the extra effort that was made to secure this funding for me.

Further financial assistance was provided by the National Research Foundation, the Nançay Observatory and the Paris Observatory. I am grateful for the support as well as the hospitality I received at both observatories.

This publication makes use of data from the Sloan Digital Sky Survey. Funding for the SDSS and SDSS-II has been provided by the Alfred P. Sloan Foundation, the Participating Institutions, the National Science Foundation, the U.S. Department of Energy, the National Aeronautics and Space Administration, the Japanese Monbukagakusho, the Max Planck Society, and the Higher Education Funding Council for England. The SDSS is managed by the Astrophysical Research Consortium for the Participating Institutions.

Plagiarism Statement

I know the meaning of plagiarism and declare that all of the work in the document, save for that which is properly acknowledged, is my own.

Contents

List of Figures

List of Tables

Chapter 1

Introduction

Our current understanding is that the Universe consists of 72 % dark energy, 23.8 % dark matter and 4.2 % baryons (Spergel et al., 2007). The nature of both the dark energy and dark matter is still unknown. Although baryons (i.e. protons and neutrons) make up only 4 % of the cosmos, they account for a sixth of the mass and they are the only component of the Universe that we can directly observe.

The baryonic matter in the Universe reside in several forms. They are found as clouds of intragalactic atomic and molecular gas and dust, in condensed form as stars and planets and as plasma in galaxy clusters.

The evolution of the Universe and the formation of structures within it changes the distribution and phase of the baryonic matter. Therefore, the distribution of the baryonic matter at the current epoch can give us information about the formation of these structures when compared to their distributions at previous epochs. The baryonic matter distribution is an important input parameter for cosmological models of galaxy and large scale structure formation.

Many astronomical surveys have been carried out to quantify the amount

of baryonic matter in the Universe. This quantity is called the baryon budget and it describes the mass density of baryons, ρ_b, in the Universe. This parameter is usually expressed relative to the Einstein - de Sitter critical density, $\rho_c = 9.21 \times 10^{-30} h^2$ g cm^{-3} (e.g. Prochaska & Tumlinson, 2008), as $\Omega_b = \rho_b / \rho_c$. The Einstein - de Sitter model assumes a flat Universe and ρ_c is the density associated with such a Universe (Einstein & de Sitter, 1932).

Hydrogen is the most abundant element in the Universe; 93 % of the baryons in the Universe are in the form of hydrogen. Neutral hydrogen, or H I, is the atomic form of hydrogen. It accounts for $\sim$ 33% of the Interstellar Medium (ISM) (Brinks, 1990). It is also found in structures between galaxies.

The H I budget estimated by Fukugita et al. (1998) has been revised dramatically (Fukugita, 2004). The initial estimate of $\Omega_b = (2.1 \pm 0.6) \times 10^{-4}$ was based on a sample of galaxies that was not representative of the Local Universe (Rao & Briggs, 1993). This sample was optically selected and only included bright spiral galaxies. It was thus biased against optically faint galaxies that are often rich in H I. More recent data from a blind H I survey by Zwaan et al. (2003) do not have this bias and yield an H I budget twice as large as the previous estimate, i.e. $\Omega_b = (4.2 \pm 0.7) \times 10^{-4}$. Although H I accounts for only $\sim$ 1% of the baryons in the Local Universe (Fukugita, 2004), the study of H I is a powerful tool for obtaining a more complete view of the Universe.

For instance, gas rich systems with faint, or no, optical counterparts which may not have been detected in optical surveys, can be detected in H I. Extreme late-type dwarf galaxies are an example of such systems. These galaxies are gas rich, but optically faint. It is therefore easier and more reliable to obtain redshifts for these galaxies using H I rather than optical spectra (see e.g. Matthews et al., 1995). Low Surface Brightness galaxies (LSBGs) are another class of objects that are traditionally underrepresented in optical

catalogues as they are often fainter than sky brightness. LSBGs are also rich in H I and they are believed to be significant repositories of baryons (in the form of H I) in the Universe (Impey & Bothun, 1997, and references therein). It is therefore important to quantify the amount of gas within these systems using H I observations.

The H I component of a galaxy typically extends further than the optical components (Broeils & Rhee, 1997). H I emission is a an excellent tracer of galaxy interactions and mergers as the gas will be disturbed more easily than the stellar components of the galaxy. It is estimated that 25 % of galaxies showed signs of current or past interaction events (Sancisi, 1999, and references therein). Often, H I is the only galaxy component that shows that an interaction has taken place. A good example of such an interacting system is the M81 group of galaxies, shown in Fig. 1.1. The large spiral galaxy to the right of center is M81, with two dwarf galaxies to the left of it. NGC 3077 is to the lower left and M82 is above M81. The left panel is the optical Palomar Observatory Sky Survey (POSS) image; the right panel is the National Radio Astronomy Observatory (NRAO) H I image. Both images show the central $\sim 1.5^\circ \times 1.9^\circ$ area of the group. It is clear from the radio image that the galaxies are interacting strongly while the optical image shows no sign of interaction within the group.

It has been observed that star formation rates are well correlated with galactic H I content (Kennicutt, 1998). H I data can therefore also be used to study the star formation processes in galaxies. Data obtained from space based instruments such as the Galaxy Evolution Explorer (GALEX)[1] and the Spitzer Space Telescope[2] have made significant contributions to our understanding of star formation in galaxies. GALEX observes galaxies at UV wavelengths. The data from these observations are used to examine star for-

[1] http://www.galex.caltech.edu/

[2] http://www.spitzer.caltech.edu/

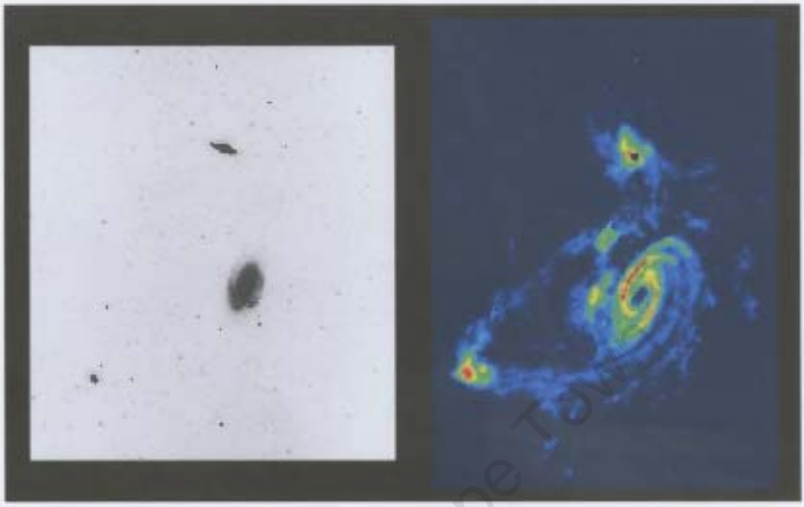

Figure 1.1: *Courtesy of the National Radio Observatory and the Palomar Observatory Sky Survey.* The three interacting members of the M81 group of galaxies. The large spiral galaxy is at the center and to the right is M81, with two dwarf galaxies to the left of it NGC 3077 is lower left and M82 at the upper right. The left panel shows the POSS optical image($1.6^{\circ} \times 1.8^{\circ}$); the panel on the right shows the NRAO HI image ($1.4^{\circ} \times 1.9^{\circ}$).

mation rates and starburst activity within galaxies (e.g. Salim et al., 2005). The Spitzer Space Telescope is an infrared instrument. Infrared data is also used to study star formation activity within galaxies. Infrared photons are not absorbed by dust, thus star formation data can be obtained for regions of galaxies obscured by dust (e.g Pérez-González et al., 2005). By combining data from H I studies as well as UV and infrared star formation research, it will be possible to investigate star formation rates and efficiencies within galaxies as a function of morphological type, gas content, environment and redshift.

A significant advantage of H I observations is that the 21 cm photons are not absorbed by dust. H I observations can probe into regions of space that are obscured by dust. For example, the dust in the Galactic plane obscures 20% of the sky at optical wavelengths (Kraan-Korteweg & Lahav, 2000); it is very difficult to detect objects behind the Galactic plane at these wavelengths. This region of the sky became known as the Zone of Avoidance (ZOA). However, with Radio Astronomy, we are able to study systems behind the ZOA and much progress has been made in mapping the Universe in this region of the sky (e.g. Kraan-Korteweg et al., 2005).

Figure 1.2 shows all sky images at optical (top panel) and H I (bottom panel) wavelengths. Most of the light in the optical image is from nearby stars. The light from the rest of the Galaxy and from systems behind the Galactic plane is obscured by the interstellar dust. The dust appears as dark patches in the image. The H I image shows no obscuration due to interstellar dust; the emission across the center of the image is due to the H I in the Galactic ISM. The galaxies behind the Galactic plane will have H I emission that is redshifted compared to the Galactic emission. These systems can be detected in H I by observing their redshifted H I spectral line emission. Only galaxies with recessional velocities in the range $-200\,\mathrm{km\,s^{-1}} \lesssim v \lesssim 200\,\mathrm{km\,s^{-1}}$ will be more difficult to detect due the Galactic emission.

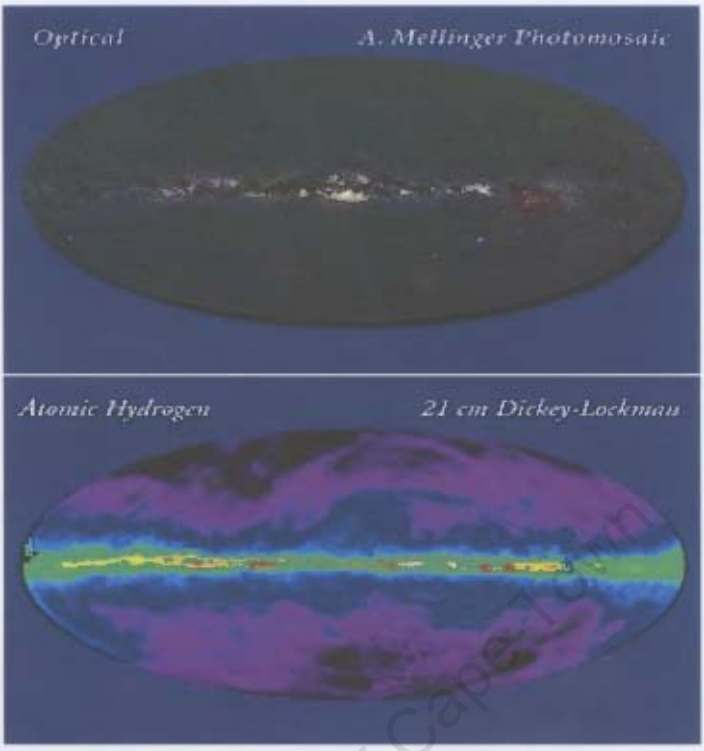

Figure 1.2: *Optical Image:* A. Mellinger, *H1 Image:* Dickey & Lockman (1990). All sky images at optical and radio wavelengths. The top panel is an optical (0.6 μm) image; the bottom panel is an HI image

To gain a better understanding of the HI in the Universe, larger surveys that include all galaxy morphological types are needed. The Square Kilometer Array (SKA)[3] is the most ambitious Radio Astronomy project ever attempted. It will go a long way towards closing the gap in our knowledge of HI. The SKA will be an interferometric radio telescope that will consist of a combination of aperture arrays and more traditional parabolic antennas. The instrument will have a collecting area of 1 million square meters and a frequency range $100\,\mathrm{MHz} \leq \nu \leq 2\,500\,\mathrm{MHz}$. It will be 50 times more sensitive than the current best radio interferometer and it will be able to detect

[3]http://www.skatelescope.org

sources with a redshift $z > 10$.

Until the SKA's completion in 2020, the SKA pathfinders, the Karoo Array Telescope (MeerKAT) and the Australian SKA Pathfinder (ASKAP), can provide further insight into the distribution of H I in the Universe. MeerKAT[4] is the South African SKA pathfinder that is currently being constructed in the Karoo region of South Africa. It will consist of 80×12 m dishes, covering the frequency range $500\,\mathrm{MHz} \leq \nu \leq 2\,500\,\mathrm{MHz}$. ASKAP[5] is under construction in western Australia. This telescope will consist of 30 - 40×12 m antennas with a frequency range of $700\,\mathrm{MHz} \leq \nu \leq 1\,800\,\mathrm{MHz}$. Both these facilities should be fully operational by 2013. The results obtained from smaller H I surveys, such as the one I discuss in §1.2, can then be used to determine what type of science is prioritised for MeerKat, ASKAP and, ultimately, the SKA.

1.1 H I surveys, past and present

Blind and targeted H I surveys provide complementary data. Targeted surveys are able to make deeper, longer observations as integration time will not be spent searching for galaxies. However, blind surveys systematically cover a much larger area of the sky.

Optically selected targeted surveys tend to be biased against optically faint gas rich dwarfs. Five of the six largest targeted H I surveys (see Fisher & Tully (1981); Haynes et al. (1999, 1997); Schneider et al. (1990); Mathewson et al. (1992)) only included spiral or later type galaxies.

Gas poor systems like elliptical galaxies will most likely not be detected

[4]http://www.ska.ac.za

[5]http://www.atnf.csiro.au/projects/askap/

by blind surveys. The bandwidth set up of the telescope's correlator also limits blind surveys in terms of the distance to which they can simultaneously observe. The sensitivity of blind surveys is usually lower than for target surveys due to shorter integration times. The detection rate for blind surveys is then distance dependent; systems with low H I mass will be underrepresented at greater distances.

By using both survey methods, a more accurate view of the H I in the Universe can be achieved.

1.1.1 Blind H I surveys of the Local Universe

Blind H I surveys do not have a pre-defined sample of galaxies to observe. They systematically scan the skies for H I sources. The largest blind H I surveys prior to 2000 were the Arecibo H I survey carried out by Spitzak & Schneider (1998), the H I Strip Survey (Zwaan et al., 1997) and the Nançay survey of the Canes Venatici group region (Kraan-Korteweg et al., 1999). These surveys detected 75, 66 and 33 galaxies respectively. In the last decade Radio Astronomy has advanced rapidly and more extensive surveys of the Local Universe are now being carried out.

The most recently completed large survey is called the H I Parkes All Sky Survey (HIPASS) (Meyer et al., 2004). This survey used the Parkes 64 m telescope which is fitted with 13 circular feed horns, called the Multi Beam receiver. The survey detected 4315 galaxies in the southern skies. Of these galaxies, 26% had no previous optical recessional velocities and 5% had no clear optical counterpart (Doyle et al., 2005). HIPASS also has a northern extension, the Northern HIPASS catalogue (NHICAT) (Wong et al., 2006). A further 1002 galaxies were detected by NHICAT. HIPASS (including NHICAT) observed more than 70% of the sky out to $cz = 12\,700\,\mathrm{km\,s^{-1}}$ with an rms of 13 mJy per beam.

The HIPASS ZOA team carried out a blind H I survey of the ZOA (Kraan-Korteweg et al., 2005; Donley et al., 2005). This survey covered the entire southern Galactic plane and the northern Galactic plane in the regions $|b| \leq 5°$, $192° < l < 212°$ and $36° < l < 52°$. The survey had a maximum recessional velocity of $cz = 12\,700\,\mathrm{km\,s^{-1}}$ and rms = 6 mJy per beam. Close to 1 000 galaxies were detected behind the Milky Way. Fewer than half of the 77 galaxies detected by the northern extension had optical counterparts.

The Arecibo Legacy Fast Arecibo L-band Feed Array (ALFALFA) survey will be the largest blind H I survey. The survey will cover 7 000 square degrees of the sky using the seven-beam L-band feed on the 305 m Arecibo telescope. Started in 2005, ALFALFA is expected to detect over 25 000 extragalactic H I sources, with a median recessional velocity, $cz = 7\,800\ \mathrm{km\,s^{-1}}$ upon its completion on 3 or 4 years. As of May 2008, 60% of the total observations have been completed (Haynes, 2008; Giovanelli, 2008).

These surveys have increased the amount of H I data available, especially in the Southern hemisphere, where few surveys had been carried out previously. They have also revealed large scale structure in the Local Universe, especially behind the Galactic plane. These data can be used to refine structure formation models.

1.1.2 Targeted H I surveys of the Local Universe

Targeted H I surveys select galaxies from pre-existing optical catalogues, selected regions on the sky or galaxy groups to observe. The four biggest surveys detected between 700 and over 2 000 galaxy.

Fisher & Tully (1981) obtained H I spectra for 1171 galaxies with a maximum recessional velocity of $\sim 3\,000\ \mathrm{km\,s^{-1}}$. The observations were carried

out using the 100 m Bonn telescope as well as the 91 m and 43 m telescopes of the NRAO at Green Bank. This sample was selected to include a high number of late type galaxies and it is complete for galaxies of type Sc and later. Redshifts, H I flux and velocity line widths were obtained for each detected galaxy.

The survey carried out by Schneider et al. (1990) yielded 762 detections out to $cz = 12\,000\,\mathrm{km\,s^{-1}}$. This sample consisted of dwarfs and LSBGs. The observations were done with the Arecibo telescope. Forty % of these galaxies had not been detected in H I before.

The largest of these surveys was carried out by Theureau et al. (1998). This survey detected 2112 galaxies out to $cz = 12\,000\,\mathrm{km\,s^{-1}}$ using the Nançay Radio Telescope. The sample consisted of only spiral galaxies. Two hundred and thirteen galaxies within this sample did not previously have measured redshifts. The survey also provided measurements of H I flux and velocity widths for the detected galaxies.

The survey performed by Haynes et al. (1999) detected 1201 galaxies, most of them type Sc, at a maximum recessional velocity $cz \sim 12\,000\,\mathrm{km\,s^{-1}}$. The observations were carried out using 5 telescopes: the Nançay Radio telescope, the 91 m and 43 m telescopes at the NRAO, the 100 m Effelsberg telescope and the Arecibo telescope. Eight hundred and eighty one of these detections had not been detected in H I before. The survey measured line widths, systemic velocities and H I for each galaxy.

A summary of the data for these surveys is presented in Table 1.1. The first column lists the publication in which the survey data was presented, the second column states the limiting recessional velocity of the survey, the third column gives the number of detections and the last column shows the

Table 1.1: Comparison of large targeted H I surveys

Survey reference	V_{max} [km s^{-1}]	N_{det}	Morphology
Fisher & Tully (1981)	3 000	1 171	Mostly late types, only complete for Sc and later types
Schneider et al. (1990)	12 000	762	dwarfs and LSBGs
Theureau et al. (1998)	12 000	2112	Spirals only
Haynes et al. (1999)	12 000	1201	Spirals, mostly Sc

morphological type of the galaxies observed during the survey.

1.2 The Nançay Interstellar Baryon Legacy Extragalactic Survey

The data for thesis consists of the first 1385 observed galaxies of the ongoing Nançay Interstellar Baryon Legacy Extragalactic Survey (NIBLES). The goal of NIBLES is to perform a comprehensive survey of the H I content of a sample of 4 000 optically selected galaxies of all morphological types in the Local Volume, here defined as $900 \leq cz \leq 12\,000$ kms^{-1}, using the Nançay Radio Telescope (NRT). The NRT is a meridian transit telescope with the equivalent collecting area of a 94 m dish (see §2.1.1). The galaxies were chosen from the Sixth Data Release of the Sloan Digital Sky Survey[6] (SDSS) database. The SDSS is an optical imaging and spectroscopic survey that has observed over 280 million objects (Adelman-McCarthy et al., 2008). Both NIBLES and the SDSS are discussed in more detail in §2.1.2.

The primary objective of NIBLES is to accurately quantify the amount of H I gas associated with galaxies in the Local Universe. These data can then be used to decrease the uncertainty related to the H I budget for the

[6]http://www.sdss.org/

Local Universe. Only 13% of the NIBLES galaxies have published H I data, nearly half of which are for bright, spiral galaxies (van Driel, private communication). The NIBLES results will add to the existing pool of H I data for galaxies in the Local Universe by providing systemic velocities, velocity widths and integrated H I line flux values for all the detected galaxies.

NIBLES will investigate the global properties of galaxies. By combining the H I data with the optical and near-infrared data from the SDSS, the gas, stellar and dynamical masses can be determined. By comparing these parameters, inferences can be made about the dark matter content of galaxies. These data can then be used to test cosmological dark matter simulations and models.

The galactic H I content as a function of morphology, stellar mass and stellar density can also be determined. This will provide information on the star formation rates and efficiencies for different galaxy types.

The gas recycling processes in galaxies can be analysed by comparing metallicity to the gas content, stellar mass and dynamical mass of the galaxies. The results of this analysis can be used to constrain models of galactic chemical evolution and galaxy formation.

Another input parameter for galaxy evolution models is the H I Mass function (H IMF) (e.g. Zwaan et al., 2005). The H IMF is the relationship between the number density of galaxies and the galaxy H I mass. The HIMF can be described by the Schechter function (Schechter, 1976):

$$\theta(M_{HI})dM_{HI} = \theta^*(\frac{M_{HI}}{M^*_{HI}})^{\alpha}\exp(-\frac{M_{HI}}{M^*_{HI}})dM_{HI}, \qquad (1.1)$$

where the $\theta(M_{HI})$ gives the space density of the galaxies and θ^* is the normalisation constant. M^*_{HI} is the H I mass at which the H IMF shows a sharp change in slope; i.e. the mass at which the H IMF changes from the expo-

nential form that describes the high mass region to the power law form that describes the low mass region. The parameter α is the slope of the H I MF when $M_{HI} \ll M^*_{HI}$, i.e. α is the slope of the power law.

The H I MF relates the galaxy population of the current epoch to the population predicted by galaxy evolution models. There is still much discord over the value of the H I MF low-mass slope, α, however. The slope varies between -1.2 and -1.5 (see Zwaan et al., 1997; Schneider et al., 1998; Rosenberg & Schneider, 2002; Zwaan et al., 2003). The NIBLES data is very well suited to determining an accurate low-mass slope because roughly 9% of the NIBLES sample consists of faint, low mass galaxies in the luminosity range $M_g \geq -16^{\mathrm{m}}$.

The Tully-Fisher (TF) relation (Tully & Fisher, 1977) can also be determined for the NIBLES sample. The TF relation is the correlation between the maximum rotational velocity of a disk galaxy and its luminosity, predicted as $L \propto V^{\alpha}$. It is frequently used as a galactic distance indicator. Based on observation, α has been found to be $3 \lesssim \alpha \lesssim 4$, with the slope increasing with increasing wavelength (e.g. Aaronson et al., 1979; Verheijen, 2001; Masters et al., 2008). Over 70% of the NIBLES galaxies are disk galaxies, thus providing a large sample with which to perform this analysis.

The large number of spirals and wide luminosity range of the NIBLES sample will allow for an exploration of the TF relation as a function of morphological type. This type of study is of interest as there is evidence to suggest that not all spiral galaxies follow the standard TF relation. A study by Matthews et al. (1998) suggests that extreme late type spiral galaxies do not fit the standard TF relation. These systems appear to be underluminous given their observed rotational velocites and the effect increases with decreasing luminosity and size of the galaxy. This could be due to an increasing dark matter component for these systems. The NIBLES data will

allow us to explore these findings with a sample of small faint spiral galaxies that is nearly twice as large as the one used by Matthews et al. (1998).

The data obtained from NIBLES can also be combined with surveys at other wavebands to improve the estimate of the overall baryon budget for the Local Universe. For example, carbon monoxide (CO) surveys give information not only on the distribution of CO, but on molecular hydrogen (H_2) as well (see e.g. Young & Scoville, 1991). Such a survey will provide information about the distribution of molecular gas in the Local Universe. This data can also be used to study the processes of stellar formation as H_2 is the building block of stars. X-ray surveys provide information on the ionised gas present in the Universe. Warm plasma found in galaxy groups and clusters emits x-rays via free-free electron emission or inverse Compton scattering (Sarazin, 1988, and references therein). By observing the X-ray flux from these sources, one can estimate the amount of ionised material in the Local Universe. By integrating the data from these surveys, a more complete understanding of baryons in the Local Universe can be achieved.

1.3 Thesis outline

The sample of galaxies studied in this thesis consists of the first 1385 NIBLES galaxies. The dataset is made up of the 21 cm line spectra for these galaxies as well as spectroscopic and photometric data from the SDSS for each galaxy.

The primary objective of this project is to determine the global H I characteristics of a sub-sample of the NIBLES galaxies. These early results will allow the NIBLES team to decide which of the science goals will be prioritised and which require further data inspection.

In order to determine the H I properties of the sample the H I Nançay

data were reduced. Quality checks of this data as well as the photometry data obtained from the SDSS were performed. Excising unsuitable or spurious data from the sample is necessary to ensure that accurate results are obtained when the data is analysed. My identification of the pitfalls and areas of concern within the data allows the NIBLES team to optimise the survey. With this optimisation the team can assess whether the goals of the survey can be met and how best to achieve these goals.

Chapter 2 deals with the data acquisition and reduction. The H I data quality control checks as well as a comparison to an existing H I catalogue are presented in Chapter 3. The optical data quality control checks are discussed in Chapter 4 where I investigate various possible causes for a surprising trend in the H I mass to light ratio for this sample of galaxies. Conclusions and future prospects are put forward in Chapter 5.

Chapter 2

Observations and Data Reduction

In this chapter I present the data selection criteria and acquisition procedures used for this thesis and describe the data reduction methods that were applied.

First, a detailed description of the Nançay Radio Telescope, the instrument used to collect the radio data, is given. The instrument is a decimetric radio telescope that can detect the radiation emitted in frequency bands around 3 330 MHz, 1 665 MHz and 1 420 MHz. For our purposes, the telescope was used to detect radiation emitted by neutral hydrogen in nearby galaxies ($cz < 12\,000\,\mathrm{km\,s^{-1}}$), hence a frequency close to 1 420 MHz.

Neutral hydrogen is observed by detecting the so-called "21 cm" spectral line emission; this spectral line is more commonly referred to as H I emission. These photons are emitted when the spins of the proton and electron that make up neutral hydrogen make a transition from being parallel to anti-parallel. This is known as the hydrogen hyperfine transition. The change in energy from the spin-parallel configuration to the spin-anti-parallel configuration is 5.88×10^{-6} eV. To conserve energy, a photon with a wavelength of

21.1 cm is released, corresponding to a frequency of $\nu_{HI} = 1420.41$ MHz (see e.g. Foot, 2005).

2.1 Data acquisition

2.1.1 The Nançay Radio Telescope

The selected galaxies were observed using the Nançay Radio Telescope (NRT). It is situated near the town of Nançay, France. The telescope is a transit instrument. It consists of two large reflectors made from a metal mesh with square holes 12.5 mm across and has a surface accuracy of 5 mm rms.

The primary reflector is flat, 200 m long in the East-West direction and 40 m in height. It can be rotated about a horizontal axis to point at the desired declination. The second reflector is fixed at a distance of 460 m from the first. It is spherical, 300 m long and 35 m high, with a radius of 560 m. The NRT has an effective collecting area equivalent to that of a 94 m parabolic dish (approximately 7 000 m^2). Figure 2.1 shows a schematic cross section of the NRT configuration. Incoming radiation is reflected off the flat primary reflector onto the spherical reflector. The radiation is then focused by the spherical reflector onto the receivers in the carriage.

The receivers are situated in a carriage between the two mirrors. To track the radio source as it moves across the sky, the receiver carriage moves along a curved, 100 m long rail track (see e.g. Monnier Ragaigne et al., 2003). Sources near the equator can be observed for approximately 1 hour; the maximum daily integration time increases with increasing declination as $1/cos(\delta)$.

The half-power beam width (HPBW) in the East-West direction is 3.6′ at a wavelength of 21 cm. Due to the shape of the telescope, the beam diameter is much larger in the North-South direction and increases with declination,

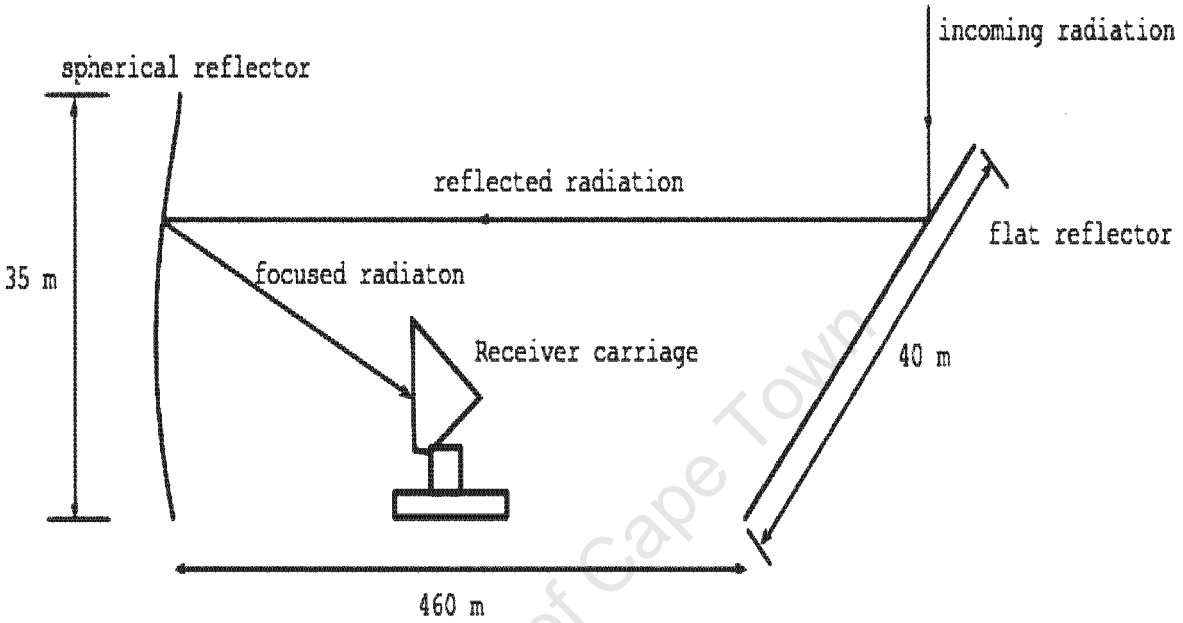

Figure 2.1: Schematic diagram of the NRT showing the flat and spherical reflectors and the receiver carriage.

rising from 22′ at δ=0°to 32′ at δ=70° (Matthews & van Driel, 2000).

The telescope's effective collecting area and gain are also influenced by this declination effect. For $\delta > 20°$ the collecting area decreases with increasing declination (Fouqué et al., 1990). As the primary reflector is pointed towards higher declinations, the radiation reflected back towards the secondary decreases. This in turn means that the effective collecting area (or effective aperture), and thus the aperture efficiency, ϵ_{ap}, decreases as $1/cos(\theta)$, where ϵ_{ap} is the ratio of the effective aperture to the physical aperture and θ is the angle between the horizon and the direction of the primary reflector .

For example, for a source near the horizon $\theta \sim 0°$, the effective aperture is approximately equal to the physical aperture of the telescope and $\epsilon_{ap} \sim 1$. For a source at the zenith, $\theta = 45°$ and $\epsilon_{ap} = \frac{1}{\sqrt{2}}$.

The gain, G, is related to ϵ_{ap} as follows (Kraus, 1986):

$$G = \frac{4\pi}{\lambda^2} A_p \epsilon_{ap} \tag{2.1}$$

where λ is the wavelength in m and A_p is the physical aperture of the telescope in m^2. The gain therefore decreases with increasing declination due to its dependence on ϵ_{ap}.

For our purposes, the telescope was used in position switching or total power mode. Each galaxy was observed for roughly 30 minutes. In this mode, an observation consisted of successive 40 s ON-source and 40 s OFF-source pointings, with OFF-source pointings taken 20′ E of the target galaxy. The OFF-source pointings are taken so that the sky's contribution to the signal can be determined and subtracted from the spectrum (see §2.2.1).

The autocorrelator was split into two cross-polarized receiver banks. Each

bank used a 50 MHz bandpass with 4 096 channels, centered on 5 000 km s^{-1} for sources with $cz \lesssim 9\,000$ km s^{-1} and 10 000 km s^{-1} for $cz \gtrsim 9\,000$ km s^{-1}. This results in a channel spacing of 2.6 km s^{-1} and a total velocity range of approximately 10 500 km s^{-1} for the respective central velocities.

2.1.2 Sample selection

SDSS selection criteria

The target galaxies for this study were selected from the Sloan Digital Sky Survey (SDSS) sixth data release[1] (Adelman-McCarthy et al., 2008). SDSS is a flux-limited optical, spectro-photometric galaxy survey and the largest project of this kind. The survey aims to map a quarter of the sky; observing millions of galaxies and quasars. This will provide a detailed three dimensional census of the objects found in the Universe.

The SDSS makes use of a unique set of five broad filter bands called *u,g,r,i,* and *z*. These filters were optimized so that the photometric redshifts of galaxies could be more easily determined (Bessell, 2005). The limiting magnitudes for the main galaxy sample are 22^{m}, 22.2^{m}, 22.2^{m}, 21.3^{m} and 20.5^{m} in the *u,g,r,i,* and *z* bands respectively (Adelman-McCarthy et al., 2007). The sample has a median redshift of $z = 0.104$ (Strauss et al., 2002). The project uses a 2.5 m telescope situated at Apache Point in New Mexico, USA.

The SDSS spectroscopic survey has observed over 1.2 million galaxies (Adelman-McCarthy et al., 2008). The selection criteria for the spectroscopic sample are based on the *r* band magnitudes of the galaxies. This large sample necessitates an automated, reliable target selection algorithm. Moreover, the algorithm should produce an accurate and robust galaxy selection function:

[1] http://www.sdss.org/dr6/

it should not create biases against any particular type of galaxy, e.g. low surface brightness galaxies, and it should be based on meaningful physical galactic parameters, such as surface brightness. Lastly, the algorithm should operate in a straightforward way that makes it easy to troubleshoot and test.

Taking these points into consideration, the SDSS team decided to use a modified form of the Petrosian magnitude definition (Petrosian, 1976) in the selection algorithm. This system determines the galactic flux within an aperture that is defined by the ratio of the surface brightness within an annulus centered on that aperture to the surface brightness within the aperture; called the "Petrosian ratio", $\Re(\theta)$. The size of the aperture is determined by the shape of the radial surface brightness profile, but not the amplitude (Strauss et al., 2002). $\Re(\theta)$ is given by Strauss et al. (2002) as:

$$\Re(\theta) = \frac{2\pi \int_{0.8\theta}^{1.25\theta} I(\theta')\theta' d\theta' / \{\pi[(1.25\theta)^2 - (0.8\theta)^2]\}}{2\pi \int_0^{\theta} I(\theta')\theta' d\theta' / \pi\theta^2} \tag{2.2}$$

where θ is the angular distance from the galaxy centre and $I(\theta)$ is the azimuthally averaged galactic surface brightness profile. The thickness of the annulus (0.8θ - 1.25θ) was chosen so that $\Re(\theta)$ would be insensitive to small fluctuations in $I(\theta)$ and noise.

The Petrosian radius, θ_P, is then defined by Strauss et al. (2002) as:

$$\Re(\theta) = f_1, \tag{2.3}$$

where $f_1 = 0.2$. This value of f_1 is chosen to make $\Re(\theta)$ insensitive to seeing fluctuations. It also keeps the difference in apertures for de Vaucouleurs surface brightness profiles and exponential profiles to a minimum.

Lastly, the Petrosian flux is (Strauss et al., 2002):

$$F_P = 2\pi \int_0^{f_2\theta_P} I(\theta')\theta' d\theta' \tag{2.4}$$

where $f_2 = 2$ and $f_2\theta_P$ is called the Petrosian aperture. The value of f_2 is low enough so that the influence of sky noise on F_P is minimal, but high enough that $f_2\theta_P$ contains almost all the flux for a typical surface brightness profile.

Instead of elliptical apertures, SDSS uses circular apertures because it is more complicated to select elliptical apertures for galaxies with light distributions that are not well characterised by concentric ellipses. The surface brightness profile of disk galaxies within a circular aperture is less inclination-dependent than the elliptical aperture surface brightness profile. This seems counterintuitive as one would expect an elliptical aperture to produce a better fit to the galaxy shape as inclination increases. However, because the Petrosian aperture is big enough to contain most of the galactic flux, the ratio of Petrosian flux to total flux is not dependent on inclination (Strauss et al., 2002).

The SDSS selection criteria for the spectroscopic sample of galaxies are as follows (Strauss et al., 2002):

- A galaxy will enter the sample if it has an r band ($\sim 6\,300\,\text{Å}$) signal 5σ above the sky brightness.
- The galaxies must have an r band Petrosian magnitude $r \leq 17.77^{\text{m}}$ and a mean surface brightness, μ_{50}, within the Petrosian half light radius (R_{50}) of $\mu_{50} \leq 24.5\,\text{mag/arcsec}^2$, where R_{50} is the Petrosian radius containing half of the galaxy's total Petrosian flux.
- For the lowest surface brightness galaxies, with $23 \leq \mu_{50} \leq 24.5\,\text{mag/arcsec}^2$, an extra selection criterion is implemented to eliminate spurious sources. Within this surface brightness range substructures within a galaxy are often identified as galaxies. It has been determined that the nearby

sky brightness, μ_{local}, for these sources is slightly higher (due to the parent galaxy) than the average global sky brightness, μ_{sky}. They can therefore be eliminated if $\mu_{local} - \mu_{sky} \geq 0.05^{\rm m}$.

- Other galaxies that do not meet the above surface brightness criteria were included in the sample as well, if they have r band fiber magnitudes, $m_f < 19^{\rm m}$ (where m_f is the flux within the opening of a spectroscopic fiber with a diameter of $3''$), as they will probably still produce acceptable spectra (i.e. spectra with a signal-to-noise ratio of S/N > 4 pixel^{-1} (Adelman-McCarthy et al., 2007)). A low surface brightness galaxy with a strong nucleus and $cz < 10\,000\,{\rm km\,s^{-1}}$ can enter the sample in this way.

- Galaxies are rejected if they have a Petrosian magnitude $r < 15^{\rm m}$ and $R_{50} < 2'$ and if $m_f < 14.5^{\rm m}$ in the i band or $m_f < 15^{\rm m}$ in the r or g bands. This is done to avoid saturating the spectroscopic CCDs and to reduce crosstalk with neighbouring spectroscopic fibres. This last criterion leads to the rejection of only 0.07% of real mostly nearby bright sources.

The NIBLES selection criteria

The 4 000 galaxies selected for NIBLES were chosen from 56 000 Local Volume SDSS galaxies, i.e. galaxies with recessional velocities in the range $900\,{\rm km\,s^{-1}} < cz < 12\,000\,{\rm km\,s^{-1}}$, henceforth called the LV SDSS sample. The automated photometry system of SDSS does not provide accurate photometry for galaxies of large angular size, so very nearby sources with $cz < 900\,{\rm km\,s^{-1}}$ were not selected. Despite this being an H I survey, all morphological types were included in the sample (van Driel et al., 2007). The NIBLES selection criteria also require that the galaxies have a good quality optical SDSS spectrum (S/N $> 4\,{\rm pixel^{-1}}$).

The LV SDSS sample includes galaxies with a wide range of z band (9 000 Å) magnitudes, with -10$^{\rm m}$ $\geq M_z \geq$ -24$^{\rm m}$ (using a Hubble constant of $H_0 = 70\,{\rm km\,s^{-1}}$). The NIBLES sources were chosen in a way that samples this luminosity range as uniformly as possible. Previously, most of the large, optically selected H I surveys included mainly bright spiral galaxies in their samples (e.g. Theureau et al., 1998; Fisher & Tully, 1981). By sampling such a large magnitude range, NIBLES will provide a more accurate view of galaxy properties over a wide range of luminosities.

The NIBLES sources are assigned to M_z luminosity bins with a width of $\Delta m = 0.5^{\rm m}$. The bins with luminosities from -10.5$^{\rm m}$ $\geq M_z \geq$ -14.0$^{\rm m}$ and M_z = -24.0$^{\rm m}$ each contain between 30 and 161 galaxies. The remaining bins contain a maximum of 200 sources each (see Fig. 2.7 for distribution of this sample of galaxies). The low number of galaxies in the faint bins reflect the low numbers of faint galaxies in the LV SDSS sample. Even though the faint galaxy numbers are low in comparison to bright galaxies, the numbers are still better than for previous surveys. With these numbers of galaxies per bin, one is able to carry out robust statistical analyses of the galaxies as a function of various galaxy properties, such as surface brightness, even for faint sources. It will later be found that this distribution changes significantly due to magnitude estimate errors (see §4).

The nearest galaxies in our sample were observed preferentially as they would have the highest chance of being detected in H I. The mean distance for the luminosity range -10.5$^{\rm m}$ $\leq M_z \leq$ -19$^{\rm m}$ is 30 Mpc, with 55 Mpc for -19.5$^{\rm m}$ $\geq M_z \geq$ -21$^{\rm m}$ and 100 Mpc for the remaining brightest sources.

The observations were scheduled by Prof. W. van Driel and Nicole Hallet of the Nançay Observatory. They were carried out by the Nançay technical staff. The data were reduced and analysed by myself.

2.1.3 Calibration

A radio telescope's receiver output is not in units of radiation flux density. Rather, the raw output is a measure of the telescope's system temperature, T_{sys} in units of K, where T_{sys} is given by:

$$T_{sys} = T_{astro} + T_{terr} + T_{rec} \tag{2.5}$$

where T_{astro} includes contributions from large scale astronomical sources such as the cosmic microwave background, radio sources within our own galaxy and solar system, and the target radio source; T_{terr} consists of radio emissions reflected from the ground into the receiver and atmospheric emissions and T_{rec} is the temperature contribution from various parts of the of the receiver.

It is therefore necessary to remove the extraneous temperature contributions and convert the signal output of the targeted source from units of temperature to units of flux density.

The contributions from astronomical as well as terrestrial sources are removed by using the position switching method mentioned in §2.1.1. The temperature contribution from the sky obtained during the OFF-source pointing contains the T_{terr} term and the T_{astro} without the contribution from the targeted radio source.

To remove the receiver temperature, T_{rec}, the terminal resistance of the receiver is placed in liquid nitrogen or helium so that its noise temperature is precisely known and kept to a minimum. Then a radio source of known flux is inserted into the receiver horn and T_{rec} is determined. This procedure is carried out between observations of the sky.

After subtracting each contribution, the remaining temperature is then due to the targeted radio source. This temperature, called the brightness temperature T_b, is related to the flux density as follows (Taylor et al., 1999):

$$T_b = F_c S, \tag{2.6}$$

where T_b is the brightness temperature in K, S is the flux density in Jy and F_c is the temperature to flux density conversion factor given by:

$$F_c = \frac{c^2}{2k_B \nu^2 \Omega}, \tag{2.7}$$

where ν is the observed frequency in Hz, k_B is the Boltzmann constant and Ω is the solid angle subtended by the beam on the sky in steradians; it is approximated as (Taylor et al., 1999):

$$\Omega = \frac{\pi \theta_{HPBW}^2}{4 \ln 2}, \tag{2.8}$$

where θ is the beam dimension in arcseconds and HPBW is defined to be the angular size of the main beam at the half power level.

F_c is calculated by observing astronomical radio sources with known flux densities and then measuring the corresponding system temperature which allows the ratio of temperature to flux density to be calculated. For the NRT, F_c= 1.4 K Jy^{-1} at $\delta = 0°$ at a wavelength of 21 cm and $T_{sys} = 35$ K.

2.2 Data Reduction

The data reduction was carried out using two software packages created by the NRT staff, called the NAnçay Processing Software (NAPS) and Système Interactif de Réduction (SIR) respectively.

2.2.1 NAPS

The NAPS software package was used to remove as much of the Radio Frequency Interference (RFI) from the raw data as possible. The RFI mitigation

algorithm is as follows (Monnier Ragaigne et al., 2003):

1. All the OFF-source spectra for an observation were averaged and this average OFF spectrum, <OFF>, was subtracted from each individual ON-source spectrum for that observation.

2. For every ON-<OFF> spectrum, the signals with the 25% highest and 25% lowest peaks were excised and the average rms and mean signal strength were calculated.

3. In each of these spectra, channels with signal strengths differing by more than 10 σ from the mean rms were flagged. The signal was replaced by a linear interpolation between the unaffected channels. There is the chance that legitimate H I signals with very high flux density will be clipped at this stage. However, because this procedure is being carried out on each individual, 40 s integration spectrum, the H I profiles usually have a flux density that is below this threshold. In the entire sample $< 3\%$ of the spectra had clipped profiles.

4. The cleaned ON spectra were then averaged and subtracted from each OFF spectrum.

5. Steps 2 and 3 were then repeated for each OFF spectrum and clean OFF-source spectra were produced. This is done to remove RFI from the OFF-spectra so that it is not re-introduced into the ON-spectra in the next step.

6. Lastly, the average of the clean OFF-source spectra was subtracted from each original, uncleaned ON-source spectrum. This creates the final, cleaned ON spectra that were used in the rest of the reduction procedures.

Despite this mitigation procedure, some RFI still remains in the spectra. The most troublesome RFI was the GPS signal at 1 381.1 MHz which often

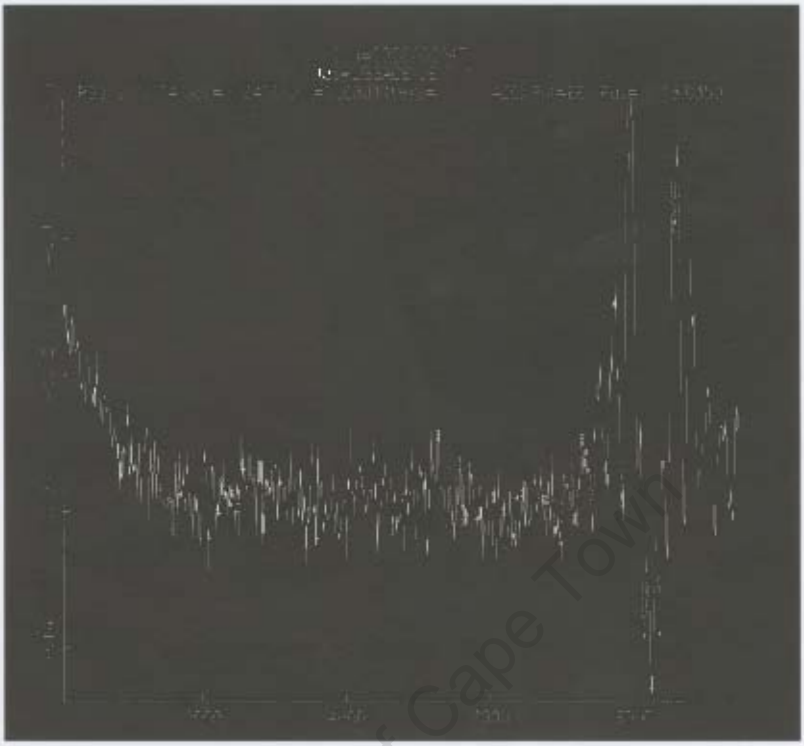

Figure 2.2: The H I spectrum of SDSS002347.66-003939.3 showing a strong GPS signal. The horizontal axis is in units $\mathrm{km\,s^{-1}}$ and the vertical axis is in units of Jy. The GPS covers a wide range of velocities, $8\,000\,\mathrm{km\,s^{-1}} \lesssim v_{GPS} \lesssim 9\,000\,\mathrm{km\,s^{-1}}$ and causes severe ringing in the baseline on either side of it.

resulted in a strong signal at the equivalent of $8\,200\,\mathrm{km\,s^{-1}}$. As an example, Fig. 2.2 shows a strong GPS signal in the spectrum of SDSS002347.66-003939.3. The horizontal axis is in units of $\mathrm{km\,s^{-1}}$ and the vertical axis is in units of Jy. In Fig 2.3 (as well as 2.4, 2.5 and 2.6) the baseline is not at the zero flux level because the baseline normalisation has not yet been performed; the normalisation happens only after the residual baseline has been subtracted (see §2.2.2). The GPS covers a broad range of the baseline, $8\,000\,\mathrm{km\,s^{-1}} \lesssim v_{GPS} \lesssim 9\,000\,\mathrm{km\,s^{-1}}$. The baseline of the spectrum is affected by severe ringing on either side of the RFI.

Next, the NAPS programme was used to convert the raw data (system temperature in K) to flux density (in Jy) using the conversion factor, F_c. Following these procedures, a spectrum of the data from each receiver bank was produced by adding all the final cleaned ON-source spectra. The spectra were then displayed and bad spectra were identified by eye and flagged.

2.2.2 SIR

The SIR package was used to extract H I parameters such as the recessional velocity and integrated flux density from the data of likely galaxy candidates. To start this process the name of the galaxy was entered into the programme and each spectrum obtained for that galaxy was displayed individually. I selected by eye which spectra to use in the analysis. These spectra were then added together to produce one final spectrum of the galaxy. As an example, Fig. 2.3 shows the final spectrum of SDSS 032009-061549.1. The horizontal axis is in units of $\mathrm{km\,s^{-1}}$ and the vertical axis is in units of Jy. This spectrum contains a double horn profile, typical of an inclined spiral galaxy, with S/N = 18.7 and strong RFI at $9\,500\,\mathrm{km\,s^{-1}}$ of unknown origin. This RFI was not removed by the RFI mitigation algorithm because it fell below the 10σ threshold set for each 40 s integration spectrum. The signal at $0\,\mathrm{km\,s^{-1}}$ is due to residual Galactic H I emission.

We then selected a section of the spectrum with a typical width, $\Delta v = 5\,000\,\mathrm{km\,s^{-1}}$, centered on the signal. In the case of non-detections, we chose the region where the signal would have been expected, according to the recessional velocity obtained from the SDSS data. Next, the signal and any RFI were marked off on the spectrum by clicking on either side of them. Figure 2.4 shows the truncated spectrum containing the H I spectral line, but with the RFI and Galactic emission excised. The red line underneath the spectral line (just below the velocity axis) indicates that it has been flagged by the user. This selection indicates to the programme that the spectral line

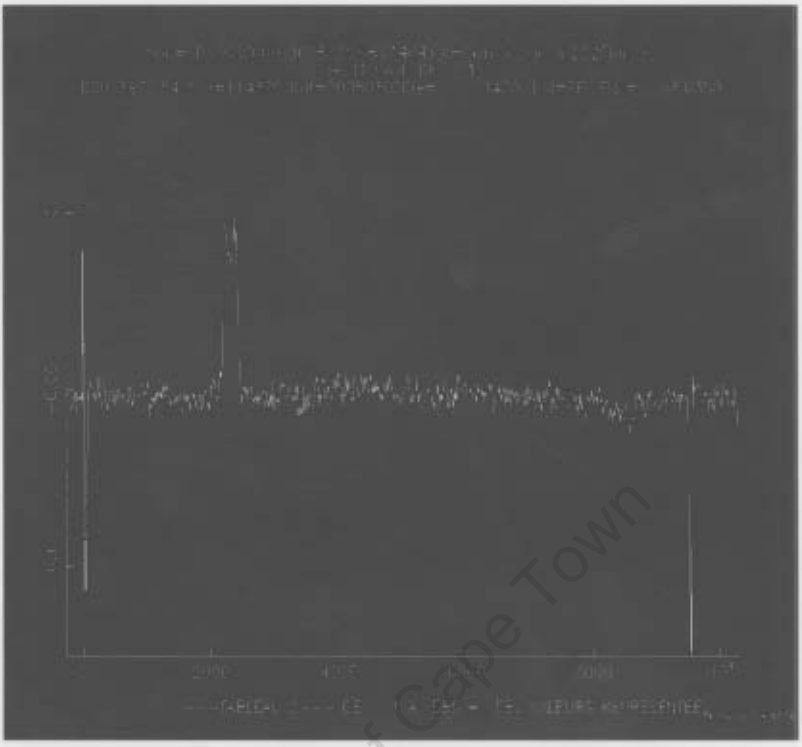

Figure 2.3: The spectrum of SDSS 032009-061549.1 as it is displayed in SIR. The horizontal axis is in units of $\mathrm{km\,s^{-1}}$ and the vertical axis is in units of Jy. The spectrum contains a good double horn profile of S/N = 18.7. It also shows strong RFI at $9\,500\,\mathrm{km\,s^{-1}}$ of unknown origin. The signal at $0\,\mathrm{km\,s^{-1}}$ is due to residual Galactic H I emission.

should not be removed during baseline subtraction.

The residual baseline subtraction was carried out by fitting a 5^{th} order polynomial to the data; this is shown in Fig. 2.5. This relatively high order was used as the residual baselines have many ripples. The sections that were marked as the signal and RFI were replaced by linear interpolations so that they would not be subtracted. The data were then box-car smoothed to a resolution of $18\,\mathrm{km\,s^{-1}}$ to improve the signal to noise ratio (Theureau et al., 1998). The resolution was set to $18\,\mathrm{km\,s^{-1}}$ to minimise the uncertainty in the recessional velocity and velocity width values.

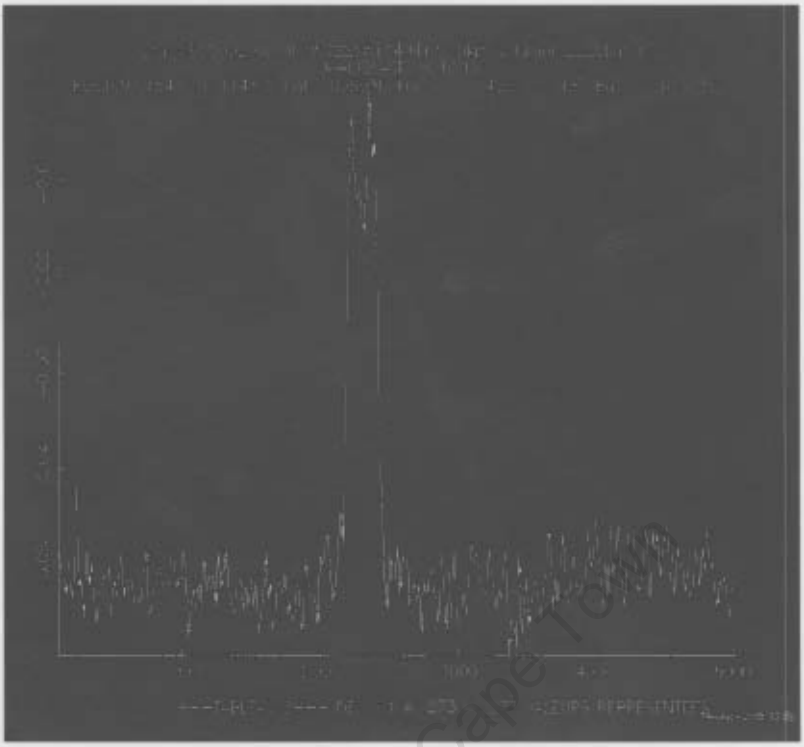

Figure 2.4: This figure shows the section of the spectrum, with the signal in the center and RFI excised. The red line indicates where the signal has been marked off on the spectrum.

Lastly, we selected the maximum intensity of the signal. Double-horned profiles are often asymmetric; in these cases the maximum intensity is then chosen to be the mean peak flux of the two horns. The programme then automatically determined H I parameters such as integrated line flux, S_{int}, central velocity, V_{HI} and velocity widths. Figure 2.6 shows the spectrum after the residual baseline subtraction and smoothing. The bottom-most horizontal line is the average baseline, the middle and top lines are the 20% and 50% levels of the maximum peak flux. These levels are used to calculate the velocity widths, W_{50} and W_{20} at the 50% and 20% levels.

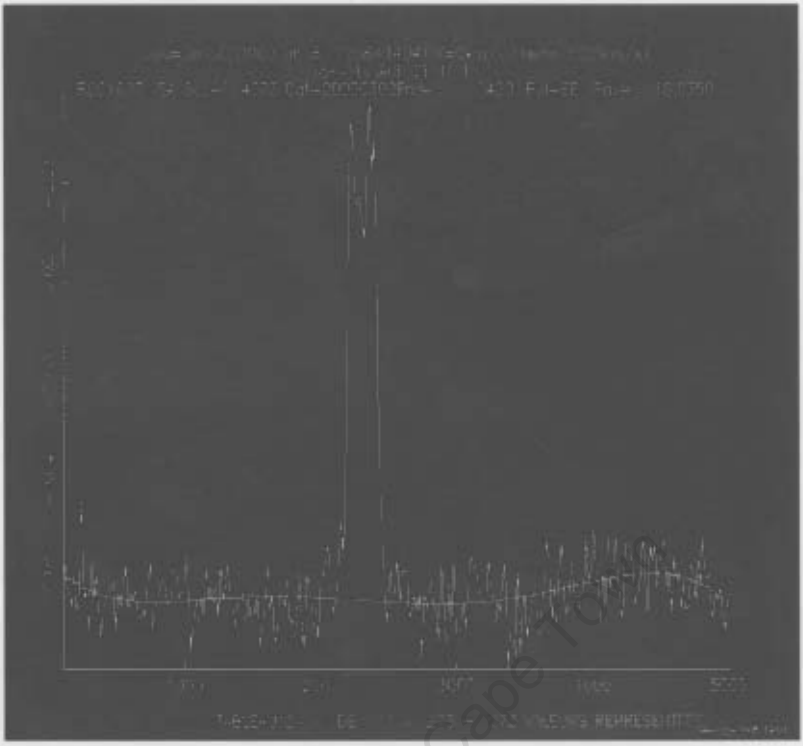

Figure 2.5: The 5th order polynomial that has been fitted to the baseline of the spectrum.

2.3 Results

The data that form part of this thesis were collected between February 2007 and March 2008. In total, about 900 hours of telescope time were used and 1 385 galaxies could be observed. Of the 1 385 galaxies, 806 were detected and 579 were not. Figure 2.7 shows the histogram of all the galaxies within the sample (yellow bars) and the galaxies detected in H I (red bars).

Figure 2.8 shows an equal-area projection of the sky distribution of the galaxies observed in this period in equatorial coordinates. The red circles represent the H I detected galaxies and the blue crosses represent H I non-detections. The voids at $63^{\circ} < \alpha < 110^{\circ}$ and $265^{\circ} < \alpha < 309^{\circ}$ are due to the Galactic plane. The three narrow strips in the southern galactic cap are

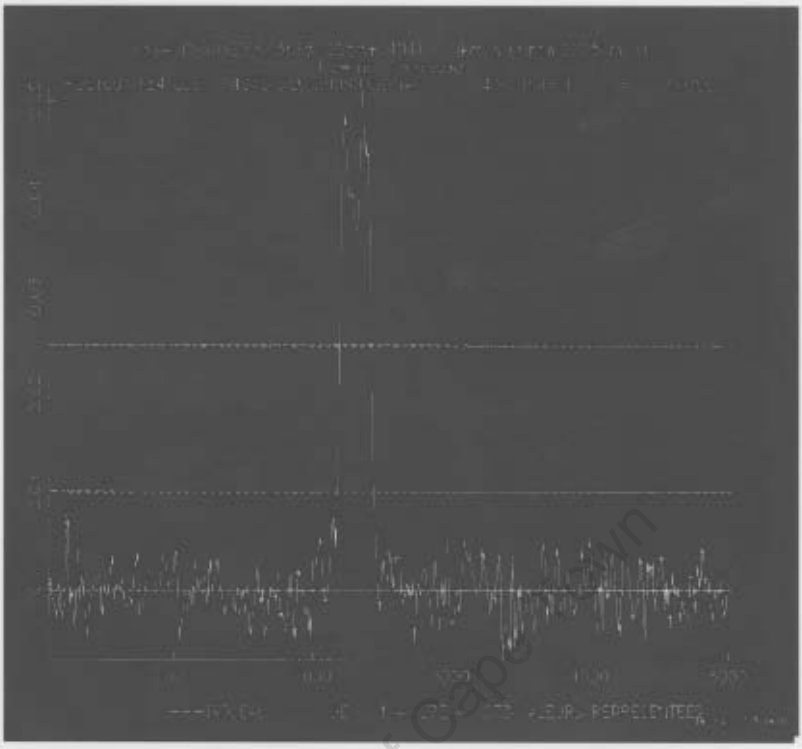

Figure 2.6: The smoothed spectrum after baseline subtraction. The bottom horizontal line is the average baseline for the spectrum. The middle and top lines indicate the 20% and 50% levels of the maximum peak flux.

part of the SDSS Legacy survey. The region between $120^\circ \lesssim \alpha \lesssim 240^\circ$ and $+10^\circ \lesssim \delta \lesssim +20^\circ$ is only sparsely populated because the SDSS survey has not completed observations of that area of the sky.

For comparison with Fig. 2.8, the equal area projection of all the galaxies in the SDSS spectroscopic survey sample is shown in Fig. 2.9. The curving, black solid line represents the Galactic plane. The main survey region, centered at $\alpha \sim 200^\circ$ and $\delta \sim 30^\circ$ and the three southern stripes are all part of the SDSS Legacy survey. The red areas are part of the Sloan Extension for Galactic Understanding and Exploration (SEGUE). The blue regions (or "special" plate regions) indicate sources that are part of the main survey,

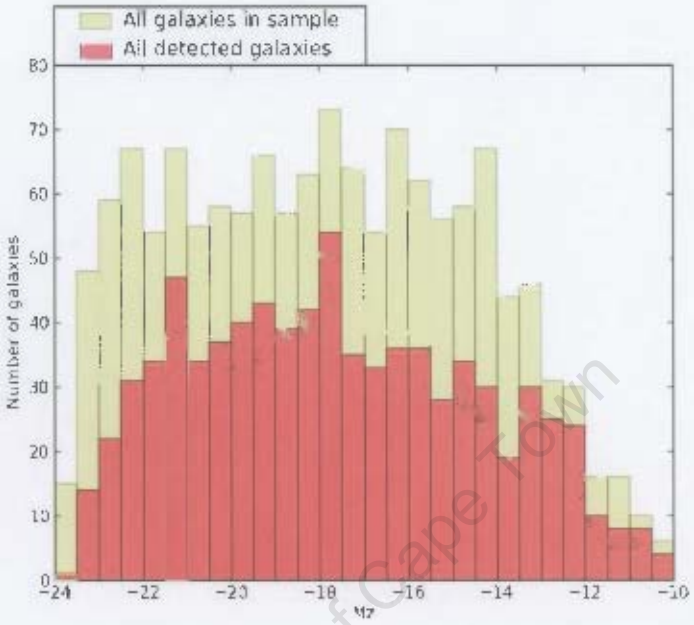

Figure 2.7: Histogram of all galaxies within the sample (yellow bars) and galaxies detected in H I (red bars).

but have been chosen for further investigation, such as the study of Galactic kinematics (Adelman-McCarthy & et al., 2005).

The average rms for the sample was 3.22 mJy for 30 minute integration times. The mass detection limit, i.e. the average minimum H I mass the survey will detect can be calculated by using the average values of the sample in the H I mass equation:

$$M_{HI} = 2.36 \times 10^5 D^2 S_{int} \tag{2.9}$$

where D is the distance of the galaxy in Mpc ($H_0 = 70\,\mathrm{km\,s^{-1}\,Mpc^{-1}}$) and S_{int} is the integrated flux of the detection in $\mathrm{Jy\,km\,s^{-1}}$. We assume that a 3σ detection of a given velocity width will be detected.

This implies a mass detection limit of $8.3\times10^8\,\mathrm{M_\odot}$ for $F = 3\sigma$, D= 45 Mpc and $\Delta V = 180\,\mathrm{km\,s^{-1}}$; the distance and velocity width are average values for the sample.

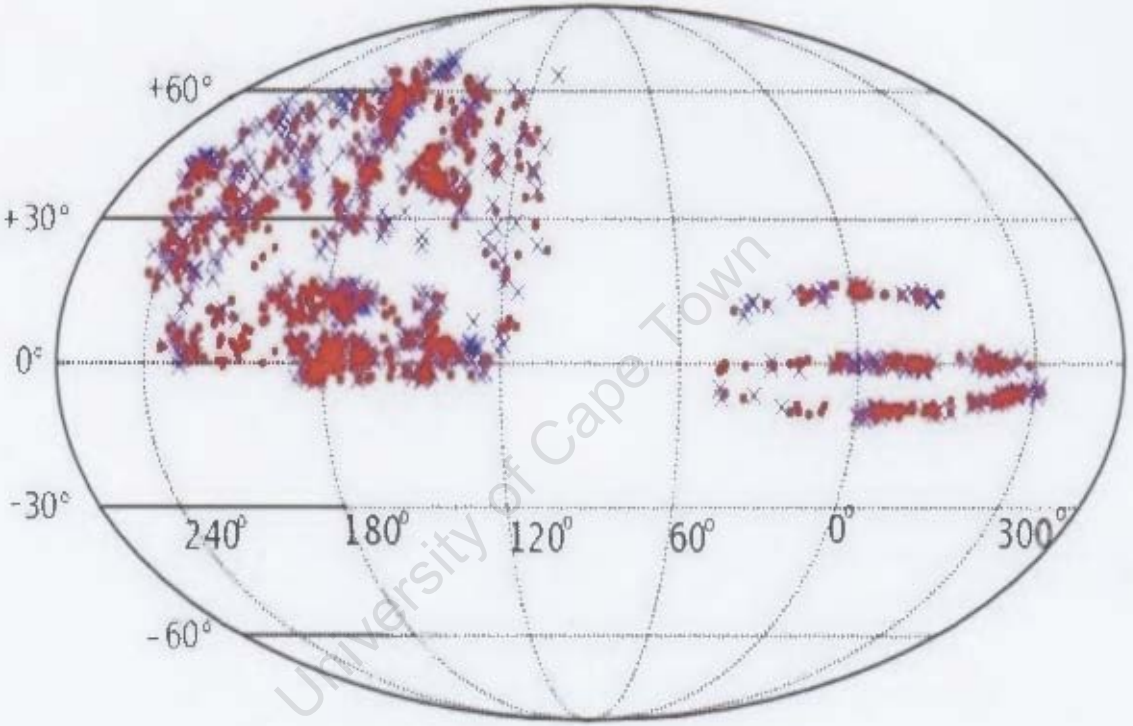

Figure 2.8: An equal-area projection of the sky distribution of the observed galaxies in equatorial coordinates obtained from the Sloan Digital Sky Survey Data Release 6. The red circles indicate H I detections, the blue crosses non-detections. The voids at $63^\circ < \alpha < 110^\circ$ and $265^\circ < \alpha < 309^\circ$ are due to the Galactic plane. The three strips in the southern galactic cap are part of the SDSS Legacy survey. The contiguous region of galaxies is centered at about $\alpha = 13\,\mathrm{h}\ 21\,\mathrm{m}$ and $\delta = 30^\circ$.

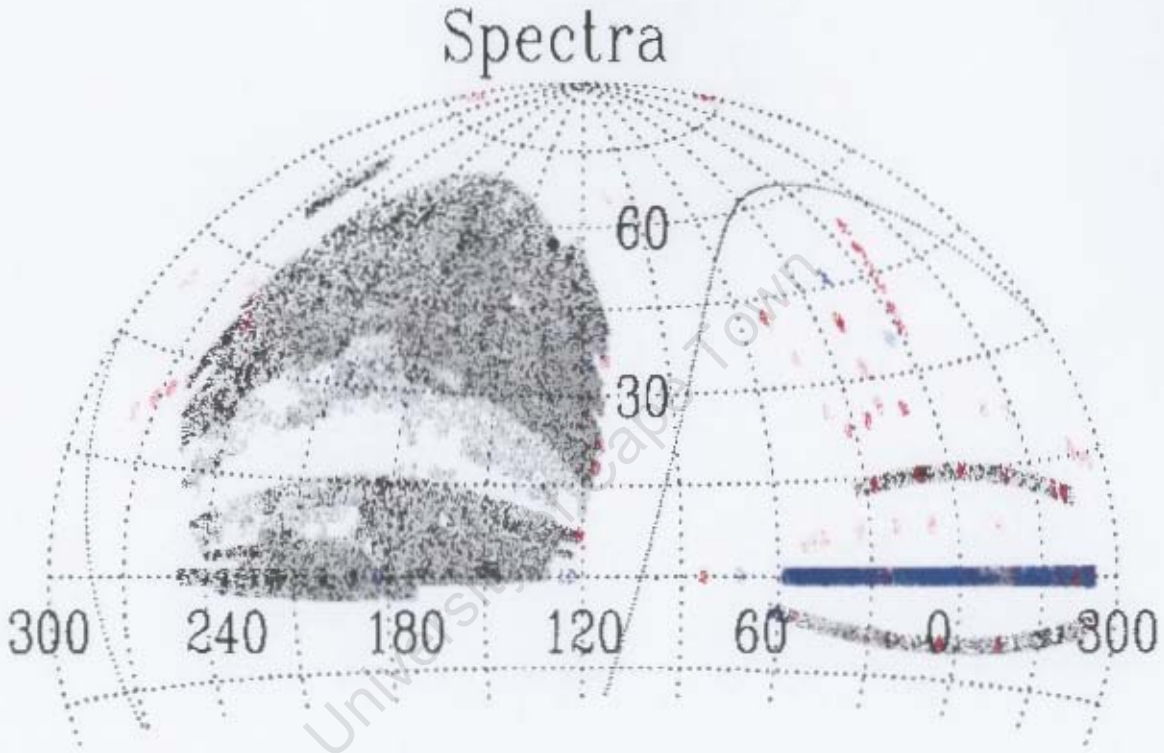

Figure 2.9: The equal area projection of all the galaxies in the SDSS sixth data release spectroscopic survey in equatorial coordinates. The solid line presents the Galactic plane. All the galaxies surveyed, including those in the three southern strips, are part of the SDSS Legacy survey. The red symbols are for galaxies in the SEGUE survey. The blue areas indicate the special plate regions. *Image*: Adelman-McCarthy et al. (2008)

Chapter 3

H I data results and quality control

Before we began the detailed analysis of the data obtained from the sub-sample of the NIBLES survey, we first needed to check the data quality. The catalogue of derived H I parameters are given, followed by a comparison to data from an existing H I catalogue, The Northern Extension of the H I Parkes All Sky Survey (Wong et al., 2006).

3.1 H I data for this sample of galaxies

This sample of galaxies consists of 1385 observations with a mean rms of 3.22 mJy. Two hundred and forty three galaxies in the sample are optical "confusion" sources. Optical confusion sources are objects that are listed in the SDSS database as galaxies, but they are actually substructures within galaxies . The data for these confused sources were not included in the catalogue of parameters (for a full discussion see §4.1.2).

Eight hundred and six of the observed galaxies were detected, but not all of these detections are reliable. A reliable detection is one with peak flux, $S_{peak} \geq 3\sigma$, where σ is the rms for that particular observation. After excis-

ing confusion sources and detections with $S_{peak} < 3\sigma$, the total number of reliable detections is 600.

An extract of the catalogue of H I parameters is shown in Table 3.1. The parameters listed are: recessional velocity (V_{HI}) in $\mathrm{km\,s^{-1}}$, the rms in mJy, the velocity widths at the 50% (W_{50}) and 20% (W_{20}) peak flux level in $\mathrm{km\,s^{-1}}$, the peak flux (S_{peak}) in mJy, the integrated flux (S_{int}) in $\mathrm{Jy\,km\,s^{-1}}$ and the H I mass (M_{HI}) in solar masses. The full catalogue of H I parameters for this sample of galaxies can be found in Appendix A. Note that an entry of zero in the W_{20} or W_{50} columns indicates that the parameter was not recorded.

S_{peak} is selected manually by clicking on the point of maximum flux on the galaxy spectrum in SIR (see §2.2.2) if the line profile is Gaussian. For a double horned profile, the peak flux is chosen to be average of the two peaks. W_{50} (W_{20}) is the difference between the velocities that correspond to the 50% (20%) peak flux level. V_{HI} is the mean velocity of the region of spectrum chosen for the line flux measurement (see §2.2.2). S_{int} is the area under the line profile. M_{HI} is derived using Eqn. 2.9.

3.1.1 Multiple detections

The NRT has a large beam size in the North-South direction ($\delta \sim 22' - 30'$). This makes it likely that multiple sources are detected during an observation. During the reduction process, each H I galaxy spectrum was inspected for multiple H I detections in a single spectrum. These spectra were flagged and separately investigated.

There are two types of multiple detection that can occur within a target spectrum:

Table 3.1: Example of the catalogue of H I parameters for this sample of galaxies

Coordinates (J2 000) hhmmss degrees	V_{HI} [km s^{-1}]	rms [mJy]	W_{50} [km s^{-1}]	W_{20} [km s^{-1}]	S_{peak} [mJy]	S_{int} [Jy km s^{-1}]	log M_{HI} [M$_\odot$]
00 01 03.6 +14 34 48.6	1679	2.32	32	48	6.96	0.14	7.3
00 02 14.8 +14 29 16.0	5053	2.71	175	201	12.74	1.77	9.4
00 03 15.0 +16 08 44.7	1064	2.18	463	489	26.38	9.98	8.7
00 03 44.3 +16 11 12.7	6265	2.67	232	290	11.21	1.97	9.6
00 06 19.6 +14 19 38.7	5330	2.66	14	77	9.31	0.15	8.3
00 06 29.3 +14 10 56.4	5654	2.53	136	247	10.37	1.11	9.3
00 07 01.6 +14 06 23.6	5320	2.72	205	284	9.79	0.98	9.1
00 08 34.3 −10 56 57.5	8842	2.85	110	135	41.04	4.29	10.2
00 08 48.8 +14 02 01.3	1902	2.56	98	117	24.32	2.05	8.6
00 12 14.7 +15 15 26.7	1861	2.31	53	64	7.85	0.43	7.9
00 13 38.6 +15 40 28.0	1952	3.18	129	144	22.26	0.69	8.1
00 13 44.0 +00 22 18.2	3926	2.71	120	176	9.49	0.75	8.8
00 20 09.3 +14 17 28.7	4713	2.15	171	190	11.83	1.4	9.2
00 21 51.2 −09 29 32.1	6130	2.4	299	309	9.6	1.49	9.5
00 27 49.7 −01 11 59.9	3846	2.77	235	249	29.92	4.98	9.6
00 30 07.3 −11 06 49.1	3477	2.65	325	342	21.47	4.68	9.5
00 30 09.0 −09 57 11.8	5059	2.85	206	330	10.55	1.56	9.3
00 30 29.8 −08 46 59.8	5236	2.83	260	293	15.28	2.67	9.6
00 33 22.1 −01 07 16.7	1976	2.55	144	168	103.02	13.15	9.4
00 34 02.8 −09 42 19.2	3706	2.69	449	467	51.38	15.92	10.0
00 34 57.9 −09 20 31.9	6709	2.76	339	420	10.49	2.12	9.7
00 36 28.9 −10 06 22.1	5777	2.52	307	351	13.1	2.65	9.7
00 37 10.6 −09 27 25.1	5172	2.32	147	227	12.3	1.23	9.2
00 39 22.9 −08 49 24.4	5672	2.91	228	277	10.77	1.28	9.3
00 41 33.9 −10 01 17.1	3851	1.6	539	564	9.12	2.08	9.2
00 43 32.4 +14 20 33.2	4387	2.38	205	225	18.56	3.29	9.5
00 43 51.9 +00 48 07.0	5358	2.74	228	259	19.29	3.34	9.7
00 44 23.3 +14 17 15.7	4115	2.46	77	104	10.09	0.54	8.7
00 45 51.9 −09 19 41.5	6007	2.77	166	219	12.74	1.65	9.5
00 46 08.8 −10 24 31.0	3919	2.69	148	178	9.15	0.54	8.6
00 47 46.4 −09 50 06.1	5640	3.04	430	0	10.64	2.11	9.5
00 47 47.5 −09 53 58.3	1344	5.07	132	166	99.37	13.06	9.1
00 51 59.6 +00 29 12.1	1612	2.79	175	192	82.58	11.59	9.2
00 52 52.8 +01 12 50.4	1754	2.53	94	124	9.61	0.7	8.0
00 53 29.9 −08 46 04.0	5517	2.62	167	224	9.43	1.05	9.2
00 56 42.7 −09 54 49.9	5552	2.75	199	225	80.85	15.32	10.4
00 57 56.6 +00 52 08.9	2263	2.95	91	121	13.28	0.94	8.4
01 00 04.1 −11 04 57.3	5323	2.64	142	224	27.46	3.87	9.7
01 00 45.8 −09 11 08.5	4507	2.78	144	298	36.42	5.82	9.8
01 01 19.5 −09 50 42.9	4495	2.41	242	260	7.95	1.25	9.1

- both the target galaxy and what appears to be an extra galaxy are detected.
- the detection may not be due to the target galaxy, but a second galaxy.

In this sample of galaxies, only 3 of the spectra contained what appeared to be an extra detection. Six detections are due to galaxies that are not the target galaxy. The data from these 9 spectra were not included in the analysis. The profiles with extra detections cannot be used in analysis because the profiles appear to be overlapping (see Fig. 3.1). It is then not possible to isolate the flux due to the target galaxy only. The detections caused by galaxies other than the target galaxy are not used because the detected galaxy is not in the NIBLES sample.

The NASA Extragalactic Database[1] (NED) was searched to try to identify the possible sources causing the extra detections. A search for galaxies within a radius of $\sim 15'$ (the maximum angular separation between galaxies in the beam if the target is at the center of the beam) was performed. Any galaxy that fell within this search area with a redshift corresponding to the extra detection was noted as a possible source of the extra detection.

Next, the SDSS finding chart website[2] was used to try and identify any extra galaxies that fell within the NRT beam during observation of the target galaxy. The finding chart tool displays SDSS colour images of galaxies. The pixel scale and angular size of these images can be set by the user. For my purposes, the image dimensions were set equal to the maximum dimensions of the NRT beam, i.e. $\alpha \times \delta \sim 4' \times 30'$. Using these images, I was then able to view all galaxies that fell within the NRT beam during an observation.

The extra galaxy that appeared in the SDSS image was then compared to the NED images of the galaxies that were noted as possible sources of

[1] http://nedftp.ipac.caltech.edu/

[2] http://cas.sdss.org/astrodr6/en/tools/chart/chart.asp

the extra detection. If the galaxy in the NED image matched the galaxy in SDSS image, then the galaxy was chosen as the source of the extra detection.

Figure 3.1 shows examples of spectra where multiple signals are present. The black lines in both spectra indicate the recessional velocity of the target galaxy. In the left panel the spectrum of SDSS151505.2+421233.9 is presented. The signal profile looks like the typical double horned profile of an inclined spiral galaxy, but with two smaller peaks on either side. This unusual shape is thought to be due to two overlapping double horned profiles, one wider than the other, at the same redshift.

The right panel of Fig. 3.1 shows the spectrum of SDSS133011.5−013947.2. This profile has a triple horned shape. This shape is also most likely due to overlapping signals of galaxies with similar redshifts.

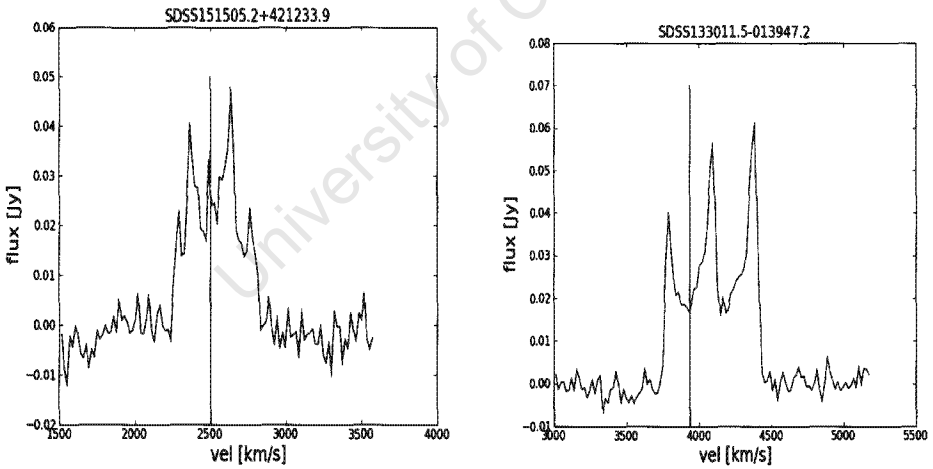

Figure 3.1: Spectra of galaxies that appear to have two detections per spectrum. The left panel shows the spectrum of SDSS151505.16+421233.9. The right panel shows the spectrum of SDSS133011.49-013947.2. The black lines on both spectra indicate the recessional velocity of the target galaxies.

The SDSS finding chart images of SDSS151505.2+421233.9 and SDSS133011.5−013947.2 are shown in Fig. 3.2. SDSS151505.2+421233.9 is centered in the left and SDSS133011.5−013947.2 is centered in the right panel. Each image has the same dimensions as the NRT beam, $\alpha \times \delta = 4' \times 22'$. The galaxy causing the extra flux in the profile is clearly visible below the target galaxy in both images.

Table 3.2 lists the galaxies that have multiple signals in their spectra as well as the most likely candidate galaxy for the source of the second signal. The first column gives the names of the target NIBLES galaxies, the second column contains the description of the profile and third column lists the optical recessional velocity of the target galaxy. The fourth column lists the name of the most likely source of the second detection; the optical recessional velocity of these galaxies are given in the fifth column. The last column contains the reference code for the velocities.

Table 3.2: Galaxies with multiple detections per spectrum

Target galaxy	profile description	V_{opt} [km s^{-1}]	Likely 2^{nd} galaxy	V_{opt} [km s^{-1}]	Ref
SDSS133006.1-014314.1	triple horned signal	4 317	NGC 5184	3 991	2
SDSS133011.5-013947.2	triple horned feature	3 937	NGC 5183	4 290	1
SDSS151505.2+421233.9	four peaks in profile	2 499	NGC 5899	2 562	3

References: [1] Fisher et al. (1995),[2] Catinella et al. (2005), [3] de Vaucouleurs et al. (1991)

Figure 3.3 illustrates the second type of multiple detection. The left panel shows the spectrum of SDSS081753.93+244112.0. There is a strong signal at $v \sim 2\,000\,\mathrm{km\,s^{-1}}$. The recessional velocity of the target galaxy is $v = 1\,701\,\mathrm{km\,s^{-1}}$ (as indicated by the black vertical line), but this signal is not detected. The right panel shows the spectrum of SDSS140711.34+550006.0. The black line indicates the recessional velocity of $v = 1\,918\,\mathrm{km\,s^{-1}}$. There

Figure 3.2: SDSS colour images showing extra galaxies in the NRT beam. The image has the dimensions of the NRT beam, i.e $\alpha \times \delta = 4' \times 22'$. The left panel is centered on SDSS151505.2−421233.9; the right panel is centered on SDSS133011.5-013947.2

is no detected signal from the target galaxy, but there is a strong signal at

$v \sim 1\,400\,\mathrm{km\,s^{-1}}$.

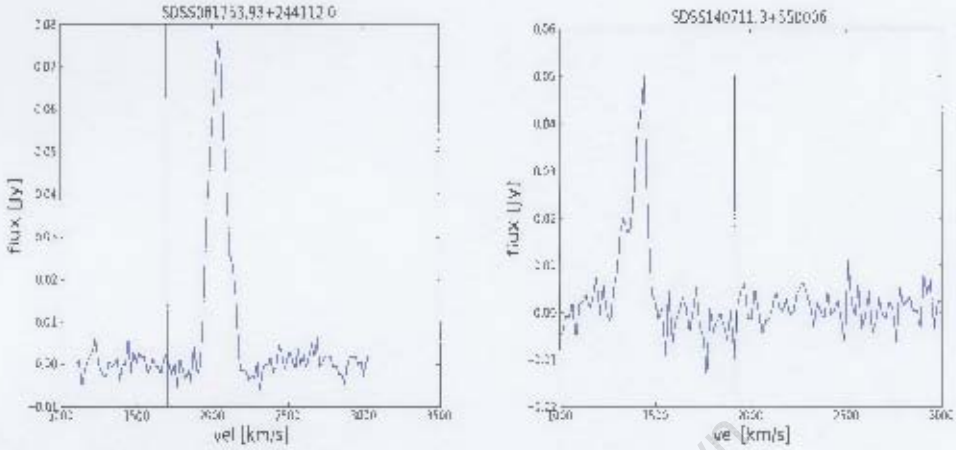

Figure 3.3: The spectrum of SDSS081753.93−244112.0 (left panel) shows no detection at the recessional velocity ($v = 1\,701\,\mathrm{km\,s^{-1}}$) of the galaxy, but there is a strong signal at $v \sim 2\,000\,\mathrm{km\,s^{-1}}$. SDSS140711.34+550006.0 (right panel) has a recessional velocity of $v = 1\,918\,\mathrm{km\,s^{-1}}$. No signal is detected at that velocity, but there is a clear detection at $v \sim 1\,400\,\mathrm{km\,s^{-1}}$. The black line shows the recessional velocity of the target galaxy.

Figure 3.4 shows SDSS081753.9+244112 (left panel) and SDSS140711.3+550006 (right panel) centered in each image. Each image has the dimensions of the NRT beam. The galaxies responsible for the detections are above and to the left of the target galaxies.

The list of galaxies that were not detected, but which have another galaxy detection in the spectrum is presented in Table 3.3. The table lists the target SDSS galaxy in the first column and the optical recessional velocity of the target in the second. The name of the most likely second galaxy is contained in the third column and the optical recessional velocity of this galaxy is shown in column four. The fifth column contains the reference code for the recessional velocity of the second galaxy.

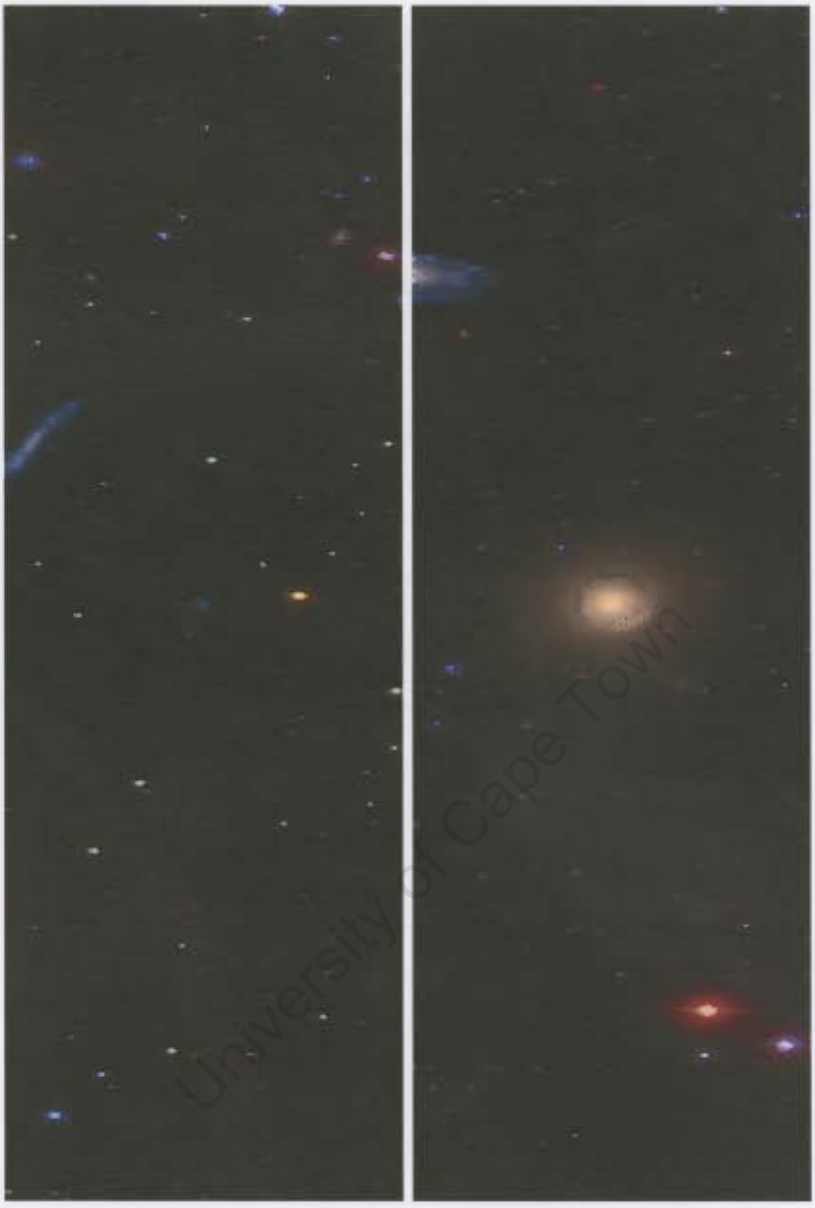

Figure 3.4: SDSS colour images showing extra galaxies in the NRT beam. The image has the dimensions of the NRT beam, i.e $\alpha \times \delta = 4' \times 22'$. The left panel is centered on SDSS081753.9+244112; the right panel is centered on SDSS140711.3+550006

3.2 Comparison of H I parameters

3.2.1 NHICAT H I data

The H I data for the pilot NIBLES survey were compared to data from the Northern H I Parkes All Sky Survey Catalogue (NHICAT) (Wong et al., 2006)

Table 3.3: Undetected galaxies with an H I detection originating from another source

Target galaxy	V_{opt} [km s^{-1}]	Other galaxy	V_{opt} [km s^{-1}]	Ref
SDSS081753.9+244112.0	1 701	IC 2267	2 044	4
SDSS084809.2+173641.3	6 178	IC 2406	4 670	5
SDSS122203.9+090205.6	996	NGC 4307A	5 836	7
SDSS124342.3+113329.5	1 022	NGC 4647	1 422	6
SDSS140050.0+493059.8	1 522	UGC 08936	1 907	8
SDSS140711.3+550006.0	1 918	NGC 5486	1 390	3

References: [3] de Vaucouleurs et al. (1991), [4] Falco et al. (1999), [5] Paturel et al. (2003), [6] Binggeli et al. (1985), [7] Meyer et al. (2004), [8] Smoker et al. (2000)

in order to verify the consistency and accuracy of the NIBLES data. The NHICAT data were chosen for comparison with the NIBLES data because the survey areas overlap and the surveys have a similar redshift range.

NHICAT was a blind H I survey that detected 1 002 galaxies in the declination range $+2° < \delta < +25°\,30'$ and one source just below $\delta = 2°$. The observations were taken during the period from 2 000 to 2 002 using the multibeam receiver on the 64 m Parkes radio telescope. The integration time was 450 s beam^{-1} resulting in a survey sensitivity of 14 mJy beam^{-1}. The survey velocity range is $-1\,280\,\mathrm{km\,s^{-1}} < v < 12\,700\,\mathrm{km\,s^{-1}}$. Galaxies in the range $-300\,\mathrm{km\,s^{-1}} < v < 300\,\mathrm{km\,s^{-1}}$ were omitted to avoid high levels of Galactic emission.

The declination range for NIBLES is $-11°\,9' < \delta < +68°\,42'$. There are no observations in the right ascension ranges $4°\,11' < \alpha < 7°\,19'$ and $17° < \alpha < 20°\,54'$ as these coordinates correspond to the Galactic Plane. Therefore not all galaxies in the NIBLES sample fall within the NHICAT survey area. In total, 210 detected galaxies fall within both the NHICAT and NIBLES survey areas.

NHICAT has a positional accuracy of 1.5′. A source in NIBLES was matched to a source in NHICAT if they were within 1.5′ of each other and the difference between their recessional velocities, $\Delta V_{HI} < 100\,\mathrm{km\,s^{-1}}$. Twenty-five galaxies were matched in this way. The compared parameters are V_{HI}, the rms, S_{peak}, S_{int}, W_{20} and W_{50}.

The velocity widths for NHICAT were determined using both a maximisation and a minimisation procedure. The minimisation procedure starts at the velocity corresponding to the peak profile flux and searched outward until the desired peak flux level is found. The maximisation procedure searches inward from the edges of the profile until the required flux level is reached. The NIBLES velocity widths are determined by simply finding the velocities corresponding to the required flux level. It was found that the NIBLES data matched the maximised parameter most closely and these velocity widths are listed in Table 3.4. V_{HI} in NHICAT is measured in several ways. The parameter that is recommended for use by the NHICAT team (and the one that is listed in Table 3.4) is called v_{50}^{max}. This parameter is the mean velocity at which the profile reaches 50% peak flux when using the maximisation procedure. S_{peak} is the maximum flux density within the profile. S_{int} is the integrated flux density within the area between the manually selected profile velocity limits and the data box size (see Meyer et al., 2004, §3.2.2).

Table 3.4: NIBLES and NHICAT data comparison

SDSS name	V_{HI} [km s^{-1}]	rms [mJy]	W_{50} [km s^{-1}]	W_{20} [km s^{-1}]	S_{peak} [mJy]	S_{int} [Jy km s^{-1}]
HIPASS name	V_{HI}	rms	W_{50}	W_{20}	S_{peak}	S_{int}
SDSS001338+154028	1952	3.2	129	144	22.3	0.7
HIPASSJ0013+15	1925	6.4	142	171	30.3	3.3
SDSS013015+144039	2427	5.2	118	147	38.3	3.7
HIPASSJ0130+14	2450	7.8	118	...	59.9	6.4
SDSS101358+070126	1210	2.8	211	235	145.3	26.7
HIPASSJ1013+07	1216	52.9	217	241	215.8	37.7
SDSS101414+032759	1213	2.5	422	482	138.4	47.1
HIPASSJ1014+03	1223	9.0	438	505	329.2	118.2
SDSS101747+215224	1579	2.9	211	246	40.0	7.4
HIPASSJ1017+21	1570	6.6	191	272	61.3	9.6
SDSS104207+134449	1306	2.8	304	344	170.3	42.7
HIPASSJ1042+13	1309	62.3	332	359	413.6	91.7
SDSS105539+022347	1026	2.5	97	135	21.2	2.0
HIPASSJ1055+02	1043	7.7	85	...	37.7	3.6
SDSS112426+112031	1051	2.3	255	273	102.4	24.9
HIPASSJ1124+11	1061	77.4	265	288	202.5	42.2
SDSS112824+092427	1733	2.5	402	420	31.8	7.6
HIPASSJ1128+09a	1743	6.9	410	437	72.3	14.0
SDSS113419+131919	1194	2.9	66	111	51.1	4.0
HIPASSJ1134+13	1198	6.8	73	98	48.7	3.4
SDSS113737+163322	1029	3.1	153	182	57.8	7.8
HIPASSJ1137+16	1029	6.6	142	173	66.1	7.3
SDSS120110+140613	1492	2.9	199	223	44.2	7.7
HIPASSJ1202+14	1477	6.9	136	214	95.8	13.0
SDSS121127+025534	1272	3.3	95	117	78.7	6.8
HIPASSJ1211+02b	1295	45.3	95	114	78.4	6.7

Table 3.4 continued ...

SDSS name	V_{HI} [km s^{-1}]	rms [mJy]	W_{50} [km s^{-1}]	W_{20} [km s^{-1}]	S_{peak} [mJy]	S_{int} [Jy km s^{-1}]
HIPASS name	V_{HI}	rms	W_{50}	W_{20}	S_{peak}	S_{int}
SDSS124356+130736	1044	2.3	283	312	120.6	30.2
HIPASSJ1243+13b	1058	112.2	278	314	255.2	51.8
SDSS124745+134546	1612	2.8	183	203	29.9	4.78
HIPASSJ1247+13	1633	7.8	163	186	47.9	6.2
SDSS131652+123253	960	2.9	165	199	61.9	9.9
HIPASSJ1316+12	966	124	173	193	64	10.1
SDSS132032+052429	950	3.3	72	161	14.2	1.1
HIPASSJ1320+05	962	14.7	86	115	58.9	4.9
SDSS132038+094710	1122	3.1	139	156	70.7	8.9
HIPASSJ1320+09	1134	45.3	150	...	112.2	15.5
SDSS143039+071630	1351	3.0	180	206	78.4	13.1
HIPASSJ1430+07	1354	32.8	183	217	144.1	19.8
SDSS143324+042701	1571	2.9	106	132	196.1	19.5
HIPASSJ1433+04	1581	6.8	100	128	438.1	42.5
SDSS144058+021111	1621	2.4	145	166	24.4	3.2
HIPASSJ1440+02	1638	6.0	124	170	30	3.4
SDSS144257+045327	1633	2.4	307	323	71.5	16.6
HIPASSJ1443+04	1649	8.0	305	330	94.4	21.3
SDSS154544+203337	2075	2.7	60	84	103.6	6.6
HIPASSJ1454+20	2092	7.4	70	101	126	9.2
SDSS160817+073218	1360	2.7	209	228	59.9	11.0
HIPASSJ1608+07	1370	7.7	215	238	96.3	14.8
SDSS225810+141830	2105	3.0	103	129	50.9	5.0
HIPASSJ2258+14	2113	6.6	109	155	74.8	7.6

Figure 3.5 shows the comparison of the NIBLES and NHICAT *rms* values. The high NHICAT *rms* values are for sources with $\delta > 10\,^{\circ}$. These high high declinations mean that the observations are taken at lower elevations and this increases the solar interference, which in turn raises the *rms* of the observations.

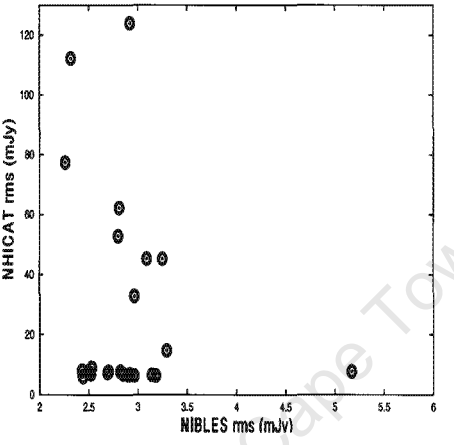

Figure 3.5: Comparison of NIBLES and NHICAT *rms*.

The data for V_{HI} and W_{50} Table 3.4 are plotted in Fig. 3.6. The NIBLES data for V_{HI} (left panel) and W_{50} (right panel) are well matched to the NHICAT data. The black lines on both plots are the lines of equality. The rms scatter for V_{HI} and W_{50} in these plots is $12\,\mathrm{km\,s^{-1}}$ and $17\,\mathrm{km\,s^{-1}}$ respectively. The NIBLES spectra were boxcar smoothed to a resolution of $18\,\mathrm{km\,s^{-1}}$. The NHICAT team used Hanning smoothing in their reduction process resulting in a resolution of $26.4\,\mathrm{km\,s^{-1}}$. V_{HI} and W_{50} are in good agreement given the velocity resolutions of the two surveys and the data show no systematic variations..

The comparisons of S_{peak} and S_{int} are plotted in Fig. 3.7. The black lines in both plots are the lines of equality. There are large disparities between the

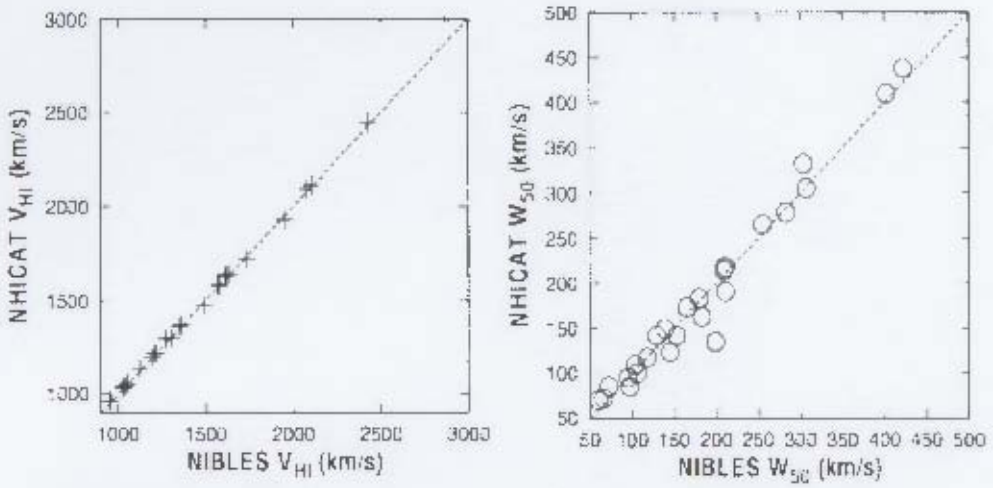

Figure 3.6: Comparisons of V_{HI} (left) and W_{50} (right).

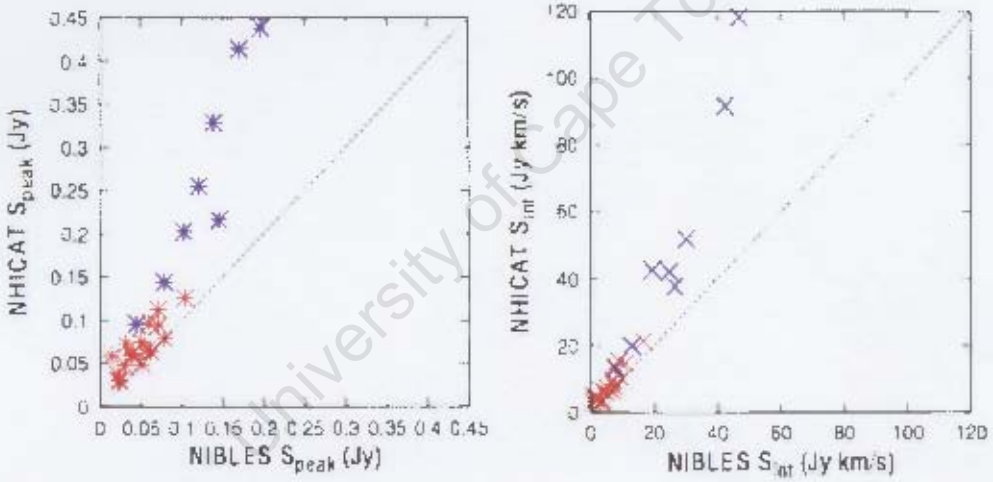

Figure 3.7: Comparisons of S_{peak} (left) and S_{int} (right). The purple symbols represent the extended sources and the red symbols represent the non-extended sources.

data for both S_{peak} (left) and S_{int} (right). The large differences in S_{peak} and S_{int} between the two datasets is due to the extended angular size of some of the galaxies (represented by the purple symbols in the plot). The NRT beam is $\sim 4'$ in the East-West direction. Therefore galaxies with $R_{HI} \sin(PA) > 2'$

will be resolved by the NRT beam, where PA is the position angle of the galaxy measured eastward of North and R_{HI} is the H I radius of the galaxy. R_{HI} is estimated to be $\sim 2R_{opt}$ (Broeils & Rhee, 1997), where R_{opt} is the optical radius of the galaxy. Since the NIBLES survey only used one pointing of the NRT to observe a source, some galaxies, particularly nearby spirals, will be larger than the observing window and will therefore not have a complete flux measurement. This leads to an underestimation of the flux of the galaxy. For the 25 galaxies compared in Table 3.4, 8 were extended compared to the East-West diameter of the NRT beam. The data for S_{peak} and S_{int} presented in Table 3.4 are therefore lower limits on the total values. The extended NIBLES sources will be re-observed using multiple pointings at a later stage. For NHICAT, extended sources were manually identified and their flux values were re-determined by summing the flux in each pixel of the moment map (see Meyer et al., 2004, §3.5). This difference in observational methodologies will result in different parameter distributions for the two galaxy samples.

Figure 3.8 displays the histograms of the W_{50} (top panel), S_{peak} (middle panel) and S_{int} (bottom panel) parameters for the NIBLES sample and the NHICAT sample. In all three plots the darker shading indicates NIBLES data and the lighter shading corresponds to the NHICAT data.

The distribution of W_{50} is skewed towards lower values for the NIBLES sample because NIBLES detected a higher number of low mass systems, such as dwarf galaxies. The NHICAT integration time is too short to allow detection of these low mass objects with narrow profiles.

The histograms of S_{peak} are shown in the middle panel of Fig. 3.8 (in the discussion that follows, the logarithmic values of S_{peak} and S_{int} are given in parentheses so that the values can more easily be related to Fig.3.8). The NIBLES data include many more systems with low peak flux values ($S_{peak} <$ 0.03 (-1.5) Jy) than NHICAT. NIBLES detected more low flux systems be-

cause the integration time per source is roughly 30 minutes, compared to 7.5 minutes beam^{-1} for the NHICAT sample. The underestimation of the flux of extended sources leads to a paucity of galaxies with $S_{peak} > 0.32$ (-0.5) Jy in the NIBLES sample.

The bottom panels of Fig. 3.8 show the histograms of the integrated flux densities, S_{int}, for the NIBLES sample and the NHICAT sample. Again, the impact of not completely observing extended sources is evident in the NIBLES data. The NIBLES sample has more galaxies with $S_{int} < 3.16$ (0.5) Jy km s^{-1} because there are more sources with narrow profiles and low peak flux values within the sample. The NHICAT data has many more sources with $S_{int} > 31.2$ (1.5) Jy km s^{-1} due to its larger number of galaxies with high peak flux values.

Two effects that lead to a difference between NIBLES and NHICAT flux distributions have been discussed; lower mass galaxies observed by NIBLES due to its longer integration time and higher mass galaxies that have underestimated flux in NIBLES if they are extended sources. In order to quantify these two effects, the histograms of W_{50}, S_{peak} and S_{int} for the galaxies listed in Table 3.4 are shown in the top, middle and bottom panels Fig. 3.9 respectively.

The histogram of W_{50} in Fig. 3.9 shows no significant difference between the NIBLEs and NHICAT data. The S_{peak} data shows that NHICAT has 5 more sources than NIBLES with $S_{peak} > 0.20(-0.7)\,Jy$. NIBLES has 4 sources with $S_{peak} < 0.03(-0.7)\,Jy$ more than NHICAT. The effect of underestimating galaxy flux then seems slightly more pronounced than the effect of longer integration time, but with such a small sample this observation may not be statistically significant. For the S_{int} data, NIBLES has 3 more sources than NHICAT with S_{int} <3.2 (0.5) Jy km s^{-1} and NHICAT has 3 more sources than NIBLES with S_{int} <31.2 (1.5) Jy km s^{-1}. So for the S_{int}

data, the two effects appear to be evenly matched.

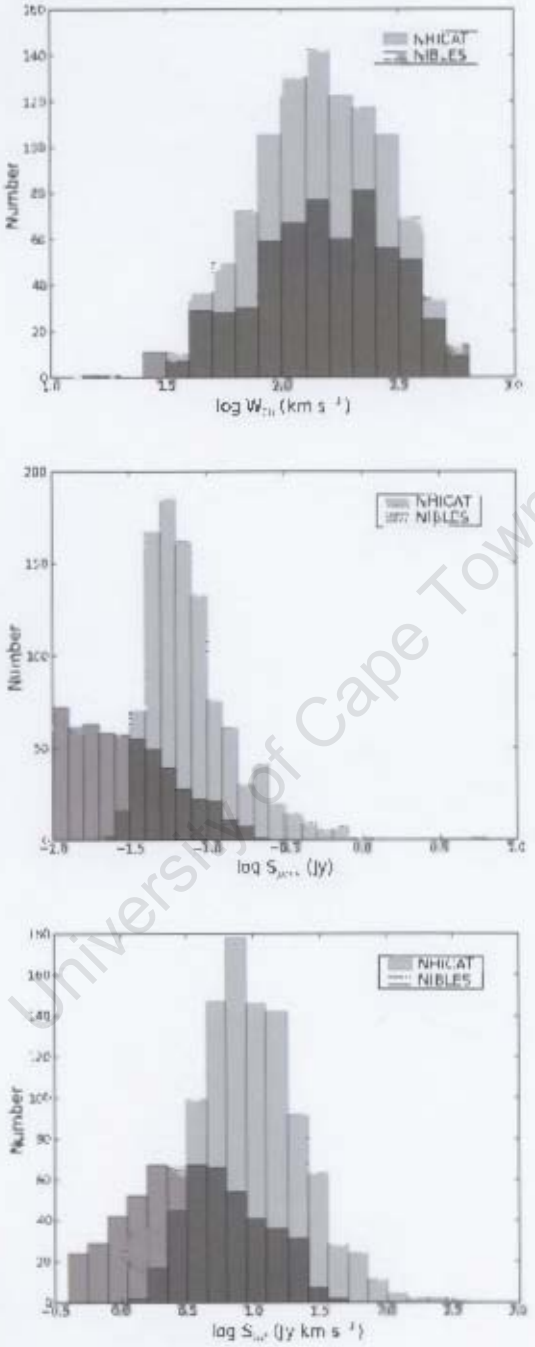

Figure 3.8: Histograms of W_{50}, S_{peak} and S_{int} for this sample of galaxies (dark shading, top to bottom) and for the NHICAT galaxies (light shading, top to bottom).

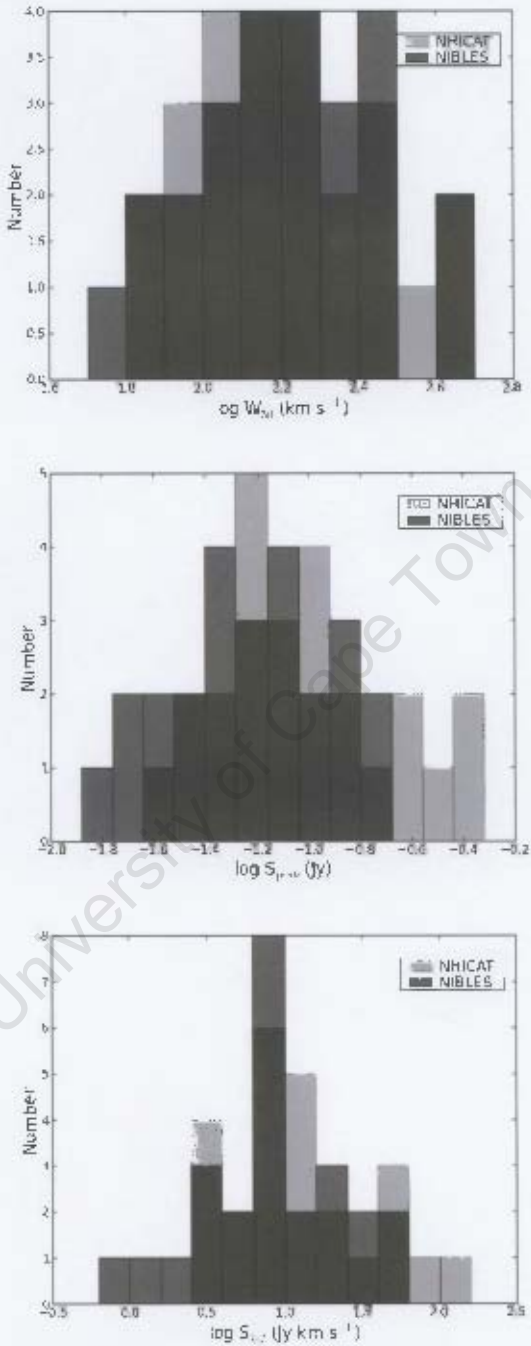

Figure 3.9: Histograms of W_{50}, S_{peak} and S_{int} (top, middle and bottom panels respectively) for the 25 galaxies found in both the NIBLES (dark shading) and NHICAT (light shading) surveys.

Chapter 4

Optical data quality control investigation

Before starting a comprehensive analysis of the data, it is necessary to first peruse the global properties of the galaxies, such as the H I mass-to-light ratios. This preliminary analysis helps to identify any areas of concern or potential pitfalls in the data.

4.1 Introduction

During the course of the preliminary data analysis, a sharp increase of the H I mass-to-light ratios (M_{HI}/L) for faint galaxies in the magnitude range $-14^{\rm m} \lesssim M_g \lesssim -7^{\rm m}$ was noticed. This is illustrated in Fig. 4.1 which shows a plot of M_{HI}/L_g (in solar units) for the galaxy sample against g band absolute magnitude. The bright galaxies (black crosses) in the range $-22^{\rm m} \lesssim M_g \lesssim -14^{\rm m}$ have $0.01 \lesssim M_{HI}/L \lesssim 1$. Roberts & Haynes (1994) performed an extensive study of galactic physical parameters and found that M_{HI}/L increases for later-type galaxies. The median range for early types (E to Sb) was $0.03\,{\rm M}_\odot/{\rm L}_\odot < M_{HI}/L_B < 0.21\,{\rm M}_\odot/{\rm L}_\odot$. For later types (Sbc to S/Im) the median range is higher, $0.29 < M_{HI}/L_B < 0.78$. The values of M_{HI}/L

for the brighter galaxies in our sample can therefore be considered to fall within a normal range.

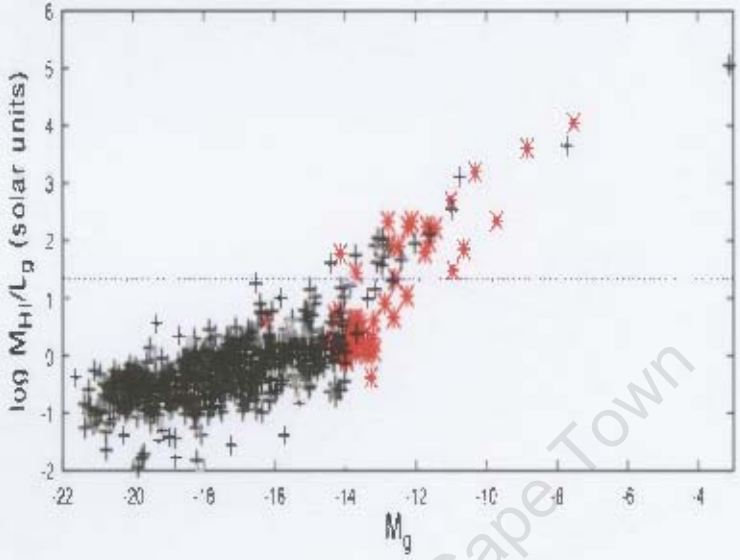

Figure 4.1: The g band HI mass-to-light ratio for the entire sample of galaxies. The horizontal axis is the g band absolute magnitude; the vertical axis is in solar units. The red asterisks represent faint galaxies in the magnitude range -14$^m \lesssim M_g \lesssim$ -7^m the black crosses represent the high surface brightness galaxies. The blue line represents the highest value, $M_{HI}/L_B \leq 22\,M_\odot/L_\odot$, found by Warren et al. (2006).

Many of the faint galaxies in Fig. 4.1 have extremely high M_{HI}/L_g, shown by the steep upward trend for optically fainter systems with $M_g \gtrsim -14^m$. A simple interpretation of Fig. 4.1 would imply that there exist optically faint galaxies with $M_{HI}/L_g > 1000$. The highest values of M_{HI}/L_H found previously are from a sample of 9 extremely gas rich late-type galaxies chosen from the HIPASS Bright Galaxy Catalogue (Koribalski et al., 2004). Values in that sample are in the range $1.1\,M_\odot/L_\odot \leq M_{HI}/L_B \leq 22\,M_\odot/L_\odot$ (Warren et al., 2006). The maximum value, $M_{HI}/L_B = 22\,M_\odot/L_\odot$, is represented in Fig. 4.1 by the blue dashed line. It is the only value in that sample greater

than $5\,M_\odot/L_\odot$. A study by van Zee (2001) calculated M_{HI}/L_B for a sample of over 50 late-type galaxies with magnitudes $M > -18^m$. The range of M_{HI}/L_B was $0.1\,M_\odot/L_\odot \leq M_{HI}/L_B \leq 6.9\,M_\odot/L_\odot$. In that sample, only two of the galaxies had $M_{HI}/L_B > 5\,M_\odot/L_\odot$. Furthermore, the blind H I survey carried out by Spitzak & Schneider (1998) found 34 galaxies (out of a sample of 75 sources) with $1\,M_\odot/L_\odot \lesssim M_{HI}/L_B \lesssim 10\,M_\odot/L_\odot$; only five sources had $M_{HI}/L_B > 5\,M_\odot/L_\odot$. For ease of comparison, these results are summarised in Table 4.1. The first column gives the publication in which the data was resented, the second column lists the sample size, the third column gives the range of M_{HI}/L_B and the fourth column details the number of sources in the sample with $M_{HI}/L_B > 5\,M_\odot/L_\odot$.

Table 4.1: Comparison of high M_{HI}/L_B results

Reference	sample size	M_{HI}/L_B $[M_\odot/L_\odot]$	Number of source with $M_{HI}/L_B > 5\,M_\odot/L_\odot$
This sample	806	$0.01 - 10^5$	59
Warren et al. (2006)	9	$1.1 - 22$	1
van Zee (2001)	55	$0.1 - 6.9$	2
Spitzak & Schneider (1998)	75	$0.1 - 10$	5

The findings of these studies suggest that systems with $M_{HI}/L_B > 5\,M_\odot/L_\odot$ are rare. This would make the extremely high values of M_{HI}/L_g seen in Fig. 4.1 rather exceptional. In the rest of this chapter, I investigate various biases, selection effects and parameter estimates to ascertain the cause of these large mass-to-light ratios.

4.1.1 A Malmquist-type selection effect

One possible cause for the steep upward trend could be a Malmquist-type bias in the data. The Malmquist bias (Eddington, 1913; Malmquist, 1936)

is a selection effect whereby objects with fainter absolute magnitudes are under-represented at larger distances in samples of galaxies. This results in a dataset that is skewed towards brighter sources as distance increases.

The NIBLES sample was chosen based on absolute magnitude and roughly equal numbers of galaxies across the magnitude range. The bias due to an apparent magnitude cut off should not be present in the data.

The galaxy Luminosity Function (LF) is optical analogue of the H I MF; i.e. the LF relates the number density of galaxies to the optical lumniosity. As with the H I MF, the LF can also be described by a Schechter function (Schechter, 1976):

$$\varphi(L)dL = \varphi^*(\frac{L}{L^*})^\alpha \exp(-\frac{L}{L^*})d(L/L^*), \tag{4.1}$$

where the $\varphi(L)$ is the space density of the galaxies, φ^* is the normalisation constant, L^* is the H I luminosity at which the LF shows a sharp change in slope and α is the slope of the LF when $L \ll L^*$.

The LF indicates that the number of galaxies rises steeply for fainter, later-type systems as shown in Fig. 4.2 (see also Heyl et al., 1997; Marzke et al., 1994). The top left panel shows the LF for all the galaxies in the sample. The "Type" label in the upper left corner of the remaining panels indicate the morphologaical type of the galaxies, where Type 1 is the earliest type and Type 5 is the latest. It is clear from this image that the number density of galaxies increases for later types. This increase in numbers will lead to increased scatter in the luminosity data; more outliers from the mean luminosity will be seen.

The NIBLES H I sensitivity is rms = 3.22 mJy. Only systems with sufficient H I flux will enter into the sample as a detection. The sensitivity cut-off introduces a Malmquist-type selection effect within the H I data; systems

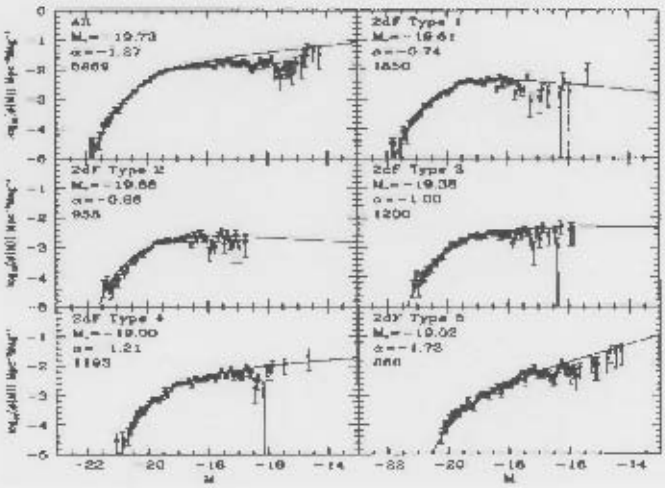

Figure 4.2: An example of the Luminosity Function for various galaxy morphological types. The top left panel shows the LF for all the galaxies in the sample. The "Type" label in the upper left corner of the remaining panels indicate the morphologaical type of the galaxies, where Type 1 is the earliest type and Type 5 is the latest. *Image:* Folkes et al. (1999)

with low flux values will not be observed if they are too far away. This leads to an increase in the M_{HI}/L with increasing optical faintness because the H I flux detection threshold is constant across the optical luminosity range, but the luminosity decreases. We then expect to see an increase in M_{HI}/L as luminosity decreases. The increase in M_{HI}/L_g shown in Fig. 4.1 could then be due to this effect.

For the five faintest galaxies shown in Fig. 4.1, $M_{HI}/L_g > 227\,\mathrm{M}_\odot/\mathrm{L}_\odot$. In particular, SDSS085424+343322 has $M_{HI}/L_g = 11\,580\,\mathrm{M}_\odot/\mathrm{L}_\odot$ which translates to a luminosity and H I mass of $L_g = 3.9\times10^5$ and $M_{HI} = 1.3\times10^9\,\mathrm{M}_\odot$. This galaxy has an H I flux of 92.5 mJy. A system with this flux would almost certainly have been observed by previous H I surveys such as HIPASS, which has a sensitivity of 13 mJy beam^{-1} (Meyer et al., 2004). However, no objects with such extreme values of M_{HI}/L_g have been detected previously.

The trend of steeply increasing M_{HI}/L_g can therefore not be explained by a Malmquist-type selection effect.

4.1.2 Confusion sources

The SDSS uses an automated system to identify and analyse objects. This system sometimes incorrectly identifies objects as galaxies when they are not. These objects are called optical confusion sources. An optical confusion source is one that is identified by the SDSS photometry software as a galaxy and listed in the database as such, but is actually a substructure within a galaxy, such as an optically bright star-forming region.

These misidentified objects may lead to a bright galaxy being classified as a faint one. For example, Fig. 4.3 shows SDSS 012206.4+005616.6 (left panel of Fig. 4.3, circled) and SDSS 012213.9+005731.4 (middle panel of Fig. 4.3, circled). The image in the right panel is centered on NGC 0493. It is clear that SDSS 012206.4+005616.6 is actually a compact, optically bright region at the south east end of the parent galaxy, while SDSS 012213.9+005731.4 is a star-forming region at the other end of the parent galaxy. These sources are listed as separate galaxies in the SDSS database with apparent B band magnitudes of 20.7^{m} and 19.4^{m} respectively. These sources are actually bright regions within NGC 0493, a galaxy with an apparent B band magnitude of $m_B = 12.9^{\mathrm{m}}$.

The large M_{HI}/L_g values could be caused by confusion sources in the sample. The misidentified source would be a substructure of the parent galaxy, leading to an incorrect and clearly underestimated magnitude value. The H I mass for the source would be one associated with the entire parent galaxy, since the beam size of NRT is usually large enough that the galaxy remains unresolved in H I. Thus, when the ratio of these two parameters is calculated, it yields a value that is unrealistically high.

For instance, SDSS 142837.8+003311 (henceforth source 2275) is such a confusion source. It is actually part of the galaxy PGC 051719. Source 2275 has an absolute g band magnitude $M_g = -11.57^{\mathrm{m}}$ and $M_{HI} = 2.75{\times}10^8\,\mathrm{M}_\odot$. This results in an incorrectly derived $M_{HI}/L_g = 41.6\,\mathrm{M}_\odot/\mathrm{L}_\odot$. The parent galaxy, PGC 051719, has an absolute g band magnitude of $M_{g,parent} = -17.31^{\mathrm{m}}$, the H I mass is equal to that of source 2275. The parent galaxy has $M_{HI}/L_{g,parent} = 0.21\,\mathrm{M}_\odot/\mathrm{L}_\odot$.

In order to excise the confusion sources from the sample, the SDSS colour image of each galaxy was examined to identify and eliminate obvious confusion sources in the sample. Each galaxy was then also cross-checked with the NASA Extragalactic Database (NED)[1] to search for further confusion sources. These objects were noted and eliminated from the sample.

[1] http://nedftp.ipac.caltech.edu/

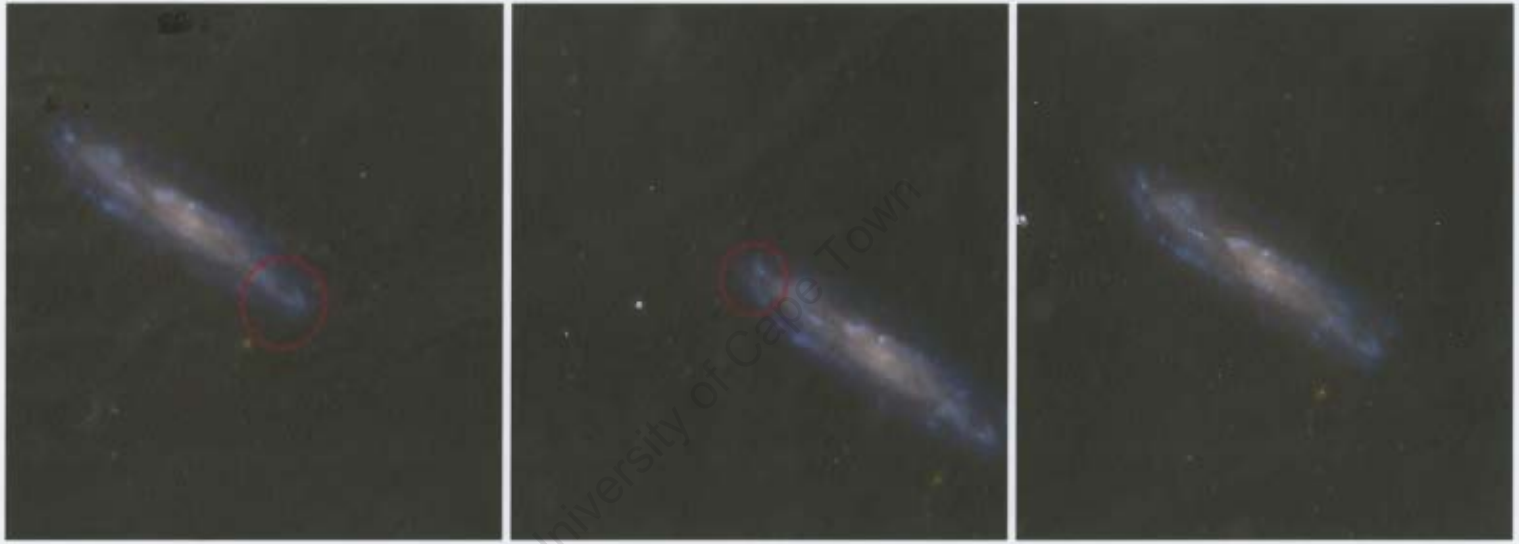

Figure 4.3: Colour images (5′×5′) of SDSS 012206.4+005616.6, circled (left panel) and SDSS 012213.9+005731.4, circled (middle panel) are clearly not galaxies, but rather they are part of NGC 0493 (right).

To eliminate confusion sources, the galaxies with the highest M_{HI}/L_g values were investigated; 75 sources with absolute g band magnitudes $-16^m \lesssim M_g \lesssim -7^m$. Twenty six of these galaxies were found to be confusion sources (over 200 confusion sources were found throughout the sample). Fig. 4.4 shows re-plotted M_{HI}/L_g in solar units against the absolute g band magnitude for these 75 sources. The red crosses are non-confused sources; the blue circles are confused sources. Sixteen sources (33% of the remaining galaxies) with $M_{HI}/L_g > 30 M_\odot/L_\odot$ are still present. Confusion sources alone can therefore not account for the high H I mass-to-light ratios.

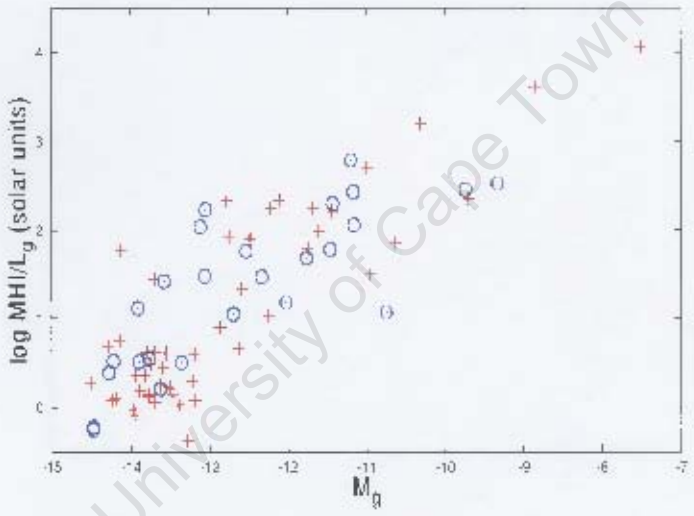

Figure 4.4: The plot of M_{HI}/L_g vs. M_g for the 75 faint galaxies with the highest values of M_{HI}/L_g. The red crosses are sources with no confusion; the blue circles are confused sources.

4.1.3 Inclination effects

The SDSS uses circular Petrosian apertures (see §2.1.2) to carry out photometry. It was thought that these apertures may lead to a less accurate

fit to the shape of the galaxies depending on inclination than an elliptical aperture. This could lead to incorrect magnitude determination. This is especially true for highly inclined systems as they would deviate significantly from a circular shape. If circular apertures were to yield an underestimate of the magnitudes and subsequently a low luminosity value, it could explain the large values of M_{HI}/L_g seen in Fig. 4.1. Strauss et al. (2002) state that the use of circular apertures does not influence the photometry for inclined systems, but it was felt that the inclination should be investigated to verify this statement.

To examine whether the inclination of the galaxies contributed to the high M_{HI}/L_g values, the galaxies were divided into a high inclination group and a low inclination group. The inclinations were determined using the isophotal diameters of the galaxies. There were also galaxies for which no inclination data were determined because the SDSS isophotal diameters were not reliable.

Figure 4.5 shows the faint galaxies with different symbols distinguishing the different inclination groups. The blue crosses represent galaxies with inclination $i > 50°$, the red circles are galaxies with $i < 50°$and the black asterisks are galaxies for which no reliable isophotal diameters are available. The majority of the highly inclined systems have $0.32\,\mathrm{M}_\odot/\mathrm{L}_\odot < M_{HI}/L_g < 6.3\,\mathrm{M}_\odot/\mathrm{L}_\odot$, a normal range. The systems with low inclination tend to be fainter and have higher values of M_{HI}/L_g. The galaxies with no inclination data have the highest value of M_{HI}/L_g. There appears to be a bias against low inclination or no inclination galaxies in the magnitude range $M_g > -13^{\mathrm{m}}$.

A deeper investigation of the photometry was required to rectify the spurious data M_{HI}/L and to resolve the apparent bias due to inclination. Individual photometry on galaxies over the entire magnitude range was needed. These results could then be compared to the magnitudes generated by the

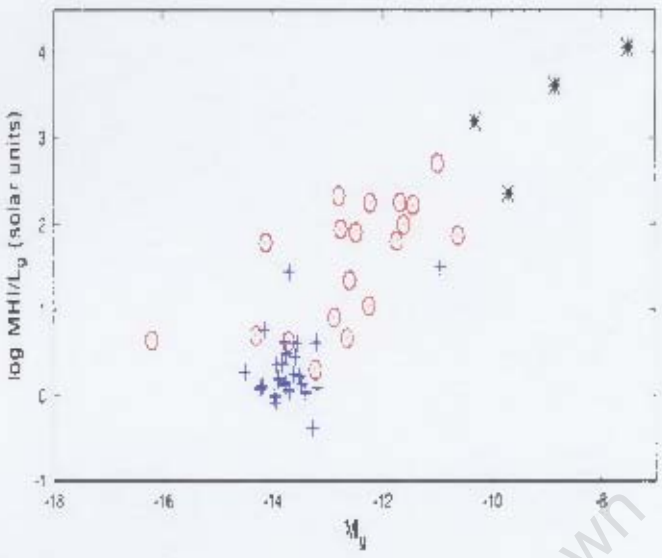

Figure 4.5: M_{HI}/L_g vs M_g. The blue crosses are galaxies with inclination $i > 50°$, the red circles are galaxies with inclination $i < 50°$ and the black asterisks are galaxies for which no inclination data is available.

SDSS algorithm. This investigation and its results are discussed in the next section.

4.2 Re-analysis of the photometric data of faint SDSS galaxies

A sub-sample of 403 galaxies was chosen from the sample for photometry re-analysis. All the galaxies in the NIBLES sample we assigned to M_z magnitude bins that are 0.5^m wide. If there were less than 20 galaxies in a bin, then the entire bin was included in the sub-sample. Therefore, all galaxies with $-24^m \leq M_z \leq -23.5$ and $-13^m \leq M_z \leq -10$ were included in the sub-sample. Galaxies with $-23.5^m \leq M_z \leq -13^m$ were chosen randomly. The g band photometry for the sub-sample, as well as the i band photometry

for the faintest galaxies ($-14^{\mathrm{m}} \leq M_z \leq -10^{\mathrm{m}}$), were re-calculated. The re-analysis was done in two filters to check whether the results were consistent in both filters. This is to ensure that any results obtained applied to the entire bandpass range. The photometry was re-evaluated using the Source Extractor (SE) programme (Bertin & Arnouts, 1996).

SE is a programme that carries out automated detection and photometry on sources in FITS files. It works by first calculating and subtracting the background radiation from the FITS image. It then detects objects that are brighter than a specified threshold level and measures their positions and shapes. Photometry is carried out on these objects. The programme writes the data (apparent magnitude, position, axes ratio, etc.) for each object to a catalogue file and creates a "check" image of the FITS file. This "check" image is used to verify that the correct source has been analysed. The FITS image files for each galaxy were obtained from the SDSS Data Archive Server [2]. For this work, SE used the Petrosian system to determine the magnitudes of the galaxies. The data obtained from SDSS were compared to the SE photometric data in order to verify its accuracy.

4.2.1 The g band data comparison

The SDSS and SE apparent magnitudes for the sub-sample are compared in Fig. 4.6. The red crosses represent the SDSS data with magnitude errors $\epsilon_{mg} < 1^{\mathrm{m}}$, the green circles indicate SDSS data for which $\epsilon_{mg} > 1^{\mathrm{m}}$. The blue line is the line of equality. A large fraction of the data (82%) falls within 0.5^{m} of the line of equality, but there are data that deviate significantly from the line. The plot shows that difference in magnitude increases for fainter apparent magnitudes and that $\mathrm{m}_{g,SDSS}$ is underestimated. However, not all faint apparent magnitudes are affected.

[2] http://das.sdss.org/DR5-cgi-bin/DAS

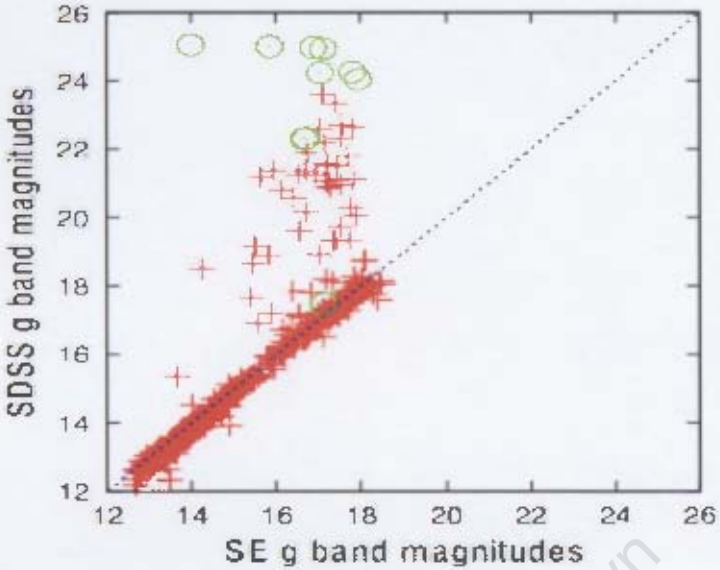

Figure 4.6: The g band apparent magnitudes for all galaxies in the sub-sample. The red crosses represent the data for which the magnitude error $\epsilon_{mg} < 1^{\mathrm{m}}$, the green circles indicate data with $\epsilon_{mg} > 1^{\mathrm{m}}$. The blue line is the line of equality.

It is clear that faintness of sources is not the only factor that leads to underestimated magnitudes. Further inspection of the data revealed that many of the outliers have very small Petrosian radii as given by the SDSS. Therefore, the difference in SE and SDSS magnitudes, Δm_g, as a function of the SDSS Petrosian radius, R_P in arcseconds, is plotted in Fig. 4.7. This plot makes it clear that the SDSS photometry for objects with $R_P < 8''$ is mostly wrong and heavily underestimated.

Figure 4.8 shows examples of two galaxies with $R_P < 8''$ and large Δm. Each image is a $2''$ by $2''$ colour SDSS image. The green superimposed circle indicates the SDSS g band Petrosian aperture for each galaxy. The image on the left is that of SDSS112338.8+535031.7. For this source $R_P = 2.97''$ and $\Delta m_g = -11.08^{\mathrm{m}}$. The right panel is an image of SDSS085424.02+343321.7. This galaxy has $R_P = 2.97''$ and $\Delta m_g = -9.16^{\mathrm{m}}$. It is clear that both these

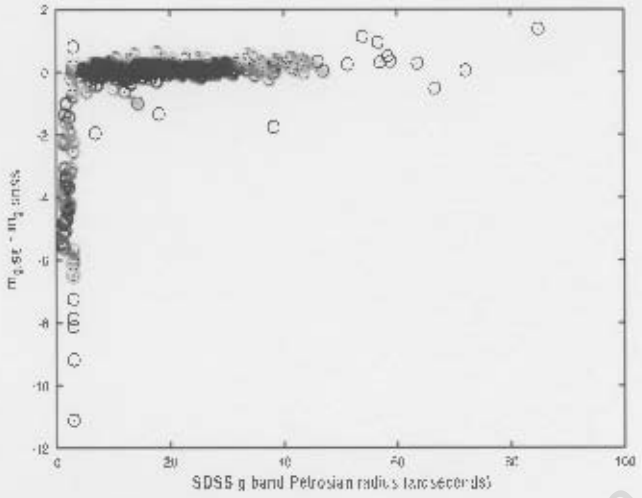

Figure 4.7: The difference between $m_{g,SE}$ and $m_{g,SDSS}$ as a function of Petrosian radius R_P.

Petrosian apertures grossly underestimate the size of the galaxies and can therefore not yield accurate flux measurements.

4.2.2 The i band data comparison

The photometry re-analysis was also carried out in the i band to verify whether the problem with the photometry existed not only in the g band, but in other filters as well. If the magnitude underestimation is caused by small $R_P < 8''$, then this trend should be present in the i band as well as in the g band. The i band analysis was restricted to the faint galaxies with $-10^{\mathrm{m}} \geq M_i \geq -14^{\mathrm{m}}$. SE was used to determine the apparent magnitudes for these sources. As with the g band data, a comparison was done between the SDSS data and the SE data.

Figure 4.9 shows this comparison for the faint galaxies. The green circles are the SDSS data points with magnitude errors $\epsilon_{mi} > 1^{\mathrm{m}}$, the red crosses are

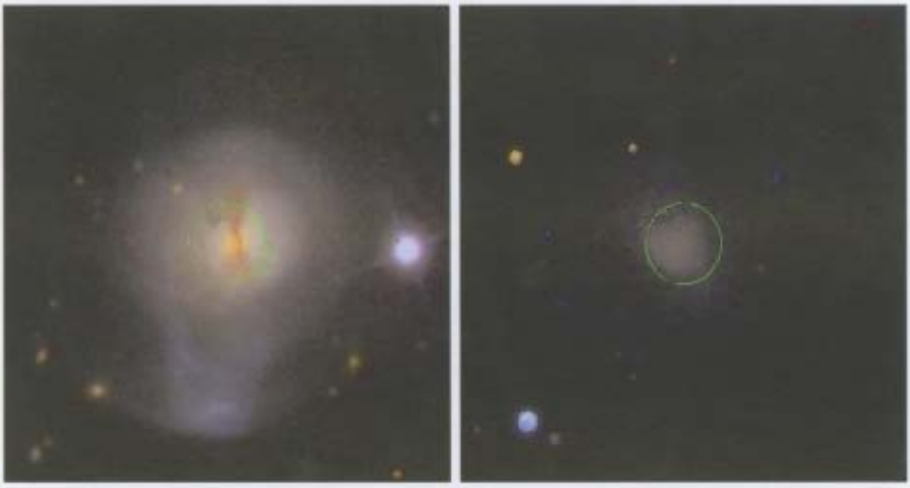

Figure 4.8: SDSS112338.8−535031.7 (left panel) and SDSS085424.02+343321.7 (right panel) with Petrosian apertures superimposed (green circles).

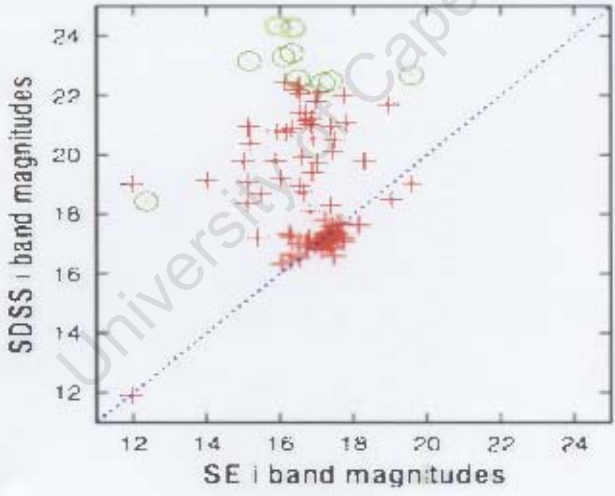

Figure 4.9: The i band comparison for galaxies with $-10^{\mathrm{m}} \geq M_z \geq -14^{\mathrm{m}}$. The red crosses represent data points with $\epsilon_{mi} < 1^{\mathrm{m}}$, the green circles indicate data with $\epsilon_{mi} > 1^{\mathrm{m}}$ and the blue line is the line of equality.

data with $\epsilon_{mi} < 1^{\mathrm{m}}$ and the blue line is the line of equality. The magnitudes have large differences; the result is similar to what is seen in Fig. 4.6 for the

g band magnitudes.

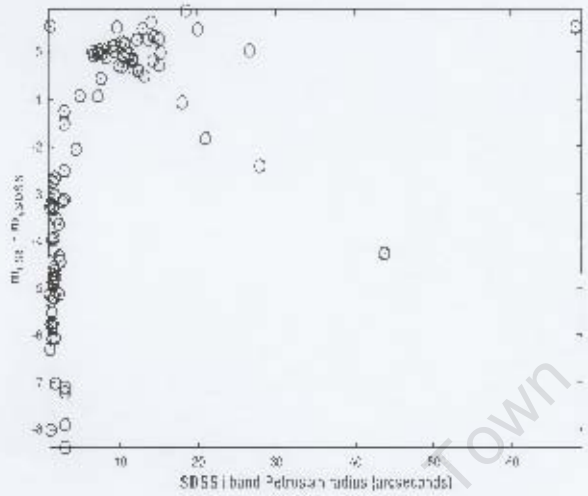

Figure 4.10: The difference between SE and SDSS i band magnitudes as a function of R_p.

Figure 4.10 shows Δm_i as a function of R_P in arcseconds. This plot shows that the SDSS photometry for the i band differs very much from the results given by SE when $R_P < 8''$. This confirms the trend seen for the g band, i.e. the large deviations in magnitudes occur for most galaxies which have $R_P < 8''$. However, there are also large differences between SE and SDSS i band magnitudes for some sources with $R_P > 15''$ which is not seen in the g band.

4.3 The clean data

The analysis in both the g and i bands strongly indicates that the SDSS photometry data is underestimating the magnitudes for mostly faint sources with SDSS Petrosian radii $< 8''$. To substantiate this claim, the magnitude comparisons, as well as M_{HI}/L_g vs. M_g were re-plotted for sources with

$R_P > 8''$ only. Fig. 4.11 shows the magnitude comparisons for these galaxies. Figure 4.6 is reproduced in the left panel for comparison. The right panel is the SDSS vs. SE g band apparent magnitudes without sources that have $R_P < 8''$. The blue line is the line of equality. The black dotted lines on either side denote the 2σ interval. By excising the small galaxies, the SDSS and SE data are in much better agreement. Only 14% of the data points are not within 1σ of the line of equality, where $\sigma = 0.30^{\mathrm{m}}$.

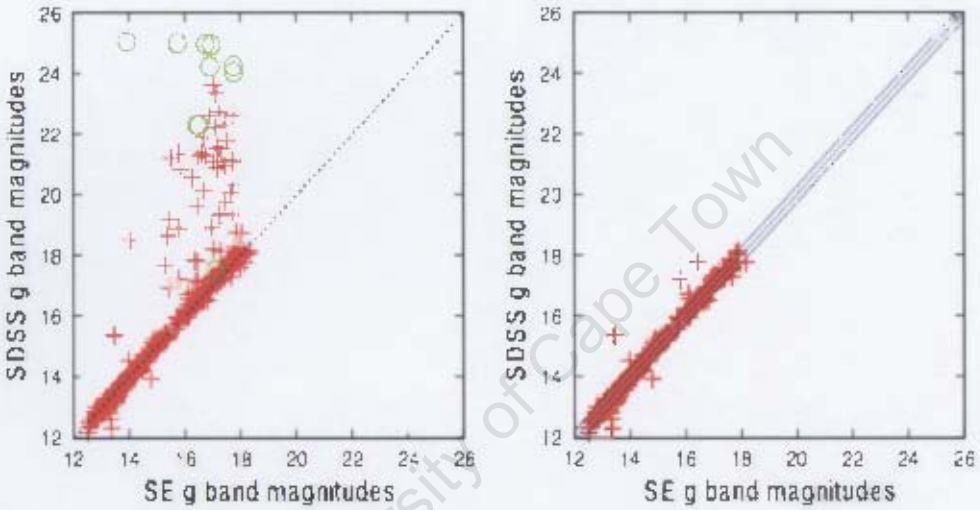

Figure 4.11: The g band apparent magnitude comaprisons. The left panel includes all the galaxies in the sub-sample (as in Fig. 4.6). The right panel is the magnitude comparison in which galaxies with $R_P < 8''$ have been excised. The blue line in both plots is the line of equality; the black dotted lines denote the 2σ interval.

Figure 4.12 shows the i band magnitude comparisons. The left panel is the same as Fig. 4.9, shown here for comparison; the right panel is the plot of $m_{i,SDSS}$ vs $m_{i,SE}$ for objects larger than $8''$. Again, excising the sources with $R_P < 8''$ gives a better fit to the line of equality. The blue line is the line of equality; the black dotted lines on either side indicate the 2σ interval. When the small sources are removed, only 11% of the remaining data lie outside

the 2σ interval, where $\sigma = 0.57^{\mathrm{m}}$.

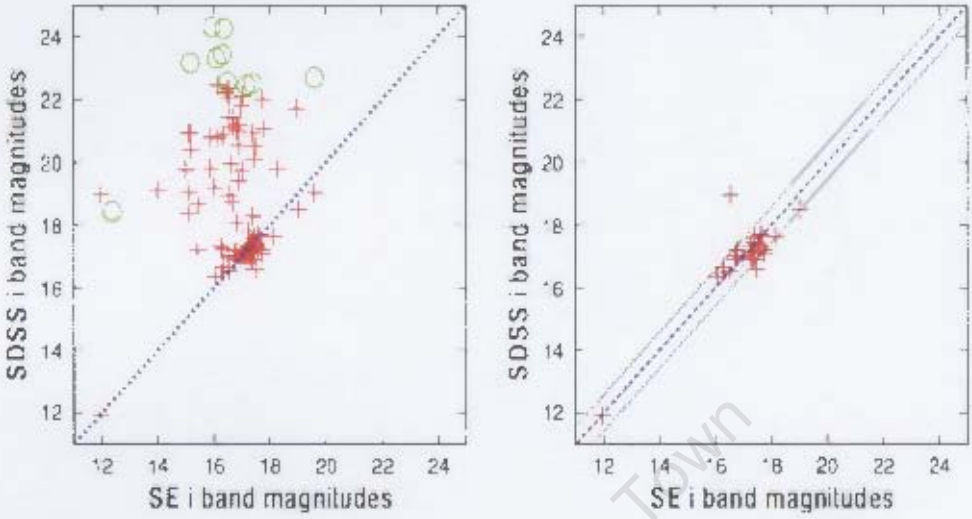

Figure 4.12: Same as Fig. 4.11, but for the i band. The plot of $m_{i,SDSS}$ vs $m_{i,SE}$ for all faint galaxies (left panel) and sources with $R_P > 8''$ (right panel). The blue line in both plots is the line of equality. The dotted black lines denote the 2σ interval.

Figure 4.13 shows the number of galaxies over the entire M_z range for: all observed galaxies within the sample (yellow bars), detected galaxies (red bars) and galaxies with g band $R_g < 8''$ (dark blue bars). Since only about a third of the galaxies in the luminosity range $-24^{\mathrm{m}} \leq M_z < -14^{\mathrm{m}}$ were used in this re-analysis, the number of galaxies with $R_g < 8''$ for this range had to be estimated. This estimation was done by multiplying the number of sources with $R_g < 8''$ per bin by the reciprocal of the fraction of sources that were re-analysed in that bin. So if a quarter of the sources in a bin were re-analysed, then the estimated number of sources with $R_g < 8''$ is 4 times the number of sources with $R_g < 8''$ found in that bin. This estimated number of galaxies is represented by the light blue bars in the histogram. Note that the confusion sources are not included in this histogram. Forty percent of the sources with g band $R_P < 8''$ are galaxies in the magnitude

range $-10^{\mathrm{m}} \leq M_z \leq -14^{\mathrm{m}}$. The number of sources per subsample plotted in Fig. 4.13 is also summarised in Table 4.2. The first column gives the name of the sub-sample in the histogram and the second column lists the number of galaxies.

Table 4.2: Summary of data displayed Fig. 4.13

Sub-sample	Number of galaxies
Observed galaxies in sample	1385
Detected galaxies	600
Estimated number of galaxies with $R_P < 8''$	203
Galaxies with $R_P < 8''$	98

The sources with $R_p < 8''$ and $M_z \geq -14^{\mathrm{m}}$ tend to have irregular shapes or tenuous borders (as seen in Fig. 4.8). It is difficult to fit accurate Petrosian apertures to these types of galaxies. The fitting of incorrect apertures will therefore lead to erroneous magnitude estimates. In order to retain as many faint galaxies in the sample as possible, the SDSS photometric data should be replaced with SE photometric data for all sources that have a Petrosian radius $R_P < 8''$.

As seen in Fig. 4.13, not only faint galaxies have small Petrosian radii. There are many galaxies with $M_z \leq -14^{\mathrm{m}}$ that also have $R_p < 8''$. In the sample the average distance, D, for galaxies with $M_z \leq -17^{\mathrm{m}}$ is $D = 59\,\mathrm{Mpc}$. The sources that have small R_P and magnitudes $M_z \leq -17^{\mathrm{m}}$ are at $D > 72\,\mathrm{Mpc}$. This increased distance means that even though these galaxies are intrinsically bright, they will have small angular sizes on the sky. Thus their Petrosian apertures are small and this could lead to an underestimation of their apparent magnitudes. The galaxies that have $-17^{\mathrm{m}} < M_z < -14^{\mathrm{m}}$ have small Petrosian radii because they are both optically faint and further

away than the faintest galaxies in the sample.

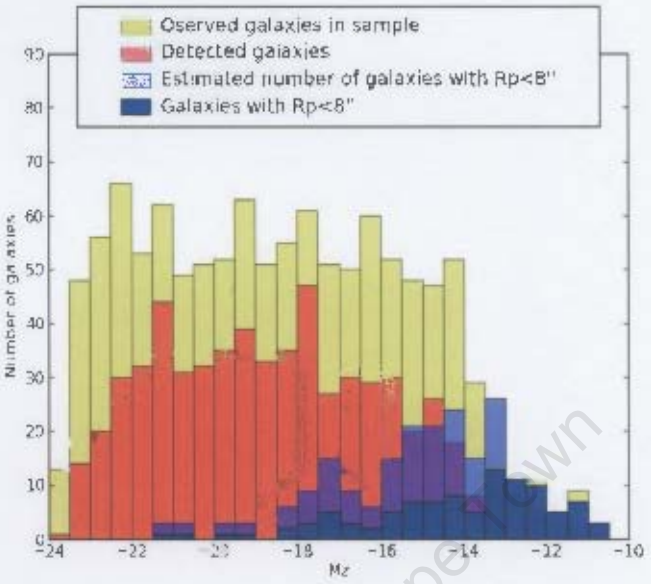

Figure 4.13: Histogram of all observed galaxies within the sample (yellow bars), detected galaxies (red bars), estimated number of galaxies with $R_P < 8''$ (light blue) and galaxies with $R_P < 8''$ (dark blue bars).

4.3.1 The corrected H I mass-to-light ratios

It has been established that galaxies with $R_P < 8''$ have underestimated SDSS photometry data. By using SE data for sources with $R_P < 8''$, the spurious H I mass-to-light ratio results should be eliminated. To confirm this, the M_{HI}/L values are re-determined using the SE data for the galaxies with $R_P < 8''$.

The g band M_{HI}/L data are shown in Fig. 4.14. The top panel shows M_{HI}/L_g vs. M_g for all sources in the sub-sample; only SDSS photometry is used in this plot. The black crosses represent galaxies with $R_P > 8''$ and the

red asterisks represent galaxies with $R_P < 8''$. The bottom panel shows the revised M_{HI}/L_g plot with SE photometry data used for small sources ($R_P < 8''$); these data are indicated by red asterisks. Black crosses represent sources with $R_P > 8''$; SDSS photometry data has been used for these sources (since the SDSS and SE data are in good agreement for these sources). The range of M_{HI}/L_g for the revised data is $0.01\,\mathrm{M}_\odot/\mathrm{L}_\odot \lesssim M_{HI}/L_g \lesssim 10\,\mathrm{M}_\odot/\mathrm{L}_\odot$. This confirms that the very high values of mass-to-light ratios seen in Fig. 4.1 are due to underestimated SDSS magnitudes.

This finding is also substantiated by the i band data. The M_{HI}/L_i values are shown in Fig. 4.15. The top panel shows M_{HI}/L_i for all the galaxies in the luminosity range $-10^{\mathrm{m}} \leq M_z \leq -14^{\mathrm{m}}$ using only SDSS data. The red asterisks indicate data for sources with $R_P < 8''$; the black crosses indicate data for galaxies with $R_P > 8''$. As with the g band data displayed in the top panel of Fig. 4.14, many of the M_{HI}/L_i values are exceedingly high; 14 sources (38%) have $M_{HI}/L_i > 30\,\mathrm{M}_\odot/\mathrm{L}_\odot$. The bottom panel is M_{HI}/L_i with the SE data used for the small sources ($R_P < 8''$) (red asterisks) and the SDSS data used for the larger sources ($R_P > 8''$) (black crosses). When the SE data are used for the objects with $R_P < 8''$, the ratios are much more realistic, $0.13\,\mathrm{M}_\odot/\mathrm{L}_\odot < M_{HI}/L_i < 18.9\,\mathrm{M}_\odot/\mathrm{L}_\odot$. This range corresponds to the values found by previous studies (e.g. Warren et al., 2006; Roberts & Haynes, 1994).

The corrected inclination data

The data in Fig. 4.5 appear to be biased against brighter galaxies with low inclinations, i. Data from this plot that also fell into the re-analysed sub-sample were replotted in order to investigate this apparent bias. Figure 4.16 shows the plot of M_{HI}/L_g vs. M_g that distinguishes between high ($i > 50°$), low ($i < 50°$), and no inclination. The left panel shows M_{HI}/L_g vs. M_g using just SDSS photometry data. The galaxies with low or no inclination have the highest values of M_{HI}/L_g and all have $R_p < 8''$. Only 45% of the

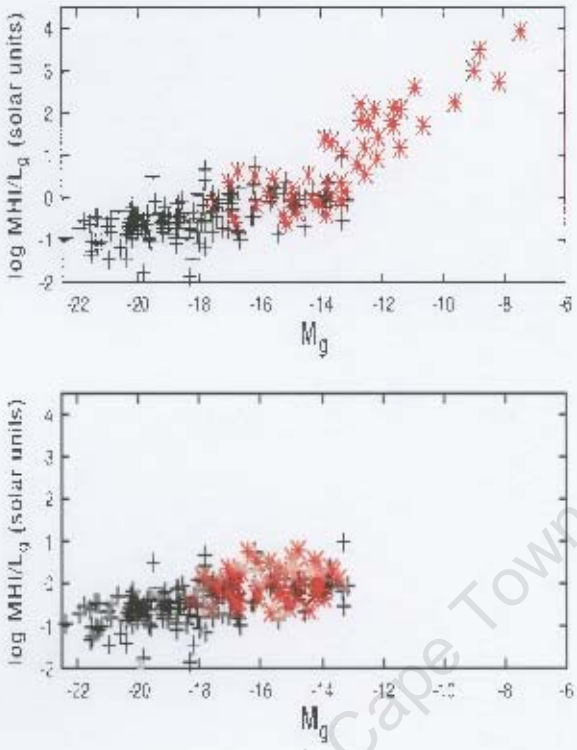

Figure 4.14: The top panel is M_{HI}/L_g vs. M_g for all galaxies in the sub-sample. The red asterisks indicate SDSS data for galaxies with $R_P < 8''$ and the black crosses are the SDSS data for sources with $R_P > 8''$. The bottom panel shows the H I mass-to-light data where SE photometry data has been used for sources with $R_P < 8''$ which are shown as red asterisks. The black crosses in the bottom panel are the SDSS data for sources with $R_P > 8''$.

highly inclined systems have $R_p < 8''$.

The right panel of Fig. 4.16 shows M_{HI}/L_g vs. M_g using SE data. The data for systems with $i > 50^{\circ}$ do not change significantly. The data for the low and no inclination galaxies are significantly changed. These data were in the range $2\,M_{\odot}/L_{\odot} < M_{HI}/L_g < 510\,M_{\odot}/L_{\odot}$ when using the SDSS photometry data. With the SE data, the range changed to $0.2\,M_{\odot}/L_{\odot} < M_{HI}/L_g <$

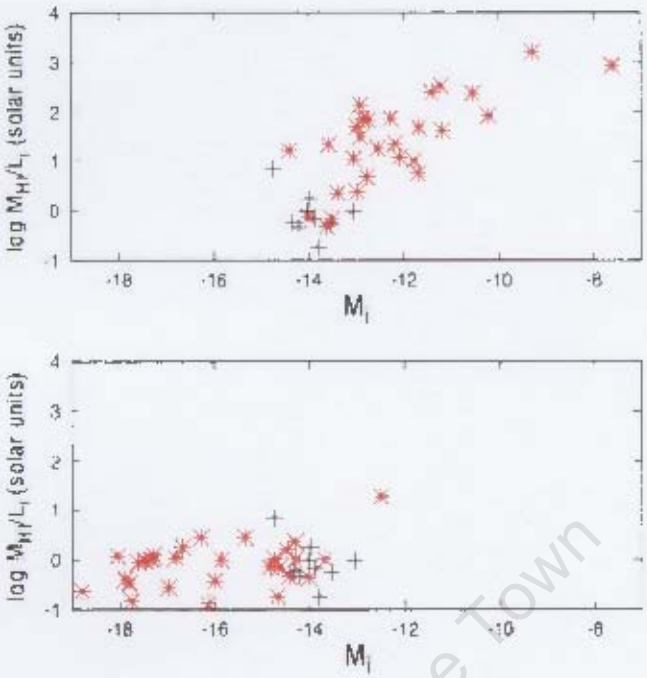

Figure 4.15: The i band H I mass-to-light ratios. The top panel shows M_{HI}/L_i using SDSS data only. The red asterisks represent data for systems with $R_P < 8''$ and the black crosses represent data for galaxies with $R_P > 8''$. The bottom panel shows M_{HI}/L_i when SE data is used for the galaxies with $R_P < 8''$ (red asterisks) and SDSS data is used for larger sources (black crosses).

$3.5\,M_\odot/L_\odot$. There are also no galaxies with $M_g \gtrsim -13$. There is no longer a bias against brighter low inclination systems when the SE photometry data is used for small sources.

The highly inclined systems have a larger average R_P and major axis diameter than the low inclination systems. The smaller galaxies are more difficult to resolve and are more likely to appear round; thus giving the appearance of being less inclined. As discussed in §2.1.2, Strauss et al. (2002) state that inclination does not affect the fitting of Petrosian apertures. However, the findings of this work imply that small, faint galaxies that appear to

have low inclination are more likely to have very small Petrosian radii. Thus these small, low inclination objects are more likely to have underestimated magnitudes.

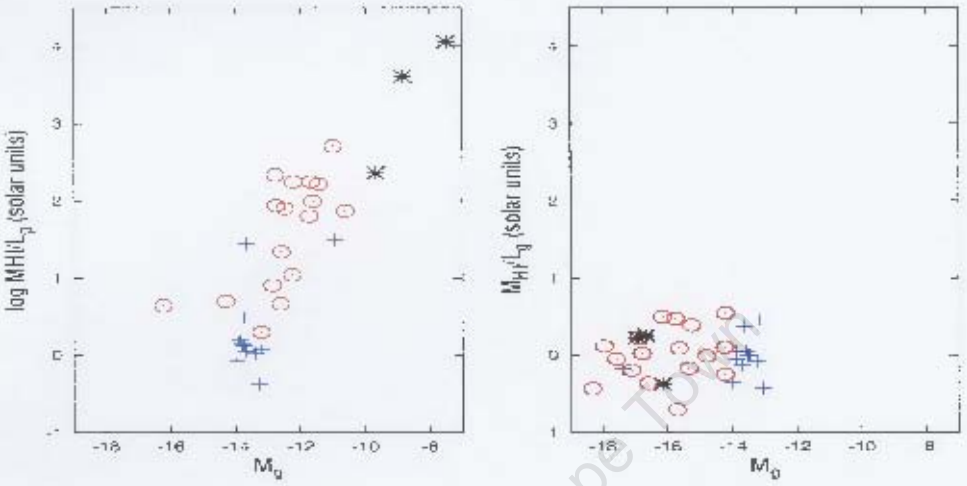

Figure 4.16: M_{HI}/L_g as a function of M_g where high and low inclination systems have been distinguished. The left panel is Fig 4.6; i.e. only SDSS photometry data has been used in this plot. The right panel shows M_{HI}/L_g using only SE photometry data. In both panels the blue crosses indicate galaxies with $i > 50°$, the red circles represent galaxies with $i < 50°$ and the black asterisks indicate that the inclination data for those galaxies could not be determined.

4.3.2 Underestimated photometry data: Implications for other studies

The SDSS photometry data implies the existence of galaxies with $-13 \lesssim M_g \lesssim -3$ and $-13 \lesssim M_i \lesssim -7$. Upon re-analysis of the photometric data, no sources fainter than M_g (or M_i) $\lesssim -13$ are found. This underestimation of apparent magnitude can have serious repercussions for studies that use SDSS photometry.

For instance, the Tully-Fisher relation measures the luminosity of galaxies as a function of their maximum rotational velocity, predicted as $L \propto V^{\alpha}$ or equivalently, $M \propto V^{\beta}$, where M is the absolute magnitude. This relation is also used as a galactic distance indicator. If the photometry data used in this relation are underestimated, then the parameter α will be lower than for higher magnitude values. This incorrect result will in turn lead to underestimation of galactic distances.

A preliminary g band Tully-Fisher (TF) relation was investigated for the sub-sample of galaxies (Fig. 4.17), plotting M_g vs. $\log(W_{50})$. In both plots the large sources ($R_p > 8''$) are represented by black crosses, the small sources ($R_p < 8''$) are represented by red asterisks and the black line is the best fit line. The parameter β was estimated by fitting $log(M) = k + \beta log(W_{50})$ to the data.

The left panel shows the relation using just SDSS photometry data. This plot shows a large amount of scatter caused by outlying data for the small galaxies. For this data $\beta = -6.9 \pm 1.0$. The right panel shows the relation using SDSS data for large sources and SE data for small sources. The scatter is reduced and $\beta = -5.1 \pm 0.8$. A study of the TF relation using SDSS galaxies was carried out by Pizagno et al. (2007). The sample consisted of 234 galaxies with a g band absolute magnitude range of -17$^{\mathrm{m}}$ > M_g > -23$^{\mathrm{m}}$ and inclination, $i > 50°$. Therefore this sample does not include galaxies that potentially have incorrect magnitudes; i.e. no low inclination faint galaxies. The slope for the g band TF relation for their study was found to be $\beta = -5.5 \pm 0.2$. The value of β obtained when using SE photometry for small sources is in better agreement with this result than when SDSS data is used for small sources. This result again demonstrates clearly that SE data should be used for small sources.

The galaxy Luminosity Function (LF) will also be influenced by incorrect

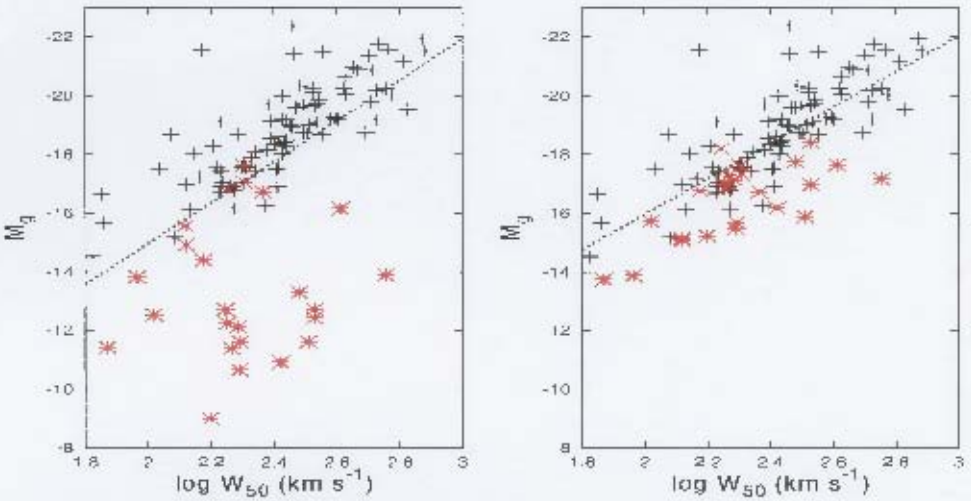

Figure 4.17: The Tully-Fisher relation for this sample of galaxies using only SDSS photometry data (left panel) and using SE data for small sources (right panel). In both plots the black crosses represent galaxies with $R_p > 8''$, the red asterisks represent galaxies with $R_p < 8''$ and the black line is the best fit line

magnitudes. By including the spurious faint galaxy data in the analysis, the LF will predict more faint systems than actually exist in the Universe. This result will in turn influence models of galaxy formation and evolution as these models must then account for an increased number of faint galaxies.

The effect of this overestimation can be seen in the M_g distribution for the sub-sample (Fig. 4.18). The yellow shading indicates that only SDSS photometry data has been used to determine the magnitudes. The blue shading indicates that SE data has been used for the small sources. The SDSS data overestimates the number of galaxies fainter than $M_g = -14^{\mathrm{m}}$. When SE photometry is used, the number objects fainter than $M_g = 13^{\mathrm{m}}$ drops from 19 to zero and the number of galaxies with $-14^{\mathrm{m}} \leq M_g < -13^{\mathrm{m}}$ decreases from 18 to 13. The number of galaxies in the range $-18.5^{\mathrm{m}} \leq M_g < -14^{\mathrm{m}}$ increases from 80 to 105 when SE data is used for small sources. Thus, using SDSS photometry for sources with $R_P < 8''$ will lead to an overestimate of

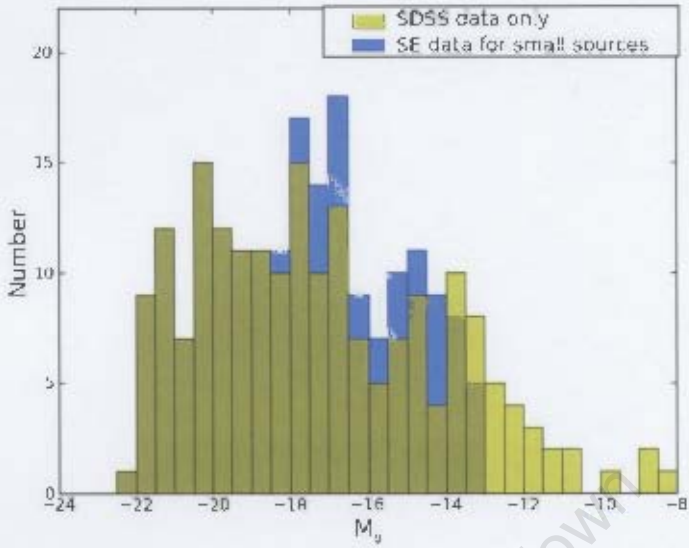

Figure 4.18: The distribution of M_g when only SDSS photometry is used (yellow bars) and when SE data is used for small sources (blue bars).

the number of faint galaxies as well as an underestimate of the number of brighter sources.

It is therefore extremely important to verify the validity of photometric data before attempting any analysis.

Chapter 5

Conclusions and future work

5.1 Conclusions

This dissertation forms part of the pilot survey for the NIBLES H I survey. The dataset used in this work consists of H I spectra and derived H I parameters for the first 1385 (out of a total of 4 000 NIBLES sources) galaxies observed. The dataset also includes photometric and spectroscopic data from the SDSS sixth data release for each galaxy.

The aim of this pilot project is to investigate the quality of the H I and optical data for this sample. An understanding of the data and possible biases and selection effects are being used to optimise the NIBLES survey so that the aforementioned goals can be achieved.

The H I data obtained for the sample are presented in § 3. The full catalogue of H I parameters is presented in Appendix A. The catalogue consists of H I parameters for 600 detections. The parameters listed are the recessional velocity, the rms,the 50% and 20% peak flux velocity widths, the peak and integrated flux and the H I mass.

The H I parameters were compared to data from NHICAT (Wong et al.,

2006). The data for the recessional velocity and velocity widths were found to be in good agreement. However, the flux measurements for a significant fraction of the compared galaxies were found to be underestimated. Each galaxy in NIBLES was observed using only one telescope pointing. The galaxies with H I radii, $R_{HI} \sin(PA) > 2'$ are therefore likely to be extended compared to the E-W diameter of the NRT beam. Eight of the 25 compared galaxies were found to be extended.

Upon examination of the H I mass-to-light ratios of the galaxies, values of $M_{HI}/L_g > 100\,\mathrm{M_\odot L_\odot}$ were seen for galaxies fainter than $M_g \sim -14^\mathrm{m}$ (see Fig. 4.1). Since no previous surveys have ever uncovered systems with $M_{HI}/L_g > 22\,\mathrm{M_\odot L_\odot}$, the data were carefully investigated to determine whether these results were real. The SDSS photometry was re-analysed for 403 galaxies. It was found that the SDSS magnitudes were underestimated for galaxies with Petrosian radii, $R_P < 8''$ and inclination, $i < 50°$ by up to 11^m in the g band and 8^m in the i band. This underestimation was found to affect 13% of the re-analysed galaxies. The new (non-automated) photometry eliminates all the extreme values of M_{HI}/L for the faint sources and yields M_{HI}/L data that are consistent with previous results (Roberts & Haynes, 1994; Spitzak & Schneider, 1998; van Zee, 2001; Warren et al., 2006). The re-analysis also indicates that there are no galaxies fainter than M_g (or M_i) $= 13^\mathrm{m}$ in the sample.

Over 200 optical "confusion" sources were identified and removed from the dataset. Optical confusion sources are objects that are listed in the SDSS database as galaxies but that are actually substructures within galaxies.

This discovery of underestimated photometry data for small, faint systems will have significant effects on the statistical analysis of large sub-samples of the SDSS galaxies; data from the SDSS database cannot just be used without first checking its reliability. For instance, the incorrect data will yield

a luminosity function that over-predicts the number of faint galaxies and under-predicts the number of brighter sources. The Tully-Fisher relation will also be incorrectly derived if these underestimated data are incorporated into the analysis, resulting in incorrect distance estimates. Other studies such as star formation rates and dark matter distribution will be affected as the underestimated magnitudes imply that the galaxies have much less stellar mass than they actually do.

5.2 Recommendations

The data verification presented in § 3 and § 4 have identified ways in which the data can be optimised or corrected so that the science goals of NIBLES can be achieved. The recommendations are as follows:

- The SDSS Petrosian magnitudes for galaxies with $R_P < 8''$ and $i < 50°$ are underestimated. Simply avoiding the galaxies with $R_P < 8''$ will exclude 42 % of the galaxies in the magnitude range $-18.5^{\mathrm{m}} \lesssim M_g \lesssim -13^{\mathrm{m}}$ and create a bias against blue dwarf and irregular galaxies with a median velocity of $\sim 2\,000\,\mathrm{km\,s^{-1}}$. Five percent of galaxies with $M_g < -18.5$ m will be excluded. Instead, the photometry for each of these galaxies should be re-determined in order to ensure that reliable data are used in the analysis. Ideally, the optical data for the entire NIBLES sample should be re-evaluated to ensure the reliability of the data.

- Re-estimating the magnitudes of the galaxies after the sample has been selected does significantly change the magnitude distribution as seen in Fig. 4.18. All objects fainter than SDSS $M_g > 13^{\mathrm{m}}$ are moved to bins in the range $-18^{\mathrm{m}} \lesssim M_g \lesssim -14^{\mathrm{m}}$. The number of galaxies brighter than $M_g < 16.5^{\mathrm{m}}$ are rather higher than in fainter bins, resulting in an uneven magnitude distribution. The overall magnitude range is also

smaller than first thought. In order to select as uniform a magnitude distribution as possible, the magnitude re-estimation should take place before the magnitude selection. Galaxies within the NIBLES velocity range and with optical good spectra should be chosen from the SDSS database. The magnitudes of these galaxies should then be re-determined and the absolute magnitude selection should be carried out using the new magnitude information for each galaxy. Then the magnitude bins can populated correctly since the new optical data will be known to be reliable.

- Optical confusion sources in the sample must be identified and excised. These objects lead to bright galaxies being classified as faint systems. These incorrect data influence H I mass-to-light ratios, the Tully-Fisher relation and leads to an artificially increased number of faint galaxies in the sample. These optical confusion sources mainly affect the fainter galaxies, i.e they are bright objects that have been classified as faint objects. To find such confused sources, it is useful to look at the SDSS colour image of each galaxy. It is often quite obvious whether the source is a real galaxy or just an optically bright region within a galaxy. These false sources can also be identified by looking at galaxy magnitude as a function of recessional velocity. If a faint source is seen to have a high recessional velocity, then it is potentially a confused source.

- The NIBLES team would like to avoid extra detections due to multiple galaxies in the NRT beam. The easiest way to do this would be to only select galaxies without any neighbours within $\alpha \sim 2''$ and $\delta \sim 11''$. However, this will cause the sample to have a bias against groups and clusters of galaxies, where the member galaxies are quite close together.

5.3 Future work

There are several avenues of research that can be pursued almost immediately with the data presented in this dissertation. A full Tully-Fisher analysis in all five passbands can be performed. The Tully-Fisher relation is used as a distance indicator for galaxies. The distances calculated for galaxies in the different passbands can then be compared to verify that the results are self consistent. Given the large dataset, the relation can be determined as a function of morphological type as well as environment. The galaxy distances obtained from the Tully-Fisher relation are a good first estimate of the galaxy redshift and can be used to get a rough approximation of the distribution of galaxies in the Local Universe. These distribution data are needed to compare to cosmological models of galaxy evolution and large scale formation.

The HIMF can be determined for this sample which contains 65 galaxies with $M_{HI} \leq 10^8\,\mathrm{M}_\odot$; the full NIBLES sample could contain as many as 180 such galaxies. The HIMF constructed by Zwaan et al. (2003) contains only 40 galaxies in this mass range. The NIBLES data are therefore well suited to the task of determining an accurate value for the much disputed faint end slope of the HIMF. The H I budget for the Local Universe can then be calculated using the parameters obtained from the HIMF.

Using the H I linewidths, the dynamical mass of the galaxies within the sample can be calculated. A comparison of this dynamical mass to the stellar mass (obtained using the optical data) and the H I mass will allow the study of the dark matter content of the galaxies.

Appendix A

Full H I data catalogue

Six hundred of the observed galaxies were detected with $S/N \geq 3\sigma$, where σ is the rms for that particular observation.

The full catalogue for these 600 galaxies is shown in Table 3.1. The parameters listed are: recessional velocity (V_{HI}) in km s^{-1}, the rms in mJy, the velocity widths at the 50% (W_{50}) and 20% (W_{20}) peak flux level in km s^{-1}, the peak flux (S_{peak}) in mJy, the integrated flux (S_{int}) in Jy km s^{-1}and the H I mass (M_{HI}) in solar masses. Note that an entry of zero in the W_{20} or W_{50} columns indicates that the parameter was not recorded.

Table A.1: The full HI catalogue

Coordinates (J2000) hhmmss degrees	V_{HI} [km s^{-1}]	rms [mJy]	S_{int} [Jy km s^{-1}]	W_{50} [km s^{-1}]	W_{20} [km s^{-1}]	S_{peak} [mJy]	log M_{HI} [$M_\odot$]
00 01 03.6 +14 34 48.6	1679	2.32	32	48	6.96	0.14	7.3
00 02 14.8 +14 29 16.0	5053	2.71	175	201	12.74	1.77	9.4
00 03 15.0 +16 08 44.7	1064	2.18	463	489	26.38	9.98	8.7
00 03 44.3 +16 11 12.7	6265	2.67	232	290	11.21	1.97	9.6
00 06 19.6 +14 19 38.7	5330	2.66	14	77	9.31	0.15	8.3
00 06 29.3 +14 10 56.4	5654	2.53	136	247	10.37	1.11	9.3
00 07 01.6 +14 06 23.6	5320	2.72	205	284	9.79	0.98	9.1
00 08 34.3 -10 56 57.5	8842	2.85	110	135	41.04	4.29	10.2
00 08 48.8 +14 02 01.3	1902	2.56	98	117	24.32	2.05	8.6

Table A.1 continued ...

Coordinates (J2000) hhmmss degrees	V_{HI} [km s^{-1}]	rms [mJy]	W_{50} [km s^{-1}]	W_{20} [km s^{-1}]	S_{peak} [mJy]	S_{int} [Jy km s^{-1}]	log M_{HI} [$M_\odot$]
00 12 14.7 +15 15 26.7	1861	2.31	53	64	7.85	0.43	7.9
00 13 38.6 +15 40 28.0	1952	3.18	129	144	22.26	0.69	8.1
00 13 44.0 +00 22 18.2	3926	2.71	120	176	9.49	0.75	8.8
00 20 09.3 +14 17 28.7	4713	2.15	171	190	11.83	1.4	9.2
00 21 51.2 −09 29 32.1	6130	2.4	299	309	9.6	1.49	9.5
00 27 49.7 −01 11 59.9	3846	2.77	235	249	29.92	4.98	9.6
00 30 07.3 −11 06 49.1	3477	2.65	325	342	21.47	4.68	9.5
00 30 09.0 −09 57 11.8	5059	2.85	206	330	10.55	1.56	9.3
00 30 29.8 −08 46 59.8	5236	2.83	260	293	15.28	2.67	9.6
00 33 22.1 −01 07 16.7	1976	2.55	144	168	103.02	13.15	9.4
00 34 02.8 −09 42 19.2	3706	2.69	449	467	51.38	15.92	10.0
00 34 57.9 −09 20 31.9	6709	2.76	339	420	10.49	2.12	9.7
00 36 28.9 −10 06 22.1	5777	2.52	307	351	13.1	2.65	9.7
00 37 10.6 −09 27 25.1	5172	2.32	147	227	12.3	1.23	9.2
00 39 22.9 −08 49 24.4	5672	2.91	228	277	10.77	1.28	9.3
00 41 33.9 −10 01 17.1	3851	1.6	539	564	9.12	2.08	9.2
00 43 32.4 +14 20 33.2	4387	2.38	205	225	18.56	3.29	9.5
00 43 51.9 +00 48 07.0	5358	2.74	228	259	19.29	3.34	9.7
00 44 23.3 +14 17 15.7	4115	2.46	77	104	10.09	0.54	8.7
00 45 51.9 −09 19 41.5	6007	2.77	166	219	12.74	1.65	9.5
00 46 08.8 −10 24 31.0	3919	2.69	148	178	9.15	0.54	8.6
00 47 46.4 −09 50 06.1	5640	3.04	430	0	10.64	2.11	9.5
00 47 47.5 −09 53 58.3	1344	5.07	132	166	99.37	13.06	9.1
00 51 59.6 +00 29 12.1	1612	2.79	175	192	82.58	11.59	9.2
00 52 52.8 +01 12 50.4	1754	2.53	94	124	9.61	0.7	8.0
00 53 29.9 −08 46 04.0	5517	2.62	167	224	9.43	1.05	9.2
00 56 42.7 −09 54 49.9	5552	2.75	199	225	80.85	15.32	10.4
00 57 56.6 +00 52 08.9	2263	2.95	91	121	13.28	0.94	8.4
01 00 04.1 −11 04 57.3	5323	2.64	142	224	27.46	3.87	9.7
01 00 45.8 −09 11 08.5	4507	2.78	144	298	36.42	5.82	9.8
01 01 19.5 −09 50 42.9	4495	2.41	242	260	7.95	1.25	9.1
01 06 51.0 +00 34 13.7	5137	2.37	30	46	9.48	0.19	8.4
01 07 14.2 +13 57 18.4	11165	3.27	238	259	12.43	1.87	10.1
01 09 07.9 +01 07 15.7	1146	2.52	122	159	12.85	1.08	7.8
01 10 20.8 −09 34 10.3	6961	2.75	232	304	17.33	3.06	9.9
01 12 08.6 +00 24 36.7	5374	2.41	239	311	12.77	2.35	9.5
01 14 20.4 +00 55 01.9	1099	2.58	85	118	23.99	1.76	8.0
01 15 30.4 +00 51 39.5	1747	2.81	169	197	118.58	19.03	9.5
01 17 48.4 −08 36 27.1	4009	3.64	130	150	29.48	3.62	9.5
01 19 14.3 −09 35 46.4	1911	3.27	60	146	12.75	0.71	8.1
01 20 06.8 +00 12 19.6	1726	2.62	123	140	17.82	1.69	8.4
01 22 23.8 +00 52 30.7	7942	3.11	508	535	19.9	7.15	10.4
01 26 46.6 +00 38 46.0	1902	2.26	70	116	27.35	2.05	8.6

Table A.1 continued ...

Coordinates (J2000) hhmmss degrees	V_{HI} [km s^{-1}]	rms [mJy]	W_{50} [km s^{-1}]	W_{20} [km s^{-1}]	S_{peak} [mJy]	S_{int} [Jy km s^{-1}]	log M_{HI} [$M_\odot$]
01 27 13.1 +13 36 08.3	4435	2.48	108	138	25.54	2.68	9.4
01 30 15.4 +14 40 39.1	2427	5.17	118	147	38.26	3.66	9.0
01 31 36.1 +13 19 52.7	2723	1.75	103	125	9.28	0.81	8.5
01 33 17.7 +13 19 55.2	2731	2.67	205	224	22.43	3.79	9.1
01 34 08.0 –01 01 56.2	4574	2.71	383	427	15.45	3.58	9.6
01 35 51.1 –10 00 10.6	5773	2.19	374	401	25.51	8.48	10.2
01 36 00.2 +00 39 48.7	5007	2.77	335	373	16.07	3.35	9.6
01 37 08.1 +00 33 53.5	2890	2.02	116	153	10.5	1.07	8.6
01 37 30.8 –08 53 07.7	1794	2.98	120	133	13.11	1.21	8.3
01 37 37.1 +00 02 24.9	4827	2.02	215	281	8.28	1.37	9.2
01 41 39.7 –09 13 03.9	1813	2.51	57	73	17.07	0.78	8.1
01 44 35.8 –08 15 05.9	3849	1.93	18	115	7.53	0.28	8.3
01 48 36.4 –10 19 34.3	1555	2.42	100	160	10.41	0.94	8.0
01 49 10.4 –10 03 40.4	1976	3.27	180	202	95.16	16.02	9.5
01 49 10.8 –10 25 35.3	1751	2.94	375	399	43.22	12.05	9.3
01 49 54.3 –09 13 41.7	1905	3.14	43	68	11.3	0.33	7.8
01 50 54.4 –10 22 10.4	1804	3.52	88	229	13.02	0.91	8.2
01 59 34.7 +14 00 29.5	4536	2.45	207	233	11.27	1.86	9.3
02 08 58.7 –07 46 00.5	3973	2.71	141	319	32.79	4.41	9.5
02 09 20.8 –10 07 59.1	3753	2.62	200	317	16.24	3.18	9.3
02 17 04.8 +01 14 39.1	6301	2.64	163	250	11.09	1.48	9.5
02 35 32.7 –07 09 15.9	1522	2.79	78	99	156.52	12.5	9.2
02 39 29.1 –08 08 01.1	1209	3.23	203	234	45.22	8.52	8.8
02 40 23.9 –08 26 00.7	1362	3.2	100	121	211.2	20.25	9.3
02 40 32.8 –08 08 51.6	1338	2.7	47	82	50.49	2.65	8.4
02 44 21.1 +00 40 31.4	2752	3.11	112	143	23.95	2.06	8.9
02 46 25.2 +00 29 55.1	1511	3.92	223	249	81.93	20.87	9.4
02 53 46.7 –07 23 44.0	1359	2.78	48	89	11.4	0.48	7.6
02 57 04.4 –07 41 08.3	5115	3.24	300	340	20.41	4.42	9.8
02 59 14.5 +00 33 59.7	2741	3.94	45	0	13.4	0.53	8.3
03 00 40.2 +00 01 13.3	2809	3.32	200	214	27.56	3.89	9.2
03 01 03.3 +00 44 36.5	2627	2.94	108	137	50.57	5.45	9.3
03 03 41.2 –01 04 24.8	4184	3.3	54	0	12.21	1.53	9.1
03 06 46.8 +00 28 10.3	699	3.11	38	79	14.31	0.58	7.1
03 06 52.4 +00 47 40.1	3180	2.68	188	210	49.85	7.92	9.6
03 08 48.3 –07 02 26.2	8459	2.35	415	458	14.34	4.03	10.2
03 09 35.2 –07 57 26.0	3708	2.16	230	278	23.76	4.58	9.5
03 09 39.1 –07 50 46.2	3687	2.93	223	241	29.59	5.34	9.6
03 13 24.2 –08 12 44.6	5035	2.6	398	434	11.18	3.23	9.6
03 13 45.2 +00 14 29.1	7666	3.29	614	838	16.45	5.94	10.3
03 13 47.8 +00 41 39.7	6273	2.97	282	297	12.47	1.56	9.5
03 14 06.7 –07 16 34.3	5123	2.6	214	316	20.8	4.1	9.7
03 17 02.8 –06 12 20.4	2069	2.56	102	146	17.15	1.65	8.5

Table A.1 continued ...

Coordinates (J2000) hhmmss degrees	V_{HI} [km s^{-1}]	rms [mJy]	W_{50} [km s^{-1}]	W_{20} [km s^{-1}]	S_{peak} [mJy]	S_{int} [Jy km s^{-1}]	log M_{HI} [M$_\odot$]
03 17 29.7 –08 08 42.8	2023	2.34	131	153	51.69	6.36	9.1
03 17 53.4 –07 17 52.1	5156	2.53	272	309	41.75	8.15	10.0
03 17 57.1 +00 10 08.6	6739	4.18	166	205	18.89	1.79	9.6
03 18 02.8 +00 32 20.3	6148	2.27	291	321	7.95	1.59	9.5
03 18 29.1 –07 53 30.7	2050	2.29	93	103	9.96	0.67	8.1
03 19 26.1 –06 07 16.0	2230	2.11	196	218	21.73	4.12	9.0
03 20 32.8 –06 07 07.6	2327	2.37	81	153	12.56	0.87	8.4
03 22 17.5 –07 05 26.4	2686	3.03	157	177	20.91	2.91	9.0
03 25 01.7 –05 44 44.8	5572	3.33	590	613	27.31	8.25	10.1
03 25 11.6 –06 10 51.4	9928	3.25	266	268	13.65	2.43	10.1
03 33 29.5 –07 33 08.4	5072	2.45	212	228	10.29	1.78	9.4
03 36 21.3 –06 42 53.1	3064	3.29	127	152	41.45	4.76	9.3
03 37 26.4 –05 32 10.8	3955	2.42	110	150	9.2	0.73	8.8
03 37 58.9 –06 16 14.2	6499	2.94	350	380	20.58	3.93	9.9
03 38 39.2 –05 20 50.4	4050	2.41	286	376	12.05	2.63	9.3
03 40 43.0 –06 24 54.5	5157	2.6	271	285	33.28	7.01	10.0
03 42 40.1 –06 22 54.5	6222	3.22	311	327	10.95	1.74	9.5
03 50 40.2 –05 33 13.6	4034	2.57	135	182	13.36	1.85	9.2
03 51 33.9 +00 28 03.7	4519	2.79	208	231	13.39	1.93	9.3
04 11 06.5 –05 42 13.0	2368	2.66	148	182	15.43	1.88	8.7
07 23 33.2 +41 26 05.5	8064	2.35	229	295	30.32	6.4	10.3
07 25 55.4 +40 41 58.9	3651	3.1	157	197	16.03	2.05	9.1
07 27 14.0 +42 12 14.3	2982	3	128	139	18.3	1.71	8.9
07 28 54.9 +40 12 21.7	3496	3.2	140	153	27.04	3.37	9.3
07 29 16.6 +42 16 46.6	6767	3.19	278	294	14.99	2.3	9.7
07 29 54.3 +37 27 06.3	10346	3.01	342	400	11.74	3.38	10.3
07 35 02.3 +32 49 19.5	4580	4.03	472	488	25.39	7.17	9.9
07 35 35.6 +41 57 48.8	3052	2.99	116	163	12.08	1.02	8.7
07 36 11.4 +32 30 54.7	4070	2.65	132	179	21.07	2.61	9.3
07 37 37.1 +41 56 49.4	5792	3.18	346	366	24.49	4.93	9.9
07 38 36.5 +37 38 00.6	3843	2.72	275	297	31.17	5.81	9.6
07 39 01.9 +33 54 58.5	3854	2.75	122	143	15.68	1.67	9.1
07 40 16.3 +32 15 30.0	3882	2.66	248	281	15.72	3.14	9.4
07 40 39.3 +39 13 59.9	3297	2.96	426	453	33.45	10	9.7
07 40 57.9 +39 22 45.2	3174	3.02	132	159	15.4	1.61	8.9
07 43 36.4 +49 40 03.2	5581	3.09	380	403	13.6	2.9	9.7
07 44 37.6 +40 52 59.5	2990	3.3	114	169	20.13	2.12	9.0
07 46 37.7 +44 47 25.8	9161	2.32	117	158	8.12	0.71	9.5
07 50 56.0 +23 53 45.2	2100	2.34	241	260	52.42	8.92	9.3
07 51 08.0 +34 03 22.9	4676	2.57	185	205	18.25	2.76	9.5
07 53 45.3 +39 46 57.3	3847	2.81	102	138	10.96	0.95	8.8
07 54 42.1 +26 38 33.5	4600	1.98	95	126	8.91	0.64	8.8
07 57 10.4 +23 46 47.3	2309	2.52	134	183	12.85	1.6	8.6

Table A.1 continued ...

Coordinates (J2000) hhmmss degrees	V_{HI} [km s^{-1}]	rms [mJy]	W_{50} [km s^{-1}]	W_{20} [km s^{-1}]	S_{peak} [mJy]	S_{int} [Jy km s^{-1}]	log M_{HI} [M$_\odot$]
07 58 20.5 +25 08 57.1	4765	2.43	257	280	25.03	4.85	9.7
07 58 43.7 +32 44 19.7	2986	3.2	146	162	13.12	1.4	8.8
07 59 57.2 +35 48 51.4	5168	2.82	220	241	10.89	2.05	9.4
08 00 23.9 +17 31 21.3	2043	2.46	147	175	17.22	2.07	8.6
08 00 57.9 +54 13 55.1	888	3.22	31	58	21.57	0.72	7.4
08 01 23.1 +15 22 09.3	4549	2.37	124	187	8.06	0.84	8.9
08 05 05.4 +25 03 45.2	4945	2.53	284	298	14.67	1.96	9.4
08 07 24.8 +39 11 40.0	3871	2.66	113	153	30.59	3.7	9.4
08 13 57.2 +52 38 54.4	5339	3.57	569	589	28.56	9.84	10.2
08 18 08.3 +24 30 06.3	2098	2.61	122	265	28.97	5.16	9.1
08 19 12.8 +20 30 38.6	4911	2.92	392	417	39.71	9.09	10.0
08 20 23.7 +21 07 53.2	5163	2.69	46	62	12.11	0.54	8.9
08 20 29.2 +03 29 34.9	2908	2.39	178	199	10.04	0.99	8.6
08 21 24.6 +19 08 52.0	7779	2.28	488	515	14.82	3.62	10.1
08 22 10.7 +03 16 04.9	4070	2.74	252	293	33.81	7.58	9.8
08 23 34.8 +03 13 15.6	2887	1.84	117	144	32.57	3.68	9.2
08 25 44.5 +27 52 28.4	2156	2.49	242	261	12.2	2.27	8.7
08 26 32.9 +23 11 33.9	5551	2.27	427	486	21.11	6.03	10.0
08 27 42.0 +21 28 44.7	4269	3.13	323	340	43.82	8.62	9.9
08 30 01.7 +17 15 35.4	2061	2.9	162	178	11.02	1.45	8.5
08 31 21.6 +07 00 00.1	1223	2.5	126	146	49	5.08	8.9
08 33 30.8 +41 31 31.6	7536	3.34	226	296	11.02	1.28	9.6
08 33 35.6 +25 08 47.1	2212	2.38	61	79	10.71	0.55	8.1
08 33 36.3 +29 30 07.2	2093	3.26	79	136	55.75	4.84	9.0
08 33 42.6 +27 42 43.4	2233	3.26	165	243	12.71	1.9	8.7
08 35 13.8 +28 45 11.9	2054	2.26	164	245	9.04	1.28	8.4
08 37 32.7 +28 42 18.7	3441	2.52	379	403	48.38	12.91	9.9
08 40 22.7 +23 32 22.8	3580	2.59	249	266	30.56	5.31	9.5
08 43 27.0 +04 25 59.4	4268	2.8	135	201	13.16	1.34	9.1
08 44 07.6 +30 07 08.9	2083	4.33	351	370	38.1	9.7	9.3
08 44 08.3 +34 43 02.0	4183	3.21	232	254	19.55	3.06	9.4
08 45 37.9 +36 56 04.7	3869	3.21	26	48	17.33	0.31	8.4
08 46 12.2 +35 41 36.9	3989	2.97	148	185	16.04	2.02	9.2
08 46 34.4 +36 26 20.8	3181	2.89	97	149	9.83	0.76	8.6
08 47 19.6 +05 53 52.5	3869	2.94	99	113	10	0.7	8.7
08 47 41.7 +13 25 08.8	2052	2.43	130	157	155.28	19.47	9.6
08 48 03.5 +25 20 01.5	1937	2.46	60	105	9.35	0.49	8.0
08 54 24.0 +34 33 21.7	2182	3.03	59	81	90.29	5.59	9.1
08 56 40.7 +00 22 30.0	2492	2.21	151	175	55.03	7.73	9.4
08 57 20.5 +02 55 16.7	3863	2.54	609	631	16	6.13	9.7
08 58 41.0 +02 11 35.4	2425	2.16	74	108	17.71	1.22	8.6
09 00 13.1 +31 59 58.3	1937	2.81	54	115	9.95	0.61	8.1
09 00 20.2 +52 29 39.2	8781	3.41	508	560	13.64	4.51	10.3

Table A.1 continued ...

Coordinates (J2000) hhmmss degrees	V_{HI} [km s^{-1}]	rms [mJy]	W_{50} [km s^{-1}]	W_{20} [km s^{-1}]	S_{peak} [mJy]	S_{int} [Jy km s^{-1}]	log M_{HI} [M$_\odot$]
09 05 12.5 +05 52 05.2	3863	2.59	121	136	15.28	1.18	8.9
09 08 51.0 +03 26 54.0	3822	2.68	134	147	11.26	1	8.9
09 09 20.2 +01 36 51.5	1318	2.9	77	99	12.47	0.77	7.8
09 09 33.7 +33 07 24.7	1926	3.18	329	360	81.41	23.85	9.6
09 10 32.1 +50 25 59.7	5029	3.32	218	257	17.93	2.9	9.6
09 10 41.8 +07 12 24.1	1478	5.31	116	178	40.36	5.07	8.7
09 12 14.5 +44 57 17.4	2604	3.62	174	207	139.73	23.02	9.9
09 13 31.4 +28 57 06.3	7675	3.13	578	598	11.89	2.83	9.9
09 14 59.7 +29 43 48.8	6188	2.37	322	348	8.53	2.17	9.6
09 16 23.8 +43 11 19.5	2585	3.99	133	216	32.72	4.34	9.2
09 17 05.3 +25 25 44.9	1670	3.43	58	157	12.01	0.82	8.1
09 17 39.9 +52 59 34.5	−2301	4.56	0	0	18.7	0	0.0
09 19 58.0 +37 11 28.5	2244	2.58	365	389	42.31	9.1	9.4
09 20 02.2 +01 02 17.8	5219	2.49	300	314	10.21	1.42	9.3
09 20 59.6 +11 03 33.2	1325	2.39	143	159	28.2	2.66	8.4
09 24 27.9 +46 31 44.7	4192	3.04	30	118	9.73	0.22	8.3
09 24 55.1 +26 46 28.8	4024	2.49	570	601	20.42	8.56	9.8
09 28 59.1 +28 45 28.6	1215	2.27	91	120	14.98	1.2	7.9
09 30 10.3 +07 54 09.8	2001	2.31	290	325	9.24	1.37	8.4
09 37 58.0 +25 29 41.2	4000	2.81	299	340	17.11	3.75	9.5
09 38 07.9 +09 31 26.0	3296	2.58	336	364	71.98	15.85	9.9
09 38 36.2 +43 10 36.4	1719	3.06	166	186	17.75	2.59	8.6
09 38 57.1 +00 41 33.5	2063	3.08	78	108	36.34	2.92	8.8
09 40 43.2 +03 57 34.9	1320	2.72	110	161	19.58	2.08	8.3
09 43 02.2 +05 01 44.4	1951	2.66	98	110	11.17	0.84	8.2
09 43 12.0 +31 55 43.3	1334	2.91	197	268	24.44	4.73	8.6
09 44 46.2 +00 41 18.3	1220	2.68	121	144	54.4	6.03	8.6
09 46 29.1 +30 39 52.7	1449	2.63	100	120	27.09	2.33	8.4
09 49 41.2 +32 13 15.9	1517	3.15	73	163	16.07	1.47	8.2
09 50 10.9 +28 00 47.7	1435	2.16	70	107	41.9	3.07	8.5
09 50 27.4 +12 45 55.7	1421	3.06	215	250	92.72	15.51	9.2
09 50 55.4 +28 33 04.0	1480	3.79	208	251	49.27	9.7	9.0
09 54 49.6 +09 16 15.9	1490	2.25	202	222	55.13	9.27	9.0
09 55 18.1 +04 16 12.0	1810	2.68	259	281	38.86	8.91	9.2
09 57 32.8 +33 37 11.0	1459	2.74	155	192	23.02	2.98	8.5
09 58 53.4 +47 44 12.6	1161	3.57	166	190	86.04	13	8.9
09 59 18.7 +47 36 58.4	1100	3.48	94	112	18.79	1.8	8.0
10 00 06.2 +45 31 09.6	1718	2.48	131	150	16.12	1.84	8.4
10 00 27.1 +03 22 27.7	2038	2.32	365	386	45.24	13.37	9.4
10 00 31.6 +03 12 19.0	2063	2.47	347	374	34.75	8.33	9.2
10 07 11.5 +33 01 38.5	1333	2.43	205	232	79.22	15.41	9.1
10 09 17.4 +05 24 14.6	1699	2.89	88	118	14.6	1.04	8.2
10 10 27.9 +27 57 21.9	4694	2.59	232	252	11.91	2	9.3

Table A.1 continued ...

Coordinates (J2000) hhmmss degrees	V_{HI} [km s^{-1}]	rms [mJy]	W_{50} [km s^{-1}]	W_{20} [km s^{-1}]	S_{peak} [mJy]	S_{int} [Jy km s^{-1}]	log M_{HI} [M$_\odot$]
10 10 39.9 +20 04 12.6	3776	2.7	424	444	22.41	6.89	9.7
10 13 31.3 +03 22 30.0	1328	5.25	140	158	38.85	4.99	8.6
10 13 58.9 +07 01 26.4	1210	2.8	211	235	145.32	26.67	9.3
10 14 14.3 +03 27 59.4	1213	2.53	422	482	138.39	47.08	9.5
10 14 51.5 +03 38 52.5	1022	2.41	52	104	78.57	6.29	8.5
10 16 21.7 +37 46 48.6	1160	3	94	143	64.5	6.08	8.6
10 17 02.3 +03 38 45.6	1042	2.34	46	59	9.36	0.29	7.2
10 17 47.9 +21 52 24.0	1579	2.9	211	246	40.02	7.35	9.0
10 20 13.9 +06 48 09.4	3725	2.94	58	157	27.93	2.21	9.2
10 20 43.3 +65 10 19.4	3289	4.25	202	223	17.47	1.95	9.0
10 21 47.6 +56 55 49.5	1160	4.75	168	198	157.22	23.03	9.2
10 30 49.7 +23 57 54.2	1338	2.74	43	61	9.86	0.15	7.1
10 32 31.9 +54 24 03.7	1445	4.11	115	165	34.52	3.42	8.5
10 32 34.8 +65 02 27.9	1662	4.85	237	268	167.32	26.76	9.6
10 34 29.8 +35 15 24.3	1510	3.05	151	227	21.05	2.97	8.5
10 34 42.8 +11 11 50.4	1370	2.64	323	363	14.26	2.88	8.4
10 34 56.1 +11 29 32.5	1169	2.56	83	96	10.75	0.56	7.6
10 35 48.9 +08 28 59.8	1164	2.37	81	131	22.52	1.83	8.1
10 36 16.2 +37 19 28.8	1584	3.11	391	411	35.14	10.73	9.1
10 39 20.5 +00 12 00.8	5451	2.33	125	165	9.55	0.92	9.1
10 42 07.5 +13 44 49.1	1306	2.81	304	344	170.29	42.65	9.6
10 42 48.4 +13 27 35.4	1208	2.57	84	157	43	4.17	8.5
10 42 52.4 +13 44 27.8	1205	2.34	151	175	7.49	0.78	7.7
10 43 05.5 +13 30 37.3	1255	2.73	67	112	25.55	1.83	8.2
10 45 22.4 +55 57 37.3	935	4.28	84	125	96.3	8.26	8.5
10 46 34.9 +13 45 03.0	3009	2.92	224	254	58.98	12.25	9.7
10 48 24.8 +34 42 41.0	1626	3.5	77	132	132.65	11.72	9.2
10 51 46.5 +32 54 00.1	1499	3.16	341	378	39.5	12.64	9.1
10 53 08.1 +33 54 37.3	1730	2.82	125	180	21.71	2.72	8.6
10 55 39.2 +02 23 44.7	1026	2.49	97	135	21.17	2.02	8.0
10 56 13.9 +12 00 40.6	984	2.34	48	80	25.74	1.45	7.8
10 57 38.1 +13 58 44.5	1233	2.88	89	113	23.62	2.07	8.2
10 59 09.0 +61 31 50.4	2112	4.15	89	107	18.26	1.27	8.4
11 00 23.8 +16 41 31.7	947	2.82	165	178	19.06	2.56	8.1
11 01 23.6 +57 40 39.6	2967	4.92	244	289	41.82	7.79	9.5
11 07 03.4 +12 03 36.1	1551	2.89	243	263	46.24	7.96	9.0
11 09 55.9 +10 43 15.0	1588	3.08	147	233	40.96	6.08	8.9
11 10 44.8 +04 50 47.2	5734	2.9	421	442	14.09	2.97	9.7
11 10 56.5 +61 20 49.2	1645	3.71	168	187	28.09	3.91	8.7
11 10 56.9 +53 23 15.9	2832	8.13	412	433	54.47	16.53	9.8
11 13 00.2 +07 51 42.7	1394	2.9	86	125	19.72	1.4	8.1
11 14 10.9 +48 19 06.6	2123	3.3	328	354	69.3	18.81	9.6
11 16 26.3 +04 20 11.4	1105	2.59	144	160	12.17	1.55	8.0

Table A.1 continued ...

Coordinates (J2000) hhmmss degrees	V_{HI} [km s^{-1}]	rms [mJy]	W_{50} [km s^{-1}]	W_{20} [km s^{-1}]	S_{peak} [mJy]	S_{int} [Jy km s^{-1}]	log M_{HI} [$M_\odot$]
11 19 28.1 +09 35 44.2	983	2.37	54	84	26.07	1.87	7.9
11 20 12.4 +67 14 29.6	1306	4.95	154	177	59.9	8.7	8.9
11 20 26.2 +03 35 08.2	2584	2.79	298	358	14.79	2.79	9.0
11 20 31.3 +57 46 53.0	1964	4.06	241	262	38.98	5	9.0
11 20 31.8 +26 57 48.1	1500	3.08	205	233	78.48	15.06	9.2
11 21 51.3 +03 24 17.4	1167	2.83	81	115	28.58	2.16	8.2
11 22 17.9 +59 04 28.2	1576	4.5	88	107	170.55	13.71	9.2
11 22 23.2 +13 04 40.1	1306	2.67	610	630	14.95	3.36	8.4
11 22 39.0 +37 45 54.3	1986	3.16	230	253	79.63	14.8	9.5
11 24 26.1 +11 20 31.9	1051	2.26	255	273	102.38	24.9	9.1
11 24 44.5 +15 16 31.4	1135	2.87	126	172	13.49	1.49	8.0
11 25 26.8 +57 43 16.4	1832	3.57	220	249	28.92	5.53	9.0
11 25 30.4 +63 26 46.7	3676	4.3	58	75	30.1	1.34	9.0
11 25 53.5 +09 59 14.9	1152	2.18	52	93	48.4	2.79	8.3
11 26 08.3 +04 03 44.5	1512	3.02	50	62	11.48	0.42	7.7
11 26 44.3 +59 09 19.5	1202	4.95	106	148	48.51	4.81	8.5
11 27 10.9 +08 43 51.7	1039	2.45	47	80	38.47	1.98	8.0
11 27 31.8 +56 52 37.4	1718	4.91	344	400	40.26	11.71	9.2
11 28 24.0 +09 24 27.4	1733	2.52	402	420	31.75	7.55	9.0
11 29 06.5 +08 59 18.9	6124	2.62	468	508	12.6	4.38	9.9
11 29 59.4 +63 13 24.1	1031	5.56	100	138	21.13	1.88	8.0
11 30 17.3 +58 08 02.0	1433	3.16	85	110	58.78	4.8	8.7
11 31 32.1 –02 18 33.0	4672	2.6	101	133	96.2	10.27	10.1
11 32 01.9 +14 36 38.8	1122	2.34	130	146	10.3	1.16	7.9
11 32 02.4 +36 41 52.7	2480	2.9	235	258	36.25	6.18	9.3
11 32 20.3 +53 54 16.0	2792	4.09	193	208	21.15	3.7	9.2
11 32 44.0 +02 28 24.8	1034	2.89	27	59	32.66	0.91	7.7
11 33 45.3 –03 26 13.2	1595	3.03	140	155	79.39	10.78	9.1
11 33 50.1 +14 49 28.2	1141	2.41	60	78	7.47	0.28	7.3
11 34 19.5 +13 19 19.1	1194	2.92	66	111	51.1	3.95	8.4
11 35 18.4 +04 57 17.2	1402	2.6	68	106	16.38	1.02	8.0
11 36 26.5 +58 11 28.9	1206	4.32	212	244	56.16	10.63	8.9
11 36 33.4 +36 24 37.2	1556	2.63	258	289	107.83	26.23	9.5
11 36 48.0 +54 17 36.8	1282	4.04	288	311	103.83	19.11	9.2
11 36 58.0 +55 09 43.4	5655	3.65	64	117	25.55	1.9	9.5
11 37 37.0 +16 33 22.3	1029	3.14	153	182	57.78	7.75	8.6
11 37 51.0 +56 08 31.0	2266	3.91	153	173	38.59	5.35	9.1
11 38 02.1 +35 12 12.9	1609	2.7	175	194	46.22	7.22	9.0
11 38 17.3 +00 36 48.1	945	3.19	31	50	18.18	0.52	7.4
11 38 51.5 +43 09 56.3	1194	3.13	158	190	27.23	4.1	8.5
11 39 01.1 +01 20 11.6	1546	2.4	93	149	14.16	1.14	8.1
11 39 21.3 +58 16 07.3	1142	3.81	107	131	104.01	10.93	8.8
11 39 22.3 +56 16 14.3	2364	4.9	296	361	51.94	13.94	9.6

Table A.1 continued ...

Coordinates (J2000) hhmmss degrees	V_{HI} [km s^{-1}]	rms [mJy]	W_{50} [km s^{-1}]	W_{20} [km s^{-1}]	S_{peak} [mJy]	S_{int} [Jy km s^{-1}]	log M_{HI} [M$_\odot$]
11 40 18.5 +09 00 35.5	1831	2.83	240	255	12.45	2.39	8.6
11 41 07.5 +32 25 37.2	1817	3.03	80	134	23.03	1.82	8.5
11 42 26.3 +51 35 52.7	976	3.13	179	197	42.26	6.48	8.5
11 43 16.1 –01 23 40.9	1904	2.43	40	56	8.26	0.18	7.5
11 43 27.0 +11 23 54.3	902	2.86	87	107	8.72	0.63	7.4
11 43 31.1 +55 28 44.0	959	3.58	143	163	27.57	3.24	8.2
11 43 34.7 +08 56 32.8	5864	2.95	497	510	11.51	2.91	9.7
11 44 04.9 +60 07 11.2	2440	5.12	398	462	23.55	4.71	9.1
11 44 10.6 –03 40 07.6	1208	2.12	62	90	18.66	1.18	7.9
11 44 14.8 +55 02 05.9	1423	4.04	126	167	51.31	6.03	8.8
11 44 52.1 +57 52 24.6	1275	3.87	43	74	23.61	0.84	7.8
11 45 35.6 +55 53 12.8	1156	5	169	185	41	5.7	8.6
11 45 45.6 +10 49 28.5	3082	2.68	50	101	8.58	0.34	8.2
11 46 07.8 +47 29 41.1	893	2.03	336	362	64.84	15.22	8.8
11 47 00.7 +00 17 39.1	1428	2.03	142	0	6.09	0.56	7.7
11 47 34.4 +55 58 02.0	2337	5.54	280	316	43.77	10.02	9.4
11 47 45.3 +59 53 12.0	1261	4.62	89	216	23.56	2.39	8.3
11 48 03.4 +30 21 33.5	6149	2.47	396	440	27.66	8.35	10.2
11 48 10.6 –01 59 20.8	1523	4.06	93	106	25.98	2.13	8.4
11 48 50.4 –02 01 56.0	1723	3.65	221	236	140.89	22.96	9.5
11 50 04.4 +26 28 45.2	1769	2.48	206	247	24.83	4.24	8.8
11 50 34.0 +00 32 16.2	1747	4.28	187	200	34.24	4.49	8.8
11 50 56.0 +14 35 41.4	1005	1.81	47	88	55.55	3.1	8.2
11 52 39.1 +50 02 16.0	994	4.14	71	114	54.65	3.87	8.3
11 53 14.1 –03 24 32.2	1262	2.7	60	144	11.07	0.56	7.6
11 54 12.3 +00 08 11.8	1133	2.52	38	112	12.35	0.55	7.5
11 54 25.0 –02 19 10.4	2353	3.22	231	259	46.37	7.05	9.3
11 54 33.7 +58 22 01.3	3364	5.96	435	497	29.8	5.64	9.5
11 55 04.9 +01 43 11.3	1298	3.27	128	180	16.02	2.06	8.2
11 55 28.7 +11 58 06.1	6251	2.59	478	505	56.72	15.64	10.5
11 55 54.9 +40 55 18.5	1103	3.42	56	96	25.99	1.47	7.9
11 56 10.3 +60 31 21.1	9665	4.88	131	146	32.21	3.25	10.2
11 56 28.1 +55 07 30.8	1105	4.82	214	247	85.8	15.41	9.0
11 56 55.4 +57 30 47.4	1068	3.74	142	176	31.04	4.12	8.4
11 57 12.4 –02 41 11.3	1380	3.36	34	57	25.87	0.86	7.9
11 57 35.3 +02 10 04.2	997	1.79	65	0	7.34	0.45	7.3
11 58 34.3 +53 20 43.7	1110	3.92	111	136	20.38	1.9	8.1
11 59 00.7 +04 40 10.7	1599	2.97	0	0	9.8	0.55	7.8
11 59 09.4 +52 42 27.3	1071	7.68	173	190	122.88	19.43	9.0
11 59 10.3 –02 35 27.2	1542	3.76	108	130	36.47	3.59	8.6
12 00 47.4 –03 25 12.3	1501	2.67	108	212	27.77	2.57	8.5
12 01 10.5 +14 06 13.5	1492	2.85	199	223	44.18	7.69	8.9
12 01 22.3 +02 11 08.3	966	2.35	34	48	18.33	0.56	7.4

Table A.1 continued ...

Coordinates (J2000) hhmmss degrees	V_{HI} [km s^{-1}]	rms [mJy]	W_{50} [km s^{-1}]	W_{20} [km s^{-1}]	S_{peak} [mJy]	S_{int} [Jy km s^{-1}]	log M_{HI} [M$_\odot$]
12 01 23.7 +13 24 03.6	925	2.68	89	105	35.54	2.92	8.1
12 02 12.2 +62 08 13.9	1214	5.45	222	257	128.62	24.8	9.3
12 02 42.2 +01 58 36.5	1964	3.35	298	325	43.22	11.88	9.4
12 03 40.1 +02 38 28.3	1222	1.83	119	145	13.54	1.37	8.0
12 04 04.3 +04 48 47.1	2191	2.48	112	0	16.62	1.75	8.6
12 04 12.5 +00 48 09.3	2906	2.42	113	0	7.5	0.7	8.5
12 05 19.9 +00 28 48.7	1349	2.42	28	79	15	0.52	7.7
12 05 36.0 +41 17 21.9	1022	3.13	31	64	29.11	0.94	7.7
12 07 41.3 +39 22 45.9	1055	3.53	39	53	21.18	0.71	7.6
12 07 46.1 +43 07 34.8	908	3.36	247	311	19.15	3.14	8.1
12 08 11.1 +02 52 41.8	1319	2.86	205	226	174.46	30.69	9.4
12 08 20.0 +02 30 19.9	1972	2.47	80	0	8.65	0.69	8.1
12 08 42.3 +36 48 09.9	1074	2.96	130	154	163.39	20.25	9.1
12 08 47.3 +29 18 17.2	3973	3.3	295	335	11.22	1.9	9.2
12 09 10.0 +29 10 36.8	3801	2.72	336	425	56.03	16.41	10.1
12 09 49.1 +43 14 04.8	1053	3.11	74	88	33.59	2.34	8.1
12 10 35.7 +11 45 38.9	1290	2.27	191	220	15.66	2.77	8.4
12 10 54.5 +39 45 26.5	1150	4.4	118	150	88	9.08	8.8
12 11 19.9 +01 29 32.2	2091	3.17	184	242	34.87	5.15	9.0
12 11 21.8 +38 32 23.5	1072	2.84	45	71	40.33	1.86	8.0
12 11 27.5 +02 55 34.6	1272	3.25	95	117	78.65	6.84	8.7
12 12 10.9 +02 52 55.7	2077	3.03	39	0	12.42	0.31	7.8
12 12 14.7 +00 04 20.2	2321	2.34	75	110	14.51	1.1	8.5
12 12 31.9 +29 09 58.7	3908	3.39	325	407	17.63	3.92	9.5
12 12 32.3 +12 07 25.7	2191	2.55	240	264	50.75	9.28	9.3
12 13 53.6 +13 10 22.2	2436	3.48	333	349	22.62	4.34	9.1
12 15 56.3 +14 25 58.9	1396	2.67	56	261	12.55	0.77	7.9
12 15 58.5 +02 02 22.0	6305	2.26	60	116	7.01	0.46	9.0
12 16 00.4 +04 39 03.5	2142	3.09	124	177	32.75	3.83	8.9
12 16 38.7 −01 27 06.6	900	2.63	44	64	23.93	0.9	7.6
12 19 09.9 +03 51 23.5	1513	4.11	46	85	46.85	2.42	8.4
12 19 52.6 +27 37 15.6	2300	2.91	155	175	11.06	1.43	8.6
12 20 25.8 +33 14 31.7	1055	2.06	45	100	7.73	0.41	7.4
12 20 35.5 +30 47 48.7	1109	2.53	42	105	24.29	1.26	7.9
12 20 47.5 +58 05 33.0	3012	3.9	332	350	20.67	5.76	9.4
12 20 54.6 +03 24 09.6	2319	2.35	370	0	9.17	1.84	8.7
12 21 32.8 +14 36 22.2	1116	2.25	338	376	51.75	14.31	8.9
12 21 57.8 +02 20 42.3	1812	1.64	147	171	8.36	0.96	8.2
12 22 42.2 +09 19 56.9	1254	2.93	308	321	24.32	5.21	8.6
12 22 56.6 +02 44 49.0	1815	2.6	112	170	12.22	1.12	8.3
12 23 23.4 +01 48 54.2	1836	2.44	124	141	10	0.9	8.2
12 23 30.0 +02 00 29.1	1818	2.47	118	182	12.35	1.32	8.3
12 23 53.9 −03 26 34.5	1988	3.18	377	451	49.29	10.58	9.3

Table A.1 continued ...

Coordinates (J2000)	V_{HI}	rms	W_{50}	W_{20}	S_{peak}	S_{int}	log M_{HI}
hhmmss degrees	[km s^{-1}]	[mJy]	[km s^{-1}]	[km s^{-1}]	[mJy]	[Jy km s^{-1}]	[M$_\odot$]
12 24 01.5 +12 12 17.1	2302	2.28	98	123	36.94	3.48	9.0
12 25 50.7 +10 27 32.6	1095	3.61	125	166	39.71	4.42	8.4
12 26 54.6 +00 52 39.4	2183	2.63	89	146	10.26	0.85	8.3
12 30 26.8 +04 14 47.6	2429	2.52	304	319	35.28	7.04	9.3
12 32 33.5 +09 10 25.1	1161	2.63	74	120	21.57	1.52	8.0
12 34 34.1 +63 31 30.2	2707	5.68	254	277	59.64	10.55	9.6
12 37 48.4 +05 22 06.6	1056	2.46	216	239	7.38	0.83	7.7
12 39 50.3 +01 40 21.4	1226	2.61	101	114	18.3	1.62	8.1
12 40 08.7 +00 21 04.8	1705	2.68	31	74	18.65	0.8	8.1
12 41 11.6 +01 24 37.0	1680	2.94	125	179	52.89	6.45	9.0
12 41 12.2 +11 53 11.9	2232	2.4	218	264	15.41	3.09	8.9
12 42 40.7 +13 16 00.8	1100	4.22	50	0	46.42	3.87	8.4
12 43 56.6 +13 07 36.0	1044	2.32	283	312	120.64	30.16	9.2
12 44 28.8 +00 28 05.0	1177	3.21	110	132	95.02	9.59	8.8
12 45 32.0 +00 32 08.6	1606	3.07	144	171	92.1	11.24	9.2
12 47 45.6 +13 45 46.1	1612	2.82	183	203	29.89	4.78	8.8
12 48 00.1 +04 26 03.3	986	3.06	45	75	92.11	4.58	8.3
12 49 25.7 +04 23 33.1	2628	3.47	101	118	38.17	3.17	9.0
12 50 38.9 +01 27 52.2	1247	2.78	187	237	20.02	2.71	8.3
12 52 59.1 +14 24 01.9	1051	2.62	84	115	19.39	2.03	8.0
12 53 21.2 +01 16 08.7	1126	2.5	282	297	41.25	8.24	8.7
12 54 40.6 +28 56 19.2	2479	2.82	311	357	77.55	20.51	9.8
12 55 12.6 +00 06 59.9	1312	2.81	190	209	107.2	16.21	9.1
12 55 21.9 +58 20 38.7	2482	4.85	352	388	65.48	19.82	9.8
13 04 31.8 -02 59 16.9	1272	3.12	68	85	44.93	2.95	8.4
13 05 24.9 +56 19 21.9	2524	4.39	234	278	33.94	5.53	9.2
13 06 04.4 +55 39 21.9	8108	3.57	124	160	56.76	5.95	10.3
13 09 33.1 +01 40 23.0	5519	3.37	435	493	19.21	5.31	9.9
13 11 31.2 +36 16 55.6	1124	2.87	114	195	57.11	6.76	8.6
13 14 10.8 +39 08 55.4	1134	2.89	119	147	31.79	3.75	8.4
13 16 00.6 +40 58 09.8	1109	2.92	70	92	22.19	1.5	8.0
13 16 52.3 +12 32 53.6	960	2.92	165	199	61.9	9.93	8.7
13 18 45.1 +41 56 58.7	1259	3.01	133	160	39.13	5.09	8.6
13 20 32.1 +05 24 29.1	950	3.29	72	161	14.15	1.07	7.7
13 20 38.7 +09 47 10.0	1122	3.09	139	156	70.7	8.89	8.7
13 23 10.5 +43 05 10.5	8059	4.05	259	293	24.3	4.81	10.2
13 25 13.9 +43 16 02.1	1214	3.4	222	260	73.1	13.43	9.0
13 26 36.6 +42 45 51.4	1224	3.57	149	170	40.34	5.97	8.6
13 27 02.6 +42 46 49.2	1251	3.53	105	125	18.36	1.77	8.1
13 27 24.6 +45 26 18.9	1252	4.36	93	122	34.01	3.22	8.4
13 29 25.9 +11 00 28.4	6716	3.75	568	592	54.38	14.26	10.5
13 30 03.6 +62 30 41.6	1749	5.29	255	275	66.65	11.49	9.2
13 32 10.4 +62 46 03.9	2940	4.75	226	256	19	2.83	9.1

Table A.1 continued ...

Coordinates (J2000) hhmmss degrees	V_{HI} [km s^{-1}]	rms [mJy]	W_{50} [km s^{-1}]	W_{20} [km s^{-1}]	S_{peak} [mJy]	S_{int} [Jy km s^{-1}]	log M_{HI} [M$_\odot$]
13 33 05.3 –01 02 08.8	3676	2.14	279	316	35.29	7.15	9.7
13 33 14.7 +45 50 13.8	1324	3.57	121	136	28.92	2.75	8.4
13 33 31.8 +38 36 19.5	1184	2.24	139	156	34.5	4.49	8.5
13 35 16.2 +44 45 41.1	2604	3.39	182	218	24.41	3.56	9.1
13 35 42.7 +45 55 46.4	1438	3.96	44	68	90.68	4.29	8.6
13 36 01.2 +49 57 39.0	1603	4.48	264	290	22.85	4.69	8.8
13 36 22.9 +39 42 16.5	2418	3.2	91	0	13.44	1.1	8.5
13 38 30.6 +08 26 32.3	1020	2.17	119	141	32.38	3.68	8.3
13 39 36.0 +43 03 10.0	3498	3.13	77	137	31.93	2.71	9.2
13 40 15.2 +38 52 09.5	3917	3.27	318	332	10.14	1.36	9.0
13 40 29.8 +42 59 33.6	2831	3.08	160	0	17.86	2.33	9.0
13 40 39.9 +54 19 58.3	2001	3.74	230	251	74.8	13.58	9.4
13 40 43.3 +39 33 10.5	3333	3.11	147	166	12.44	1.02	8.8
13 45 19.2 +41 42 45.2	2542	3.29	454	476	29.61	9.89	9.5
13 46 18.7 +43 51 04.8	2405	2.8	394	423	125.16	34.14	10.0
13 46 24.7 +46 06 25.3	1507	7.75	304	329	110.83	27.01	9.5
13 47 45.5 +38 15 33.2	1409	2.79	154	228	48.83	7.86	8.9
13 48 16.0 +03 57 03.1	1161	2.1	206	225	69.72	11.66	8.9
13 48 56.1 +39 59 06.6	2792	2.7	0	0	9.72	0.54	8.3
13 49 44.3 +39 59 05.1	2549	4.14	400	432	22.77	6.36	9.3
13 51 31.1 +39 27 17.0	1836	2.46	142	205	11.32	1.38	8.4
13 52 04.2 –02 12 23.8	4310	3.76	82	110	103.78	8.5	9.9
13 52 34.9 +38 42 18.7	2401	2.78	165	200	15.57	2.18	8.8
13 52 54.5 –01 06 52.6	1368	3.24	211	230	148.07	19.74	9.3
13 53 21.6 +40 21 50.1	2304	3.24	294	317	103.36	20.49	9.7
13 53 38.4 +36 08 02.5	8260	3.87	0	0	16.25	0.67	9.4
13 54 58.4 +05 20 01.4	1434	1.91	124	150	28.08	2.88	8.5
13 55 34.3 +59 44 34.1	1593	9.35	139	18	47.69	5.05	8.8
13 55 39.9 +40 27 42.3	2531	4.33	384	408	101.75	22.03	9.8
13 56 09.3 +05 32 33.3	1082	2.27	40	58	10.67	0.37	7.3
13 56 51.0 +37 47 50.0	2952	2.68	294	311	15.81	3.07	9.1
13 57 11.5 +50 26 08.5	1867	3.22	207	255	14.17	2.15	8.6
13 57 19.2 +11 58 33.6	6048	2.69	282	296	15.6	2.98	9.7
13 58 37.9 +37 25 28.1	3417	2.76	545	640	36.16	16.7	10.0
13 58 37.9 +60 47 48.5	1617	4.18	145	159	38.04	4.68	8.8
14 00 20.1 +38 54 55.5	5291	3.28	364	382	23.29	4.53	9.8
14 00 45.7 +59 19 41.8	2934	4.54	306	334	32.23	5.53	9.4
14 02 54.1 +49 10 15.6	2048	3.19	274	423	56.46	16.29	9.5
14 03 00.8 +50 00 43.6	1886	3.93	102	134	12.38	1.19	8.3
14 03 12.1 +11 43 11.5	5185	1.84	267	308	6.26	1.07	9.2
14 03 36.7 +39 03 10.1	5707	2.99	198	245	18.12	2.69	9.6
14 06 21.6 +50 43 30.3	1876	3.2	190	228	28.8	4.4	8.9
14 06 31.9 +06 01 46.8	1015	2.91	244	261	18.62	3.58	8.3

Table A.1 continued ...

Coordinates (J2000) hhmmss degrees	V_{HI} [km s^{-1}]	rms [mJy]	W_{50} [km s^{-1}]	W_{20} [km s^{-1}]	S_{peak} [mJy]	S_{int} [Jy km s^{-1}]	log M_{HI} [$M_\odot$]
14 07 25.0 +55 06 11.0	1378	3.43	174	206	67.23	11.31	9.0
14 08 58.1 –02 58 25.6	1615	2.2	79	110	15.18	1.05	8.1
14 10 00.7 +39 11 54.1	1477	3.12	80	120	9.67	0.7	7.9
14 10 03.1 +54 13 05.8	1808	3.41	204	221	30.35	5.16	8.9
14 10 12.9 –02 34 32.9	1555	2.14	212	261	111.92	21.05	9.4
14 10 15.2 +48 32 45.9	2000	4.26	62	0	15.76	0.87	8.2
14 10 35.9 +59 21 28.7	3033	4.7	213	255	35.72	5.53	9.4
14 11 49.6 +47 57 58.8	2088	3.92	112	135	19.6	1.77	8.6
14 11 53.4 +38 11 37.8	5996	2.77	479	524	18.28	5.91	10.0
14 13 36.9 +47 24 21.0	2121	2.77	151	180	29.64	4.39	9.0
14 14 54.1 –02 08 22.9	1557	2.26	41	119	10.85	0.53	7.8
14 15 34.1 +36 13 35.6	2868	3.36	572	609	49.73	23.96	10.0
14 17 04.2 –01 30 20.1	1557	4.03	66	93	40.7	2.51	8.5
14 19 20.2 +01 09 54.6	2418	1.91	101	135	9.74	0.77	8.3
14 20 26.5 +35 11 19.6	3579	4.06	113	217	49.94	6.82	9.6
14 20 32.1 +03 58 59.6	1761	3.04	81	108	75.39	6.1	9.0
14 20 40.3 +40 18 55.1	1266	3.29	73	125	17.44	1.24	8.0
14 20 43.5 +04 08 37.1	1773	2.58	61	105	11.87	0.59	8.0
14 20 44.5 +08 37 35.8	1293	2.53	84	115	26.01	2.26	8.3
14 20 55.9 +03 14 16.8	1599	2.49	72	144	10.46	0.7	7.9
14 22 12.2 –01 53 28.7	1001	2.73	81	135	10.1	0.76	7.6
14 22 23.8 +00 23 15.6	1630	2.66	198	219	115.44	19.88	9.4
14 23 27.1 +01 43 34.6	1389	3.18	217	237	115.75	18.37	9.2
14 24 24.3 +08 16 34.1	1248	2.98	115	140	39.04	4.37	8.5
14 25 21.0 +39 32 22.4	1437	2.66	172	200	86.18	12.85	9.1
14 26 35.2 +51 35 07.3	1898	3.72	100	133	19.72	2.01	8.6
14 26 59.8 +08 41 01.0	1359	2.57	145	169	52.17	7.36	8.8
14 27 10.7 +05 08 08.3	1563	2.7	89	114	21.6	1.62	8.3
14 27 28.4 +46 08 47.5	2313	3.75	276	297	42.38	8.48	9.4
14 28 18.4 +13 46 48.8	1280	2.22	192	212	81.25	14.76	9.1
14 30 25.5 +35 19 15.7	3105	3.08	344	435	27.41	7.26	9.5
14 30 39.3 +07 16 30.3	1351	2.96	180	206	78.44	13.11	9.1
14 32 05.6 +57 55 17.1	1897	4.54	387	412	46.31	14.15	9.4
14 32 46.8 +49 27 28.4	2108	3.95	448	476	63.99	20.26	9.6
14 33 24.3 +04 27 01.7	1571	2.91	106	132	196.13	19.49	9.4
14 35 39.9 +13 10 11.7	1795	2.55	190	238	63.5	12.02	9.3
14 37 13.6 +43 41 45.4	3259	2.83	308	325	21.59	4.8	9.4
14 37 30.8 +51 33 42.6	2186	2.71	405	425	40.38	10.88	9.4
14 38 18.1 +03 24 37.1	1585	2.55	165	195	18.62	2.45	8.5
14 39 52.2 +42 44 32.4	2505	3.34	271	300	46.09	11.11	9.5
14 40 03.5 +34 05 59.5	1498	3.15	89	162	24.26	2.39	8.4
14 40 26.1 +33 59 20.8	1479	3.13	189	208	68.23	11.94	9.1
14 40 56.4 +00 19 05.5	1725	3.7	379	418	79.55	23.94	9.5

Table A.1 continued ...

Coordinates (J2000)	V_{HI}	rms	W_{50}	W_{20}	S_{peak}	S_{int}	log M_{HI}
hhmmss degrees	[km s^{-1}]	[mJy]	[km s^{-1}]	[km s^{-1}]	[mJy]	[Jy km s^{-1}]	[M$_\odot$]
14 40 58.3 +02 11 11.5	1621	2.44	145	166	24.4	3.19	8.6
14 41 32.0 +44 30 45.9	3221	2.7	216	252	19.71	3.47	9.3
14 42 33.2 +28 43 35.2	3693	2.61	233	257	62.69	10.87	9.9
14 42 45.9 +00 21 03.9	1697	2.72	126	220	30.36	4.21	8.8
14 42 57.9 +04 53 27.7	1633	2.43	307	323	71.52	16.59	9.3
14 44 24.4 +01 40 47.1	1559	6.66	325	348	88.58	20.96	9.4
14 46 20.2 +04 43 58.7	1514	2.69	47	116	13.99	0.59	7.8
14 46 21.1 +34 22 14.0	1627	2.57	122	174	53.46	6.52	8.9
14 47 44.5 +36 30 16.8	1242	2.65	51	138	17.49	1.13	7.9
14 50 56.6 +35 34 19.5	1205	2.88	85	131	42.91	3.58	8.4
14 51 06.7 +02 31 26.9	2089	2.39	67	133	11.71	0.77	8.2
14 51 14.4 +35 32 32.1	1251	2.71	169	206	43.36	6.84	8.7
14 52 07.9 –02 31 47.0	1945	2.29	182	207	77.17	12.3	9.4
14 53 05.2 +03 19 54.4	1550	2.39	207	219	32.98	5.59	8.8
14 53 42.5 +03 34 56.9	1556	2.27	137	170	178.42	24.7	9.5
15 00 00.4 +01 53 28.7	1368	2.35	316	349	39.25	8.02	8.9
15 00 26.4 +01 37 28.0	1493	2.32	61	142	15.68	1.32	8.2
15 07 07.7 +01 32 39.2	2524	2.66	197	223	64.64	8.87	9.4
15 09 13.2 +52 31 42.3	3479	3.61	379	402	33.93	9.2	9.7
15 09 31.6 +54 30 23.3	3052	3.56	102	158	13.88	1.42	8.8
15 19 25.3 +45 52 48.9	5076	3.36	386	416	26.88	6.92	10.0
15 20 55.4 –02 34 40.5	1975	3.03	340	367	16.67	3.18	8.8
15 26 41.5 +40 33 52.2	2601	3.53	360	389	71.94	23.29	9.9
15 29 45.0 +42 55 07.2	5447	3.15	394	441	16.7	4.69	9.8
15 30 47.3 +23 03 57.9	1971	2.5	92	115	51.78	4.68	9.0
15 35 36.1 +00 22 31.0	2035	2.98	44	76	25.33	1.21	8.4
15 39 02.4 +31 45 35.7	2014	2.8	131	212	23.69	3.01	8.8
15 45 44.5 +20 33 37.4	2075	2.69	60	84	103.56	6.64	9.2
15 59 03.0 +51 18 16.8	3765	3.57	414	425	13.92	3.58	9.4
15 59 12.5 +44 42 59.3	1841	2.85	48	76	49.9	2.55	8.6
15 59 55.5 +06 53 02.6	1549	2.56	27	108	10.24	0.43	7.7
16 01 48.4 +06 50 18.4	1748	2.6	90	101	14.04	0.96	8.2
16 05 45.9 +41 20 41.1	1976	3.27	112	168	110.85	13	9.4
16 08 17.3 +07 32 18.6	1360	2.7	209	228	59.94	11.04	9.0
16 09 20.7 +08 45 47.7	3016	4.14	74	94	109.71	7.8	9.5
16 11 11.5 +48 20 04.0	2783	3.28	83	132	20.99	1.51	8.8
16 18 30.0 +22 09 47.3	4194	2.43	247	294	20.46	4.07	9.6
16 20 47.4 +47 03 53.9	2974	3.94	135	153	13.59	1.21	8.7
16 25 30.5 +49 50 24.9	5850	3.86	131	147	34.51	3.39	9.8
16 25 50.0 +40 29 19.3	8424	4.41	80	191	22.18	2.2	9.9
16 40 21.4 +28 45 55.9	958	3	89	103	38.4	3.25	8.2
16 40 22.2 +28 28 17.5	954	2.51	57	80	16.97	0.94	7.6
16 42 28.9 +34 30 30.3	6478	2.67	290	308	17.09	3.17	9.8

Table A.1 continued ...

Coordinates (J2000) hhmmss degrees	V_{HI} [km s^{-1}]	rms [mJy]	W_{50} [km s^{-1}]	W_{20} [km s^{-1}]	S_{peak} [mJy]	S_{int} [Jy km s^{-1}]	log M_{HI} [M$_\odot$]
17 00 14.6 +23 06 22.8	2948	2.13	119	193	28.67	3.44	9.2
20 55 21.6 –01 12 24.1	3764	2.75	271	286	26.29	4.62	9.5
20 55 27.6 –01 13 30.8	3735	2.6	286	301	31.77	6.07	9.6
21 01 07.7 +00 11 42.6	6972	2.65	409	446	11.4	2.43	9.8
21 02 03.5 –06 17 48.7	7549	2.07	196	209	12.32	1.75	9.7
21 26 57.8 –07 01 17.5	7217	2.32	116	141	31.11	3.09	9.9
21 30 25.9 +00 28 27.7	5885	1.78	262	332	12.46	2.79	9.7
22 05 42.2 +00 33 40.6	4873	3.38	167	180	10.44	1.01	9.1
22 30 36.8 +00 06 36.9	1596	2.53	58	77	11.13	0.55	7.8
22 31 59.0 –09 47 52.4	4542	2.52	187	210	9.58	1.27	9.1
22 41 33.9 +00 24 03.0	1743	2.68	156	179	116.04	14.07	9.3
22 43 59.9 –10 07 01.0	968	2.33	30	63	9.32	0.21	7.0
22 44 24.4 +00 09 43.5	4773	2.58	354	419	25.54	7.58	9.9
22 49 44.9 +15 05 21.0	3360	3.84	158	177	26.5	3.51	9.3
22 51 12.3 +12 46 47.1	2543	2.81	91	149	9.55	0.8	8.4
22 53 04.5 +01 08 40.0	4842	2.42	49	119	16.46	1.17	9.1
22 58 10.1 +14 18 30.5	2105	2.96	103	129	50.91	5	9.0
22 59 07.3 +13 43 16.6	2559	2.44	265	290	72.47	14.21	9.7
22 59 50.4 +13 44 09.8	2612	2.96	134	173	12.73	1.66	8.7
23 06 14.9 +14 39 27.4	1518	2.2	94	114	29.92	2.61	8.5
23 14 17.2 –09 50 10.3	3344	2.8	184	223	19.6	3.16	9.2
23 18 33.6 +13 26 17.8	2566	2.83	149	169	22.07	2.75	9.0
23 19 04.8 –08 29 06.3	2229	2.7	503	527	68.04	20.13	9.7
23 28 12.3 –01 03 46.2	2538	2.98	67	95	37.55	2.36	8.9
23 32 24.4 +15 50 52.2	3978	3.5	224	243	35	5.42	9.6
23 36 31.3 +00 29 43.3	2481	2.89	56	122	17.05	1.16	8.5
23 36 46.9 +00 37 24.3	2613	2.95	47	0	9.15	0.22	7.9
23 37 23.9 +00 23 30.0	2659	2.82	145	168	57.53	7.35	9.4
23 38 41.2 +15 57 16.6	3813	2.94	233	257	14.41	2.48	9.3
23 40 20.7 +01 14 44.7	1856	3.25	190	216	40.3	7.57	9.1
23 42 26.0 +00 15 21.5	6404	2.76	219	282	9.94	1.41	9.5
23 56 07.1 +00 54 59.4	7112	6.15	177	229	52.28	8.82	10.4
23 59 37.0 +14 48 25.0	1739	2.76	181	223	135.79	23.47	9.5

Note: an entry of zero in either columns 5 or 6 indicates that the parameter was not recorded.

Bibliography

Aaronson, M., Huchra, J., & Mould, J. 1979, ApJ, 229, 1

Adelman-McCarthy, J. K., Agüeros, M. A., Allam, S. S., Allende Prieto, C., Anderson, K. S. J., Anderson, S. F., Annis, J., Bahcall, N. A., et al. 2008, ApJS, 175, 297

Adelman-McCarthy, J. K., Agüeros, M. A., Allam, S. S., Anderson, K. S. J., Anderson, S. F., Annis, J., Bahcall, N. A., Bailer-Jones, C. A. L., et al. 2007, ApJS, 172, 634

Adelman-McCarthy, J. K. & et al. 2005, VizieR Online Data Catalog, 2267

Bertin, E. & Arnouts, S. 1996, A&AS, 117, 393

Bessell, M. S. 2005, ARA&A, 43, 293

Binggeli, B., Sandage, A., & Tammann, G. A. 1985, AJ, 90, 1681

Brinks, E. 1990, in Astrophysics and Space Science Library, Vol. 161, The Interstellar Medium in Galaxies, ed. H. A. Thronson, Jr. & J. M. Shull, 39–65

Broeils, A. H. & Rhee, M.-H. 1997, A&A, 324, 877

Catinella, B., Haynes, M. P., & Giovanelli, R. 2005, AJ, 130, 1037

de Vaucouleurs, G., de Vaucouleurs, A., Corwin, Jr., H. G., Buta, R. J., Paturel, G., & Fouque, P. 1991, Third Reference Catalogue of Bright Galaxies

(Volume 1-3, XII, 2069 pp. 7 figs.. Springer-Verlag Berlin Heidelberg New York)

Dickey, J. M. & Lockman, F. J. 1990, ARA&A, 28, 215

Donley, J. L., Staveley-Smith, L., Kraan-Korteweg, R. C., Islas-Islas, J. M., Schröder, A., Henning, P. A., Koribalski, B., Mader, S., & Stewart, I. 2005, AJ, 129, 220

Doyle, M. T., Drinkwater, M. J., Rohde, D. J., Pimbblet, K. A., Read, M., Meyer, M. J., Zwaan, M. A., Ryan-Weber, E., et al. 2005, MNRAS, 361, 34

Eddington, A. S. 1913, MNRAS, 73, 359

Einstein, A. & de Sitter, W. 1932, Proceedings of the National Academy of Science, 18, 213

Falco, E. E., Kurtz, M. J., Geller, M. J., Huchra, J. P., Peters, J., Berlind, P., Mink, D. J., Tokarz, S. P., et al. 1999, PASP, 111, 438

Fisher, J. R. & Tully, R. B. 1981, ApJS, 47, 139

Fisher, K. B., Huchra, J. P., Strauss, M. A., Davis, M., Yahil, A., & Schlegel, D. 1995, ApJS, 100, 69

Folkes, S., Ronen, S., Price, I., Lahav, O., Colless, M., Maddox, S., Deeley, K., Glazebrook, K., et al. 1999, MNRAS, 308, 459

Foot, C. J. 2005, Atomic Physics (Oxford Master Series in Atomic, Optical and Laser Physics) (Oxford University Press, USA)

Fouqué, P., Durand, N., Bottinelli, L., Gouguenheim, L., & Paturel, G. 1990, A&AS, 86, 473

Fukugita, M. 2004, in IAU Symposium, Vol. 220, Dark Matter in Galaxies, ed. S. Ryder, D. Pisano, M. Walker, & K. Freeman, 227

Fukugita, M., Hogan, C. J., & Peebles, P. J. E. 1998, ApJ, 503, 518

Giovanelli, R. 2008, in IAU Symposium, Vol. 244, IAU Symposium, ed. J. Davies & M. Disney, 73–82

Haynes, M. P. 2008, in American Institute of Physics Conference Series, Vol. 1035, The Evolution of Galaxies Through the Neutral Hydrogen Window, ed. R. Minchin & E. Momjian, 238–241

Haynes, M. P., Giovanelli, R., Chamaraux, P., da Costa, L. N., Freudling, W., Salzer, J. J., & Wegner, G. 1999, AJ, 117, 2039

Haynes, M. P., Giovanelli, R., Herter, T., Vogt, N. P., Freudling, W., Maia, M. A. G., Salzer, J. J., & Wegner, G. 1997, AJ, 113, 1197

Heyl, J., Colless, M., Ellis, R. S., & Broadhurst, T. 1997, MNRAS, 285, 613

Impey, C. & Bothun, G. 1997, ARA&A, 35, 267

Kennicutt, Jr., R. C. 1998, ApJ, 498, 541

Koribalski, B. S., Staveley-Smith, L., Kilborn, V. A., Ryder, S. D., Kraan-Korteweg, R. C., Ryan-Weber, E. V., Ekers, R. D., Jerjen, H., et al. 2004, AJ, 128, 16

Kraan-Korteweg, R. C. & Lahav, O. 2000, A&A Rev., 10, 211

Kraan-Korteweg, R. C., Staveley-Smith, L., Donley, J., Koribalski, B., & Henning, P. A. 2005, in IAU Symposium, Vol. 216, Maps of the Cosmos, ed. M. Colless, L. Staveley-Smith, & R. A. Stathakis, 203

Kraan-Korteweg, R. C., van Driel, W., Briggs, F., Binggeli, B., & Mostefaoui, T. I. 1999, A&AS, 135, 255

Kraus, J. D. 1986, Radio Astronomy (Powell, Ohio: Cygnus-Quasar Books, 1986)

Malmquist, K. G. 1936, Stockholms Observatoriums Annaler, 12

Sancisi, R. 1999, in IAU Symposium, Vol. 186, Galaxy Interactions at Low and High Redshift, ed. J. E. Barnes & D. B. Sanders, 71–+

Sarazin, C. L. 1988, S&T, 76, 639

Schechter, P. 1976, ApJ, 203, 297

Schneider, S. E., Spitzak, J. G., & Rosenberg, J. L. 1998, ApJ, 507, L9

Schneider, S. E., Thuan, T. X., Magri, C., & Wadiak, J. E. 1990, ApJS, 72, 245

Smoker, J. V., Davies, R. D., Axon, D. J., & Hummel, E. 2000, A&A, 361, 19

Spergel, D. N., Bean, R., Doré, O., Nolta, M. R., Bennett, C. L., Dunkley, J., Hinshaw, G., Jarosik, N., et al. 2007, ApJS, 170, 377

Spitzak, J. G. & Schneider, S. E. 1998, ApJS, 119, 159

Strauss, M. A., Weinberg, D. H., Lupton, R. H., Narayanan, V. K., Annis, J., Bernardi, M., Blanton, M., Burles, S., et al. 2002, AJ, 124, 1810

Taylor, G. B., Carilli, C. L., & Perley, R. A., eds. 1999, Astronomical Society of the Pacific Conference Series, Vol. 180, Synthesis Imaging in Radio Astronomy II

Theureau, G., Bottinelli, L., Coudreau-Durand, N., Gouguenheim, L., Hallet, N., Loulergue, M., Paturel, G., & Teerikorpi, P. 1998, A&AS, 130, 333

Tully, R. B. & Fisher, J. R. 1977, A&A, 54, 661

van Driel, W., Schneider, S., Lehnert, M., & NIBLES Consortium, t. 2007, ArXiv e-prints, 711

van Zee, L. 2001, AJ, 121, 2003

Verheijen, M. A. W. 2001, ApJ, 563, 694

Marzke, R. O., Geller, M. J., Huchra, J. P., & Corwin, Jr., H. G. 1994, AJ, 108, 437

Masters, K. L., Springob, C. M., & Huchra, J. P. 2008, AJ, 135, 1738

Mathewson, D. S., Ford, V. L., & Buchhorn, M. 1992, ApJS, 81, 413

Matthews, L. D., Gallagher, III, J. S., & Littleton, J. E. 1995, AJ, 110, 581

Matthews, L. D. & van Driel, W. 2000, A&AS, 143, 421

Matthews, L. D., van Driel, W., & Gallagher, III, J. S. 1998, AJ, 116, 2196

Meyer, M. J., Zwaan, M. A., Webster, R. L., & et al. 2004, VizieR Online Data Catalog, 8073

Monnier Ragaigne, D., van Driel, W., Schneider, S. E., Balkowski, C., & Jarrett, T. H. 2003, A&A, 408, 465

Paturel, G., Theureau, G., Bottinelli, L., Gouguenheim, L., Coudreau-Durand, N., Hallet, N., & Petit, C. 2003, A&A, 412, 57

Pérez-González, P. G., Rieke, G. H., Egami, E., Alonso-Herrero, A., Dole, H., Papovich, C., Blaylock, M., Jones, J., et al. 2005, ApJ, 630, 82

Petrosian, V. 1976, ApJ, 210, L53

Pizagno, J., Prada, F., Weinberg, D. H., Rix, H.-W., Pogge, R. W., Grebel, E. K., Harbeck, D., Blanton, M., et al. 2007, AJ, 134, 945

Prochaska, J. X. & Tumlinson, J. 2008, ArXiv e-prints, 805

Rao, S. & Briggs, F. 1993, ApJ, 419, 515

Roberts, M. S. & Haynes, M. P. 1994, ARA&A, 32, 115

Rosenberg, J. L. & Schneider, S. E. 2002, ApJ, 567, 247

Salim, S., Charlot, S., Rich, R. M., Kauffmann, G., Heckman, T. M., Barlow, T. A., Bianchi, L., Byun, Y.-I., et al. 2005, ApJ, 619, L39

Warren, B. E., Jerjen, H., & Koribalski, B. S. 2006, AJ, 131, 2056

Wong, O. I., Ryan-Weber, E. V., Garcia-Appadoo, D. A., Webster, R. L., Staveley-Smith, L., Zwaan, M. A., Meyer, M. J., Barnes, D. G., et al. 2006, MNRAS, 371, 1855

Young, J. S. & Scoville, N. Z. 1991, ARA&A, 29, 581

Zwaan, M. A., Briggs, F. H., Sprayberry, D., & Sorar, E. 1997, ApJ, 490, 173

Zwaan, M. A., Meyer, M. J., Staveley-Smith, L., & Webster, R. L. 2005, MNRAS, 359, L30

Zwaan, M. A., Staveley-Smith, L., Koribalski, B. S., Henning, P. A., Kilborn, V. A., Ryder, S. D., Barnes, D. G., Bhathal, R., et al. 2003, AJ, 125, 2842